

UNIVERSITY OF OKLAHOMA
GRADUATE COLLEGE

INVESTIGATION AND MODELING OF FRICTIONAL BOUNDARY
CONDITIONS IN OBLIQUE CUTTING OF ALUMINUM ALLOYS

A DISSERTATION
SUBMITTED TO THE GRADUATE FACULTY
in partial fulfillment of the requirements for the
Degree of
DOCTOR OF PHILOSOPHY

BY
DURSUN SEDAT KILIC
Norman, Oklahoma
2012

INVESTIGATION AND MODELING OF FRICTIONAL BOUNDARY
CONDITIONS IN OBLIQUE CUTTING OF ALUMINUM ALLOYS

A DISSERTATION APPROVED FOR THE
SCHOOL OF INDUSTRIAL AND SYSTEMS ENGINEERING

BY

Dr. Shivakumar Raman, Chair

Dr. M. Cengiz Altan

Dr. Theodore B. Trafalis

Dr. F. Hank Grant

Dr. J. David Baldwin

© Copyright by DURSUN SEDAT KILIC 2012
All Rights Reserved.

ACKNOWLEDGEMENTS

First and foremost I want to thank my advisor Dr. Shivakumar Raman. It has been an honor to be his Ph.D. student. I appreciate all his contributions of time, ideas, support and funding throughout my Ph.D. study. I also want to thank for this continuous encouragement and patience to support me in achieving my doctoral degree.

I gratefully acknowledge the financial support provided by the National Science Foundation (NSF) to the project that made my Ph.D. possible.

I would like to thank to my colleague Arindam Basu for his help in performing experiments and his comments during my early research study. I thank Sam Noble Research Center and Sarkeys Energy Center in my attempts of getting SEM images.

I would like to sincerely thank to my friend Orhan Ozcelik in proof reading of my thesis draft and for his very valuable help in the final stage of my graduate study.

Lastly, I would like to thank my parents for all their love and encouragement who raised me with love and supported in all my pursuits. And most of all for my loving, supportive and patient wife Burcu for her faithful support during final stages of my Ph.D.

TABLE OF CONTENTS

ACKNOWLEDGEMENTS		iv
TABLE OF CONTENTS		v
LIST OF TABLES		vii
LIST OF FIGURES		ix
ABSTRACT		xvi
CHAPTER 1	INTRODUCTION	1
CHAPTER 2	THEORY OF METAL CUTTING	5
	Shear Plane Model	10
	Slip Line Field Solution	13
	Friction in Metal Cutting	14
	Tool Chip Contact Area	21
	Chip Flow	24
	Normal and Shear Stress Models	26
CHAPTER 3	PRELIMINARY EXPERIMENTS	34
	Experimentation and Analysis Methods	34
	Preliminary Experiments and Data Analysis	42
CHAPTER 4	MAIN EXPERIMENTS AND DATA ANALYSIS	56
	SEM Image Analysis	58
	Cutting Force Data Analysis	87
	Plowing Force Determination	101

CHAPTER 5	MATHEMATICAL MODEL OF TOOL	
	STRESSES	107
	Stress Model	107
CHAPTER 6	CONCLUSION	120
REFERENCES		129
APPENDIX A	MATLAB CODE	135
APPENDIX B	SEM IMAGES	140
APPENDIX C	CUTTING FORCE MEASUREMENTS	148

LIST OF TABLES

Table	Page
2.1. Summary of photoelastic tool studies	28
2.2. Summary of split tool method studies	31
3.1. Numerical values of contact area repeatability testing	43
3.2. Results of LSCM imaging	50
3.3. Elastic modulus and hardness values of Al-6061 at the tool chip interface	55
4.1. Uncut chip area and d/f ratio for the depth of cut and feed rates used in the experiments	57
4.2. Primary sticking, sliding and secondary sticking area values for Al-2024 at 110 m/min	63
4.3. Primary sticking, sliding and secondary sticking area values for Al-2024 at 225 m/min	66
4.4. Primary sticking, sliding and secondary sticking area values for Al-2024 at 335 m/min	68
4.5. Primary sticking, sliding and secondary sticking area values for Al-2024 at 470 m/min	71
4.6. Primary sticking, sliding and secondary sticking area values for Al-6061 at 120 m/min	78
4.7. Primary sticking, sliding and secondary sticking area values for	

	Al-6061 at 230 m/min	80
4.8.	Primary sticking, sliding and secondary sticking area values for Al-6061 at 345 m/min	83
4.9.	Primary sticking, sliding and secondary sticking area values for Al-6061 at 490 m/min	85
4.10.	Normal and frictional forces on the cutting tool for Al-2024 at different cutting speeds, feed rate and depth of cut	95
4.11.	Normal and frictional forces on the cutting tool for Al-6061 at different cutting speeds, feed rate and depth of cut	96
4.12.	Plowing forces for Al-2024	103
4.13.	Plowing forces for Al-6061	104
4.14.	Normal and frictional forces on the cutting tool for Al-2024 at different cutting speeds, feed rate and depth of cut - after plowing force effect is removed	105
4.15.	Normal and frictional forces on the cutting tool for Al-6061 at different cutting speeds, feed rate and depth of cut - after plowing force effect is removed	106

LIST OF FIGURES

Figure	Page
2.1. Two-dimensional orthogonal cutting model	5
2.2. Schematic representation of oblique cutting	7
2.3. Single-point turning operation	8
2.4. Single-point cutting tool geometry	9
2.5. Piispanen's card model	11
2.6. Three regimes of solid friction	16
2.7. Zorev's model	17
2.8. Average rake face stresses versus contact length ratio	18
2.9. Chip flow direction model	25
2.10. Shear and normal stress distribution models obtained by photoelastic tool and split tool methods	29
3.1. Industrial lathe and data acquisition system	35
3.2. Original SEM image and the cropped and redefined image	38
3.3. Cleaning code results	40
3.4. Area identification by MATLAB® code	41
3.5. Reliability test results for the cutting force and contact area values	43
3.6. Profilometer results of tool-chip contact area for Al-7075	44
3.7. SEM images for Al-2024	46
3.8. SEM images for Al-6061	47

3.9.	Surface topography analysis of Al-2024 at different cutting speed and cutting times	48
3.10.	Surface topography analysis for Al-6061 at different cutting speed and cutting times	49
3.11.	Backscattered image of tool-chip contact area, showing different frictional conditions	52
3.12.	Elemental scan and chemical composition of sticking areas: (a) Primary sticking zone, (b) Secondary sticking zone	54
4.1.	Modified SEM images of tool-chip contact area for cutting experiments of AL-2024 at 110 m/min, different feed rates and depths of cut	59
4.2.	Modified SEM images of tool-chip contact area for cutting experiments of AL-2024 at 225 m/min, different feed rates and depths of cut	60
4.3.	Modified SEM images of tool-chip contact area for cutting experiments of AL-2024 at 335 m/min, different feed rates and depths of cut	61
4.4.	Modified SEM images of tool-chip contact area for cutting experiments of AL-2024 at 470 m/min, different feed rates and depth of cuts	62
4.5.	Frictional contact areas vs d/f for Al-2024 at 110 m/min	64
4.6.	Chemical composition of primary and secondary sticking	

zones for Al-2024 at 110 m/min	65
4.7. Frictional contact areas vs d/f for Al-2024 at 225 m/min	67
4.8. Chemical composition of primary and secondary sticking zones for Al-2024 at 225 m/min	67
4.9. Frictional contact areas vs d/f for Al-2024 at 335 m/min	69
4.10. Chemical composition of primary and secondary sticking zones for Al-2024 at 335 m/min	70
4.11. Frictional contact areas vs f/d for Al-2024 at 470 m/min	72
4.12. Chemical composition of primary and secondary sticking zones for Al-2024 at 470 m/min	72
4.13. Modified SEM images of tool-chip contact area for cutting experiments of AL-6061 at 120 m/min for different feed rates and depths of cut	74
4.14. Modified SEM images of tool-chip contact area for cutting experiments of AL-6061 at 230 m/min for different feed rates and depth of cuts	75
4.15. Modified SEM images of tool-chip contact area for cutting experiments of AL-6061 at 345 m/min for different feed rates and depth of cuts	76
4.16. Modified SEM images of tool-chip contact area for cutting experiments of AL-6061 at 490 m/min for different feed rates and depth of cuts	77

4.17.	Frictional contact areas vs d/f for Al-6061 at 120 m/min	79
4.18.	Chemical composition of primary sticking zone for Al-6061 at 120 m/min	79
4.19.	Frictional contact areas vs d/f for Al-6061 at 230 m/min	81
4.20.	Chemical composition of primary and secondary sticking zones for Al-6061 at 230 m/min	81
4.21.	Frictional Contact Areas vs d/f for Al-6061 at 345 m/min	83
4.22.	Chemical composition of primary and secondary sticking zones for Al-6061 at 345 m/min	84
4.23.	Frictional contact areas vs f/d for Al-6061 at 490 m/min	86
4.24.	Chemical composition of primary and secondary sticking zones for Al-6061 at 490 m/min	86
4.25.	Schematic of cutting force axes	88
4.26.	Schematic showing force measurement axis, forces acting on the tool, and tool geometry	90
4.27.	Planar view of the cutting tool (xy plane)	91
4.28.	Planar view of cutting tool when projected in the modified axial direction	92
4.29.	Planar view of cutting tool when projected in the modified radial direction	93
4.30.	Frictional force on the rake face	94
4.31.	3-D schematic representation of equivalent cutting tool	

with actual cutting forces	94
4.32. Normal and frictional force vs. d/f for Al-2024 at 110 m/min	97
4.33. Normal and frictional force vs. d/f for Al-2024 at 225 m/min	97
4.34. Normal and frictional force vs d/f for Al-2024 at 335 m/min	98
4.35. Normal and frictional force vs d/f for Al-2024 at 470 m/min	98
4.36. Normal and frictional force vs. d/f for Al-6061 at 120 m/min	99
4.37. Normal and frictional force vs. d/f for Al-6061 at 230 m/min	99
4.38. Normal and frictional force vs. d/f for Al-6061 at 345 m/min	100
4.39. Normal and frictional force vs. d/f for Al-6061 at 490 m/min	100
4.40. Plowing force and contact regions on a cutting tool	102
4.41. Graphical determination of plowing force for Al-2024 at 470 m/min and low feed rate	103
5.1. Lee's model for normal and shear stresses	108
5.2. Schematic of stress model	111
5.3. Comparison of predicted and experimental frictional forces for Al-2024 at 110 m/min	111
5.4. Comparison of predicted and experimental frictional forces for Al-2024 at 225 m/min	112
5.5. Comparison of predicted and experimental frictional forces for Al-2024 at 335 m/min	112
5.6. Comparison of predicted and experimental frictional forces for Al-2024 at 470 m/min	113

5.7.	Comparison of predicted and experimental normal forces for Al-2024 at 110 m/min	114
5.8.	Comparison of predicted and experimental normal forces for Al-2024 at 225 m/min	114
5.9.	Comparison of predicted and experimental normal forces for Al-2024 at 335 m/min	115
5.10.	Comparison of predicted and experimental normal forces for Al-2024 at 470 m/min	115
5.11.	Comparison of predicted and experimental frictional forces for Al-6061 at 120 m/min	116
5.12.	Comparison of predicted and experimental frictional forces for Al-6061 at 230 m/min	116
5.13.	Comparison of predicted and experimental frictional forces for Al-6061 at 335 m/min	117
5.14.	Comparison of predicted and experimental frictional forces for Al-6061 at 490 m/min	117
5.15.	Comparison of predicted and experimental normal forces for Al-6061 at 120 m/min	118
5.16.	Comparison of predicted and experimental normal forces for Al-6061 at 230 m/min	118
5.17.	Comparison of predicted and experimental normal forces for Al-6061 at 345 m/min	119

5.18. Comparison of predicted and experimental normal forces for Al-6061 at 490 m/min	119
--	-----

ABSTRACT

Friction at the cutting tool interface has been studied for 60 years, yet an accurate model of friction is largely unavailable, especially in operations such as turning, where the interface is inaccessible due the continuous contact between chip and tool. A historical perspective of friction in turning is provided to better understand the purpose of this thesis. The contradictions arising from different frictional boundary condition assumptions in machining were analyzed. Experimental observations were substantiated in the light of the literature review. Friction conditions at the tool chip interface were found to be more complex than the simple models of seizure followed by sliding, which is accepted in most machining models.

This thesis investigated the surface topology of cutting tools in conventional turning operation, which is one of the oldest and common machining processes. Two different aluminum alloys Al-2024 and Al-6061 were used in turning experiments with carbide tools to define the frictional conditions as these alloys exhibited a wide range of frictional contacts at different machining conditions. Experiments were conducted using carbide cutting tools at a range of speeds, feed rates, and depths of cut, which are commonly utilized in industrial applications.

The analysis of tool chip interface at microscopic levels revealed further details of seizure and sliding zone formation. Newer techniques developed in

microscopy and surface characterization were used to characterize the interface in a non-destructive manner. Scanning electron microscopy (SEM), surface profilometer and laser scanning confocal microscopy (LSCM) techniques helped us in the understanding of the frictional boundaries.

Analysis of SEM images obtained by turning experiments revealed three distinct regions whose topology is closely related to turning parameters. These different zones were named as primary sticking zone, sliding zone and secondary sticking zone. Furthermore, with the assistance of a developed computer code, the real area of contact and each different contact area were determined numerically. Therefore, this study is the first attempt in literature both identifies the frictional contact areas and computes their exact numerical values.

The SEM backscattering technique showed that the workpiece material behavior is different in the built up edge and sticking areas. This finding was especially used to identify the preliminary and secondary sticking areas. Thus, it has been showed first time that the deposited layers on frictional areas show different material characteristics. With the help of tool surface image analysis, area calculation algorithm, chemical composition identification, and earlier efforts cited in the literature, we proposed a stress-model which accurately predicted experimental normal and shear forces in oblique cutting of aluminum alloys for most tested conditions.

CHAPTER 1

INTRODUCTION

Machining is a generic term applied to all metal removal processes. Metal cutting process is one of the oldest and most fundamental metal removal processes used to form metal into functional parts by removing unwanted workpiece material to achieve the desired dimensions with accuracy. Most practical machining operations, such as turning, drilling, and milling require energy to deform the workpiece material plastically by a harder tool and remove the deformed, unwanted material in terms of chips from the newly generated part.

The study of machining focuses on the features of cutting process, such as cutting conditions, tool and workpiece material behavior and cutting performance that have a direct effect on the efficiency of the process and the quality of the produced part. In spite of the fact that the metal cutting is the most widely used machining operation in industry, the fundamental principle of this process is not exactly known yet due to its complex nature. Extensive studies have been performed to understand the fundamentals of machining to increase the productivity and efficiency of the process.

The objective of metal cutting study is to develop science-driven models that will predict the technical measures of cutting operations such as chip formation, cutting forces, temperature, tool wear, and finished part accuracy. Practical applications of such models in industry will contribute to progress of

performance and productivity of machining operation. However, to meet the diverse demands of industry, different models have been developed for different purposes by utilizing different principles and techniques. In most of the metal cutting studies, analytical models have been supported by experiments that have been conducted using limited practical cutting conditions that are applicable to a specific domain rather covering all the cutting conditions. This approach is time consuming, domain dependent and relies on limited and mostly empirical data. Therefore, the models differ according to the type of operation, the quantity predicted, the purpose of the model, and the modeling technique. As a result, there is no unique model that completely comprises all aspects of the mechanics of metal cutting.

The majority of metal cutting studies has investigated orthogonal cutting because of its simplicity, where the cutting edge is perpendicular to the axis of feed motion and the cutting velocity direction. In other words, plastic deformation takes place under plain strain condition. However, nearly all practical cutting processes are oblique, i.e. the tool cutting edge is inclined to the feed and relative cutting velocity directions. Therefore, two-dimensional (orthogonal) cutting theory has to be extended and applied (broadened) to practical, three-dimensional cutting.

Also, much of the research in metal cutting has been concentrated on the primary shear zone, where big proportion of the cutting energy is used to deform the material. A noticeable amount of cutting energy is consumed in the secondary

shear zone to overcome the friction between tool and chip as the chip flows over the tool surface. The cutting conditions at this zone are so severe that the classical frictional theory fails to explain the physics of chip flow.

Frictional behavior at the tool chip interface has been studied by many researchers due to its profound yet inexact and undetermined effect on metal cutting performance. Frictional interaction between tool and chip does not only effect the chip formation process in terms of cutting forces, temperatures and wear rate, but it is also considered as a function of those variables. Moreover, the frictional boundary conditions consist of sticking and sliding interfaces, exhibiting variability in geometry depending on the cutting parameters, tools and workpiece material behavior. The classical model of fixed sticking and sliding geometry is questionable. Presently, a general and accurate description of the interface boundary conditions is not yet available.

This study aims to determine physical quantities such as cutting forces and tool chip contact areas both quantitatively and qualitatively in oblique cutting, so that a new frictional model that will serve for the improved productivity and effectiveness of the metal cutting practices can be developed. Therefore, the focus is the secondary deformation zone in oblique cutting, typically the turning operation.

In this study, the historical development of metal cutting is presented. The fundamentals and different theories of metal cutting were summarized. Preliminary experiments performed with different aluminum alloys were

introduced. The results of the preliminary experiments showed which techniques and methodologies will be performed for further analysis of the oblique cutting. After the methodology has been established, main experiments were designed and performed with two different aluminum alloys. Force measurements were recorded during cutting experiments. SEM images of tool chip contact area were obtained after the cutting experiments. Analysis of SEM images and metallographic studies of contact zones revealed the different contact zones on the cutting zone. Image processing technique was used to find the exact numerical values of frictional contact zones. Experimental data, investigation, and data analysis showed that different alloys could behave differently under the same cutting conditions.

Finally, a mathematical stress model was developed and compared with the experimental data. Results and model fit is discussed at the end of the study.

The following chapter represents the theory of metal cutting and the literature review. Chapter 3 documents preliminary studies and experiments, and Chapter 4 presents main experiments and their data analysis. A mathematical model of stress distribution on cutting tool and model verification is shown in Chapter 5. Investigations of the data analysis and modeling validation are summarized at the conclusion part of this thesis.

CHAPTER 2

THEORY OF METAL CUTTING

Metal cutting operation is a metal removal process that produces chips. Therefore, analysis of chip formation is the basic understanding point in the metal cutting mechanics. However, it is not easy to understand chip formation mechanics due to the complexity of plastic deformation involved.

Simple orthogonal cutting represents all practical cutting operations reasonably well; therefore, it has been extensively studied. A simple two-dimensional orthogonal cutting model is given in Figure 2.1.

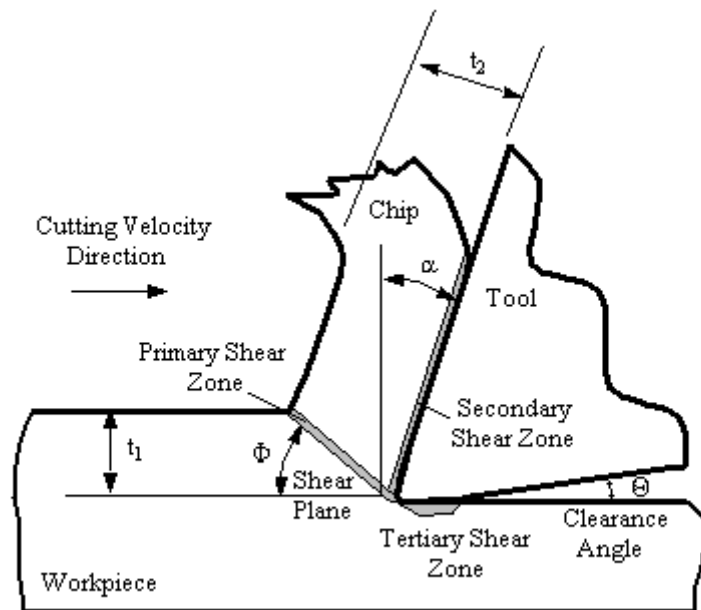


Figure 2.1. Two-dimensional orthogonal cutting model

In orthogonal cutting, a tool with a plane cutting face and single, straight cutting edge, removes a layer of work material of an undeformed chip thickness of t_1 , and width of w . The cutting edge is always normal to the cutting velocity. The angle α between the tool cutting edge and the normal of the cutting velocity is defined as the rake angle, and it is measured positive if it is as shown in the figure. Rake angle has an important effect on cutting forces and other cutting variables. The angle θ between the clearance face and the finished work surface is called the clearance angle. Plastic deformation takes place by intense shear mechanism in the shear plane, inclined by the shear angle Φ with respect to the finished surface line. There are three deformation zones of interest in the cutting process. The primary shear zone extends from the tool tip to the free surface of the workpiece, separating the deformed and undeformed material through the shear plane. At low speeds, this zone gets thicker, and it becomes difficult to predict the plastic deformation behavior. The secondary shear zone is the contact zone between tool rake face and deformed chip material. Due to the severe cutting conditions and friction, high heat generation and deformation of tool matrix is possible. This results in tool wear and shortening of the tool life. Friction in this zone is not easy to predict, since it cannot be explained by classical frictional laws. During cutting, the contact load between tool and chip is very high, resulting in unpredictable behavior of frictional interaction between tool and chip. The tertiary zone is perpendicular to tool tip clearance face and consists of the tool machined surface and tool interaction through the clearance face. This zone is

mainly responsible for the surface roughness of the finished surface. The mechanics of machining focuses in plastic deformation characteristics in the primary deformation zone and in the friction and wear characteristics at the tool-chip interface in the secondary shear zone. Very often, the tertiary shear zone is neglected.

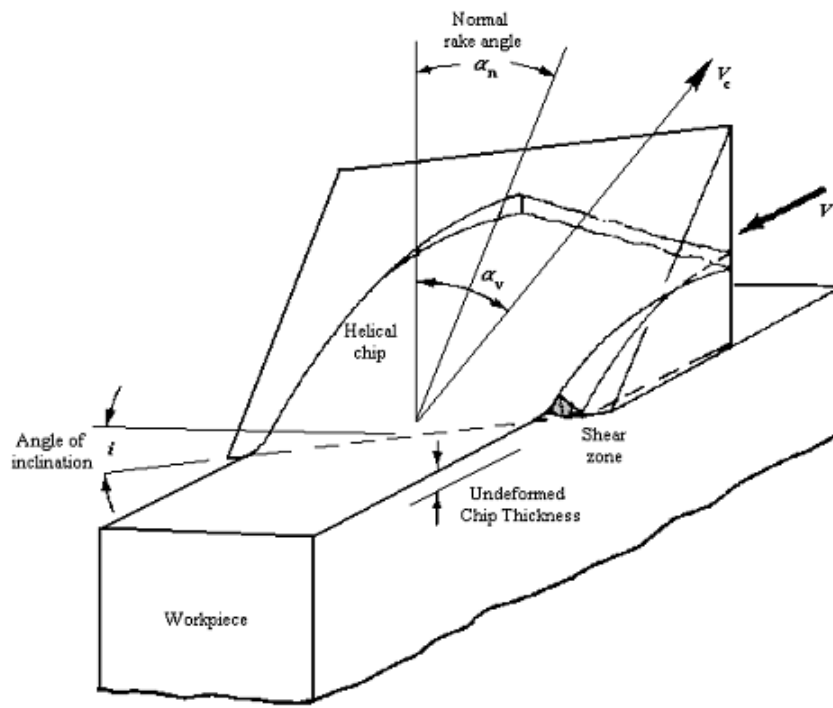


Figure 2.2. Schematic representation of oblique cutting

As a result of the difficulty in the analysis of three-dimensional plastic flow process, approximate methods have been developed to model the more general cutting process. A schematic representation of an oblique cutting chip formation is illustrated in Figure 2.2.

The main difference between oblique and orthogonal machining is that the chip flow direction is no longer normal to the cutting edge, since the cutting edge is not set normal to the cutting velocity in the plane of the newly machined surface. It is inclined by an angle i , which is called the inclination angle. Because of this inclination, the chip curls into a helical rather than a spiral shape and is removed easily. In defining the rake angle in oblique cutting, different types of rake angles were introduced, such as effective rake angle α_e , velocity rake angle α_v and normal rake angle α_n . The feed rate f and depth of cut d are representative of undeformed chip thickness h and width of cut w in orthogonal cutting, respectively. The aforementioned deformation zones are also valid in oblique cutting.

Turning is a special form of oblique cutting process mainly accomplished on a lathe, where a cylindrical workpiece is rotated, and a single point cutting tool is used to remove the unwanted material to produce the desired part. Figure 2.3 shows a simple sketch of a single-point turning operation.

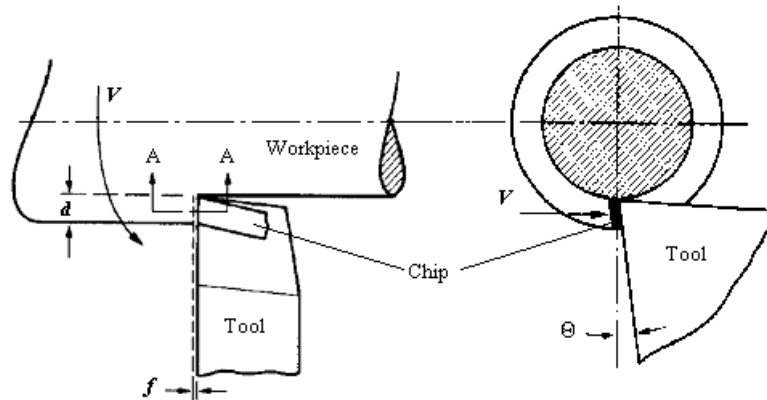


Figure 2.3. Single-point turning operation

Cutting speed V (fpm or m/min), the feed rate f (ipr or mm/rev) and depth of cut d (in or mm) are the main operational variables in a turning operation. The chip formation process is said to be plane strain, since the depth of cut d is usually larger than the feed rate f at least by five times. A single point cutting tool with its cutting edges and surfaces is shown in Figure 2.4.

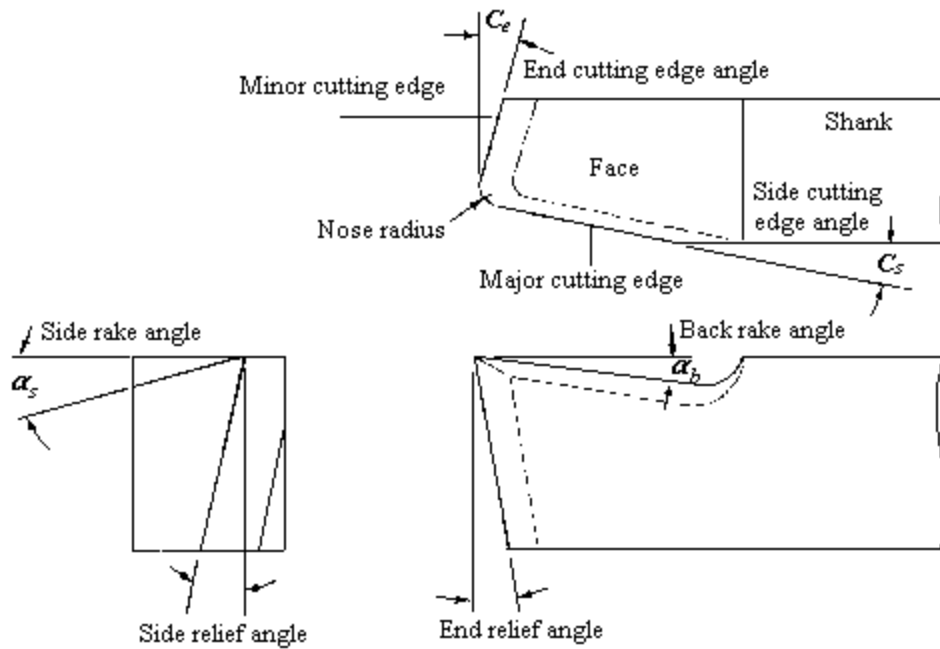


Figure 2.4. Single-point cutting tool geometry

The rake face is the surface on which the chip is flowing. The flank is the tool surfaces over which the surface produced on the workpiece passes. Intersection of major and minor flank surfaces with the rake face form the side cutting edge and end cutting edge, respectively. The corner of the cutting edges is mainly rounded with a nose radius to give strength to the tool. The geometry of

the tool is important in machining performance since it accommodates primary motion, feed motion, and chip disposal. Since in most cases the depth of cut to feed ratio is approximately 10, the main cutting action takes place at the side cutting edge, and the end cutting edge helps to remove the chip. Consequently, the end cutting edge is neglected most of the time. The important tool angles are the side cutting edge angle C_s , the end cutting edge angle C_e , the back rake angle α_b , the side rake angle α_s , and the clearance angles. The cross-sectional area of the layer material being removed (uncut chip cross-sectional area) is approximated by the formula:

$$A_c = fd \quad (1)$$

Strong knowledge of engineering mechanics, material science, plasticity, tribology and thermodynamics is required to understand what happens during the cutting operation. Many models can be found in the literature to explain the mechanics of machining. Some of the popular ones are explained in the sequel below.

Shear Plane Model

The scientific approach that explains the principles of cutting mechanics started with Piispanen [1]. He defined the chip material as a pack of cards sliding

by a finite distance across its neighbor and assumed that shear stress on the shear plane would increase with normal stress (Figure 2.5).

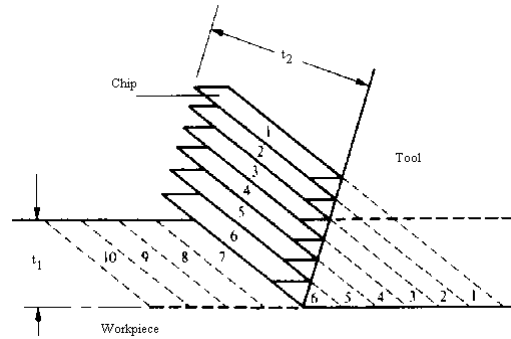


Figure 2.5. Piispanen's card model

This was the same assumption of Ernst and Merchant [2, 3]. They defined the deformation process taking place on a single shear plane; hence, maximum shear stress and maximum shear strain are oriented along this shear plane direction. They defined the shear angle based on the minimum work principle:

$$\Phi = \frac{\pi}{4} + \frac{\alpha}{2} - \frac{\beta}{2} \quad (2)$$

Merchant's analytical approach assumes straight, continuous chip formation with infinite tool-chip contact area, where classic sliding friction is the main mechanism. The frictional force along the rake face was assumed completely Coulombic. However, during machining, where high temperature,

pressure and deformation conditions exist, Coulombic friction does not hold. Therefore, although Merchant's shear plane model is an important attempt to understand the mechanics of machining, the assumption of total sliding between tool and chip is incorrect. The shear plane model was further redefined by Trigger and Chao [4]. Their work is based on the heat generation in orthogonal machining, where they showed that the increase in the coefficient of sliding friction at the tool-chip interface is a result of the decrease of interface temperature. A decrease in the cutting forces was also observed for harder materials although the cutting temperatures increase due to the smaller chip-contact area and higher stresses.

These approaches led many researchers to conduct experiments with different operating conditions using different materials. Lee and Shaffer [5] applied plasticity theory to the machining problem. They assumed the material above the shear plane to be in plastic stress state and the shear stress at the shear plane was assumed to be constant. This resulted in the shear angle formula as:

$$\Phi = \frac{\pi}{4} + \alpha - \beta \quad (3)$$

Shaw et al. [6] modified this equation to fit the experimental data they obtained. Kobayashi and Thomsen [7] introduced the concept of measure of the deviation from the minimum energy principle to have an agreement between the experimental and empirical results. Dewhurst [8] presented slip line fields to

account for the effect of chip curl. The main feature of this approach is the introduction of a curved shear plane to accommodate the required velocity gradient across the chip and tool-chip interface. Shaw [9] concluded that it is not possible to obtain a unique shear angle relationship. This conclusion is valid since in all shear plane models, work material is assumed to deform at constant flow stress. However, generally, the flow stress of metals varies with strain, strain-rate and temperature and it is essential to take into account all of these variables to develop a satisfactory machining theory.

Slip Line Field Solution

Another approach in chip formation modeling was to extrapolate material test results to the conditions occurring in metal cutting, i.e., large strain, strain rate and temperature values. Followers of this approach started with Oxley [10], who used experimental flow fields to model a slip line field. The experimental flow fields were obtained from magnified motion pictures and quick-stop photos. These slip line fields were then used to determine shear angle and other parameters. The traces of flow stream lines showed that the plastic deformation takes place in a narrow zone. Roth and Oxley [11] showed that the hydrostatic pressure across the length of the shear zone varies. Based on the slow cutting speed experiments, Oxley developed the predictive slip line field theory.

Friction in Metal Cutting

Friction is defined as the resistant force one surface experiences when one solid body slides over another, and it is always directed opposite to the relative velocity. The principles of friction are summarized as Amonton's laws and verified by Coulomb. These laws state that the frictional force F is proportional to the normal load N , and the ratio of these two forces is known as the coefficient of friction, which is independent of the area of contact between the contacting bodies, as given:

$$\mu = \frac{F}{N} \quad (4)$$

It is also proposed that the frictional force and coefficient of friction are independent of the sliding speed, temperature and surface finish of the contacting bodies. These laws are valid when real and apparent contact areas are different.

Bowden and Tabor [12] demonstrated that the real area of contact could be much smaller than the apparent area and vary with normal load and hardness of contacting surfaces. They explained this phenomenon by introducing an interfacial film separating the surfaces. Interfacial sliding would only occur if the tangential force overcame the shear strength of interfacial film. Up to that point, the junctions will deform under normal and shear forces, thus increasing the

contact area. As a result of this asperity deformation theory, the coefficient of friction was modeled by:

$$\mu = \frac{1}{\delta^{1/2} (f^{-2} - 1)^{1/2}} \quad (5)$$

where, f is normalized film strength given by $f = \tau/k$, τ is the shear strength of the film, k is the shear flow stress of the deforming material, and δ is an empirical factor. This adhesion model does not take the surface roughness value into consideration.

The asperity deformation model was further analyzed by Green [13], applying plasticity theory. He claimed that during junction growth, different junctions being at various stages of development, the friction could be taken as the ratio of the average tangential and normal forces acting over the life cycle of a typical junction. Adhesion theory sheds some light to the understanding of the mechanism involved in friction, but it relies heavily on the formation and fracture of welds. It is also deficient in terms of wear and hardness consideration of contacting bodies.

Shaw et al. [9] investigated the variation of friction with the change in normal stress, as shown in Figure 2.6. Regime I is where Amonton's law holds ($\mu = \tau/\sigma = \text{constant}$). In regime III, the apparent area of contact is equal to the real area of contact, and shear stress is independent of normal stress. Regime II is a

transition region, where the coefficient of friction decreases with increasing normal load. In that respect this region is more representative of the frictional conditions that occur at the tool chip interface. Zorev [14] developed a model which predicts the frictional conditions at the tool chip interface by suggesting a normal and shear stress distribution at the tool rake face as shown in Figure 2.7. He used controlled contact length cutting tools to measure the forces for different contact lengths, where he machined steel orthogonally at low and moderate cutting speeds (0.02, 0.7, 60, 70 and 80 m/min), at different depth of cuts using different rake angle tools. According to this model, the initial part of the interface is considered as *sticking zone*, where intense plastic shearing of weaker (chip) material occurs, and the rest of the contact zone is represented as *sliding zone* with relatively less severe frictional conditions. These zones were defined from the photomicrographs obtained by quick-stop mechanism.

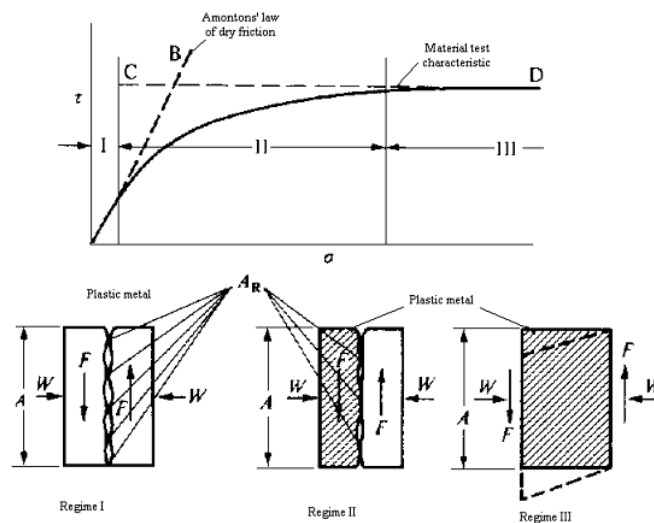


Figure 2.6. Three regimes of solid friction [9]

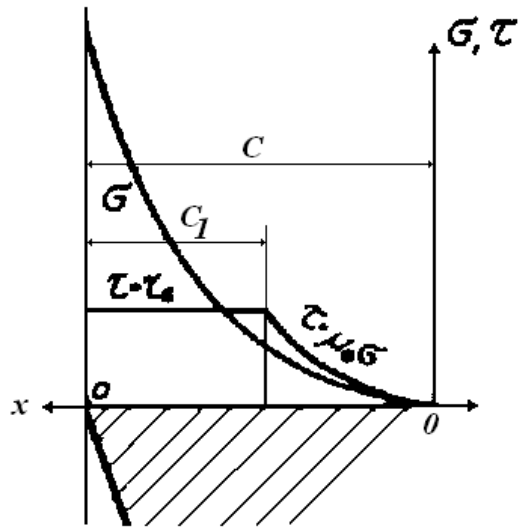


Figure 2.7. Zorev's model

Zorev assumed a uniform shear stress in the sticking region and a decreasing shear stress with a power law in the sliding zone. The normal stress distribution was modeled with the power law equation of $\sigma = qx^y$, where x is the distance from the point where chip leaves the tool, and q and y are constants. Wallace and Boothroyd [15] also pointed out the defined regions as sticking and sliding friction at tool-chip interface, where they used a shaper to cut an aluminum alloy using different rake angle tools and at low and moderate cutting speeds (18, 28, 54, 70 m/min) as shown in Figure 2.8. They also used quick-stop mechanism to investigate the underside of the chip and interface. They introduced the variability of tool-chip interfacial friction and concluded the dependence of friction on the normal stress distribution on the rake face, shear strength of the chip material at the tool chip interface, and the coefficient of sliding friction.

The terms sticking and sliding have been literally interpreted by Doyle et al. [16], where sticking and sliding were related to mean adhesion between chip and tool material. Seizure at the tool rake face was introduced by Trent [17] after viewing the sweeping back of chip material into a thin, parallel layer to the tool rake face, obtained at very low cutting speeds using high speed steel (HSS) tools, with the use of quick-stop mechanism. This condition favors the built up edge formation. Transparent sapphire cutting tools were used by Horne et al. [18] and Doyle et al. [16] to observe the frictional interactions at the tool-chip interface. When machining soft materials such as aluminum and lead a sliding region just behind the cutting edge was observed, followed by a sticking region.

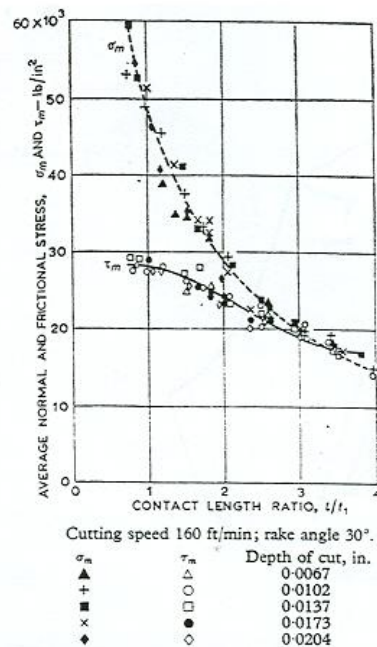


Figure 2.8. Average rake face stresses versus contact length ratio [15]

Experiments performed by Horne et al. [18] using sapphire tools to cut lead showed the sticking zone at the rear part of the contact length, which contradicts Zorev's model. Sliding conditions dominate in the region just behind the cutting edge when comparatively soft materials (aluminum, lead) are machined with sapphire tools. On the other hand, sticking dominates in this region when hard materials (steel, iron) are machined with metal tools. Wright [19] concluded that sticking and sliding happen as a result of stress conditions and surface properties. In his experiments, single stroke planing was performed in air, with lubricants and under vacuum conditions. Sapphire tools are used to cut pure lead and aluminum. HSS planing tools with 10° and 40° rake angle were also used to machine pure copper, iron, and nickel. Maximum cutting speed was 140 mm/s, resulting in a cutting time of 1.4 s. Depth of cut was 0.1 mm, and width of cut was 2.5 mm. At the end of his study, Wright concluded that the frictional conditions in machining vary according to tool-workpiece combination, surrounding environment, cutting time, and cutting speed. He also pointed out that sliding will occur when soft materials are machined for short cutting times with coated tools. On the other hand, seizure conditions were attributed at high cutting speeds, long cutting times, and low hardness values between tool and work materials. Later, Wright et al. [20] defined seizure as a solid phase weld between the primary atomic layers at the interface, where the last layer of atom is stationary, and the motion is by shear velocity, gradually increasing from zero to the chip velocity. A quantity " k " was defined as the ratio of the seized area to the

real area of contact, where k lies between 0 and 1, and it is a function of tool-workpiece combination, rake angle, cutting speed, time of cut, and other environmental conditions. Some important conclusions by Wright can be summarized as: a) The actual cutting conditions are much more severe, so that experiments performed with soft-materials at low speeds will not characterize the real cutting conditions; b) experiments in vacuum favored seizure, which was attributed to the oxide free clean surfaces, c) three points are interesting in designing the cutting experiments to analyze the sticking and sliding behavior: 1) Steady state seizure pattern occurs after approximately 30 seconds, 2) Single stroke planning operations cannot represent turning operation, 3) Quick-stop mechanism does not allow a detailed examination of the interface boundary.

Oxley [10] claimed heavy frictional conditions cause the retardation of the chip velocity at the interface, thus, forming the heavily deformed thin seizure layer. However, the chip velocity never retarded completely. This thin layer was called plastic zone, and its thickness was referred as δt_2 . Another major contribution on modeling the frictional interactions at the interface was by Challen and Oxley [21], who developed a slip line field based on the asperity deformation model to explain the tribological interactions in metal cutting. This model is applicable to the sliding of a hard surface over a softer one, where the friction force is defined as the force needed to push waves of plastically deformed material along a soft surface ahead of the asperity on the hard one. In this

approach, no fracture mechanics is involved. Using the slip-line field theory, Challen and Oxley [21] proposed the coefficient of friction as:

$$\mu = \frac{A \sin \alpha + \cos(\arccos f - \alpha)}{A \cos \alpha + \sin(\arccos f - \alpha)} \quad (6)$$

where, $A = 1 + \frac{\pi}{2} + \arccos f - 2\alpha - 2 \arcsin\{(1-f)^{-1/2} \sin \alpha\}$; α is the slope of the angle of the hard asperity, and f is the normalized strength of the interfacial film. According to them, the complex processes occurring during the chip formation and chip curl influence the behavior of the chip material.

Tool-Chip Contact Area

Tool-chip contact area is an extremely important parameter for predictive modeling of chip formation. The tool-chip contact occurs as a result of the frictional conditions at the interface, and it effects the deformation within the chip and curling away of the chip from the tool rake face. Early models did not pay attention to tool-chip contact length or area since the chip was assumed to be straight, continuous, and infinite [2]. A major disadvantage of studying tool-chip contact area is the difficulty in assessing the area *in situ*. Especially in orthogonal cutting experiments, quick-stop mechanism was used to bring the chip to stop and

investigate the interface and bottom of the chip. However, quick-stop mechanism technique does not allow a detailed examination of the interface boundary.

Traces of chip flow on the tool rake face are good signs in determining the magnitude of the contact area. Takeyama and Usui [22] did the pioneering study in determination of the tool-chip contact area. Brass tubes were machined by the restricted cutting tools orthogonally, since brass has tendency to produce slight built-up edge. The restricted tool chip area varied between zero and the normal value. It was shown that the tangential force on the rake face is directly proportional to the tool-chip contact area regardless of the depth of cut, when the rake angle is zero. The frictional stress on the rake face is constant regardless of the depth of cut or rake angle and almost equal to the shearing strength of the brass. This is an indication of the fact that the apparent area of contact is equal to the real area of contact. The frictional force does not depend on the area of cut, only on the tool chip contact area. The situation is a little bit different when the rake angle is 30° , i.e., the tangential force on the rake face has a definite value, when the tool chip contact area is zero. This definite value cannot be a force originated by the tangential stress, but it is a singular point. A singular point exists at the tool edge, and the tangential component is the definite value of the tangential load. This singular load is a function of depth of cut and rake angle. However, when the rake angle is zero, the residual tangential load becomes zero, regardless of the depth of cut since the residual normal force is perpendicular to rake face. So the normal force was modeled as:

$$N = N_0 + k_2 \cdot A \quad (7)$$

where N is the normal force on the rake face; N_0 is the residual normal force; k_2 is a constant, and A is the tool-chip contact area. Furthermore, N_0 is a function of area of cut and rake angle.

$$N_0 = N_1 + k_1 \cdot A_c \quad (8)$$

where N_1 is the real residual normal force; k_1 is a constant, and A_c is the area of cut. N_1 does not contribute to the actual metal removal since it is related to the resistance against the elastic deformation of the material cut near the cutting edge or the rubbing force at the relief; k_1 can be determined from the graph of normal force vs. area of cut and k_2 from the graph of normal force vs. tool-chip contact area. The value of k_2 is constant, which is almost independent of rake angle and depth of cut.

Takeyama concluded that the tool chip contact area per unit area of cut determines the shear angle and the other machineability characteristics. A higher speed or a larger rake angle can make the tool chip contact area smaller. Tool-chip contact area is determined by the strain or stress field, or diffusibility of shearing fracture or slip ahead of the tool face, and also by the metallic affinity between the tool and work material. The strain and stress field is closely dependent on the cutting speed. Shear angle is also determined based on the fact

that the force on this tool-chip contact area is balanced with the forces within the workpiece material, i.e. the forces in the primary cutting area.

Usui and Hiroto [23] used energy method in orthogonal cutting and expressed the shear plane area and projected area of cutting cross-section and verified their cutting model by the experimental results obtained with different depth of cuts and rake angles. A very recent study performed by Guha [24] presents fractal analysis of tool-chip contact area. Raman et al. [25] further investigated the fractal nature of the sticking and sliding regions on the tool rake face. They concluded that fractal geometry of the contact region is a function of cutting speed, where the fractal dimension shows a decreasing trend with the increase in cutting speed. In using fractal analysis, they used SEM micrographs of cutting tools and image analysis.

Chip Flow

A well known chip flow model was represented by Colwell [26], where he assumed that the chip flow over the cutting face of the tool was perpendicular to the major axis of the projected area of cut (Figure 2.9).

Stabler [27] introduced his famous relationship that the chip-flow angle is equal to the inclination of the cutting edge. Armarego and Brown [28] established the new chip-flow equations based on general oblique cutting in their generalized cutting mechanics approach.

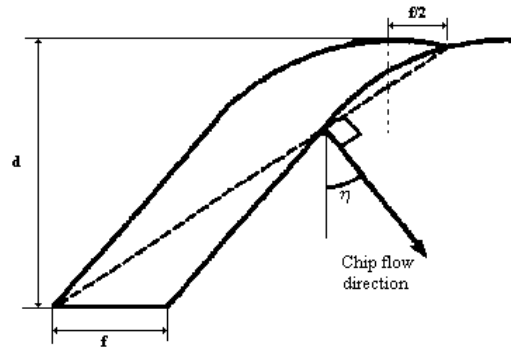


Figure 2.9. Chip flow direction model [26]

Young et al. [29] developed a chip-flow model for nose radius tools by considering the undeformed chip as a series of elements and summing up the friction forces along these elements to find the resultant chip-flow direction, where they used the experimental results of Armarego and Brown [28]. Effects of rake and inclination angles on chip flow direction were included by Wang and Mathew [30], where numerical integration methods were used along the length of the cutting edge. A simple method was employed by Arsecularatne [31] by separately taking the effects of nose radius and tool angles into consideration and using superposition of these effects. Similarly, Jawahir et al. [32] performed considerable work on modeling of cutting forces and chip flow in machining by dividing undeformed area of cut into small segments and using oblique cutting data to calculate cutting forces and chip-side flow. Ghosh [33] developed a chip flow model based on measured cutting forces and tool geometry. Cutting forces were assumed to act on the equivalent cutting edge.

Normal and Shear Stress Models

The prediction of cutting forces on the tool face is dependent on the stress distribution model along the interface and the quantitative and qualitative description of contact type between chip and tool. Since all the studies rely on the experimental evidence, there is no exact solution in analyzing the stress distribution in the literature. In most of these studies, the interfacial contact conditions were investigated, and some form of stress distribution obtained from the experimental evidence was assumed. However, there are noticeable differences between reported studies about normal and shear stress models.

Researchers used different techniques to model the stress distributions along the tool chip interface. These techniques are photoelastic tool method, split tool method and slip-line field method. In all of these techniques, however, orthogonal cutting tests were utilized.

The determination of stress distribution in the photoelastic tool method relies on the analysis of the isochromatics and isoclinics produced inside the tool under the action of cutting forces during machining. Although it is easy to use, the disadvantage of this technique is that only soft metals such as lead can be machined at very low cutting speeds because of the cutting tool material, which is usually epoxy resin that has low strength and low hot-hardness values. Also, it is not possible to determine the stress distribution accurately close to the cutting edge since the flank face force creates distortion of the isochromatic fringes [34].

The studies performed by different researchers using epoxy resin as the tool material show different stress distributions along the interface. The first studies on stress distribution were performed by Andreev [35] and Kattwinkel [36]. Andreev showed that shear stress distribution starts from zero at the chip separation point and reaches a constant value in the middle of the tool and remains constant until the cutting edge (Figure 2.10(a)-curve 2). He showed that the normal stress is increasing exponentially towards the cutting edge (Figure 2.10(b)-curve 1). Kattwinkel's results show that the shear stress falls near the cutting edge (Figure 2.10(a)-curve 3) after it reaches a maximum value in the middle part of the contact area. The normal stress distribution is the same as Andreev's. Usui and Takeyama [37] machined lead at low speed, where the shear stress distribution is as given in Figure 2.10(a)-curve 2 and the normal stress distribution is as shown in Figure 2.10(b)-curve 2. Rice et al. [38] determined the normal stress distribution when machining lead at a cutting speed of 3.05 m/min, as shown in Figure 2.10(b)-curve 3. Chandrasekaran and Kapoor [39] machined lead at low cutting speeds with different rake angle tools. The shear stress distribution is similar to the one represented by curve 2 and curve 3 in Figure 2.10(a) for positive rake angles and for negative rake angles, respectively. For all rake angles, it is found that the maximum value of the shear stress approaches the shear yield strength of the chip material. The normal stress distribution was found to remain constant for a short distance near the cutting edge and then decreased to zero (Figure 2.10(b)-curve 3). Amini [40] showed that both shear and normal stress

increase in a non-linear way from the chip separation point to the tool edge (Figure 2.10(a)-curve 1 and Figure 2.10(b)-curve 1).

In order to make the cutting conditions more representative of the actual case, Baghci and Wright [41] used a sapphire cutting tool to machine mild steels and brass, and obtained consistent results in the form of stress distribution for all the workpiece materials. Their result is similar to the findings of Chandrasekeran and Kapoor [39]. The results obtained and the experimental conditions employed in different photoelastic tool technique studies are listed in Table 2.1. The models developed by the studies are represented in Figure 2.10.

Reference	Tool Material	Workpiece Material	Rake Angle	Cutting Speed (m/min)	Result (Shear,Normal)
Andrew [35]	Epoxy	Lead	18	0.08	2 , 1
Kattwinkel [36]	Epoxy	Lead	-5	0.024	3 , 1
Usui and Takeyama [37]	Epoxy	Lead	7	0.0018	2 , 2
Rice et al. [38]	Epoxy	Lead	17.5	3.05	- , 3
Chandrasekeran & Kapoor [39]	Epoxy	Lead	0,10,20	0.0024	2 , 3
Chandrasekeran & Kapoor [39]	Epoxy	Lead	-10	0.0024	3 , 3
Amini [40]	Epoxy	Lead	10	Low	1 , 1
Baghci and Wright [41]	Sapphire	1020 Steel, Brass	-5	10-75	3 , 3

Table 2.1. Summary of photoelastic tool studies

Split tool method is another method used to determine stress distribution on the tool rake face. This method is based on the measurement of the forces acting on two separate parts of a composite cutting tool. The method of stress computation and split tool geometry is described by Arsecularatne [42].

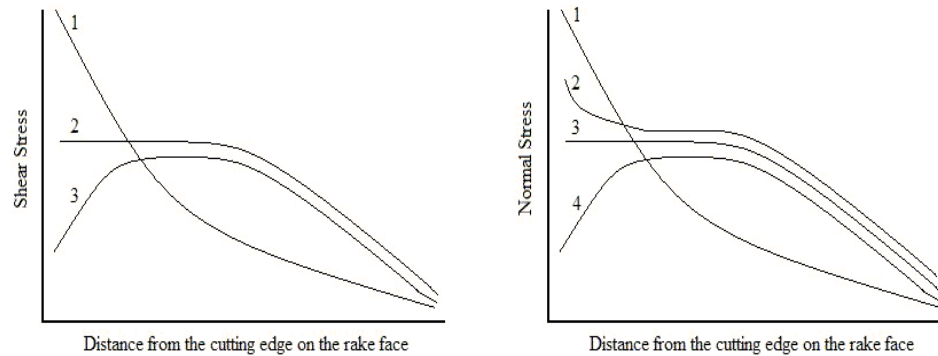


Figure 2.10. Shear and normal stress distribution models obtained by photoelastic tool and split tool methods

Since there is no restriction on tool and workpiece materials with split tool technique, high strength materials were machined at moderate to high cutting speeds. Therefore this method is more representative of the actual cutting process.

Kato et al. [43] machined aluminum, copper, zinc, and lead-tin alloy using positive rake angle HSS tools at a cutting speed of 50 m/min. The result for aluminum, copper and lead-tin alloy is given in Figure 2.10(a)-curve 2 and Figure 2.10(b)-curve 3. For zinc, the normal stress appeared to increase continuously towards the cutting edge (Figure 2.10(b)-curve 1). Usui and Shirakashi [44] machined plain carbon steel at 200 m/min. Their results showed that the shear

stress was constant near the cutting edge (Figure 2.10(a)-curve 2), and the normal stress increased continuously towards the cutting edge (Figure 2.10(b)-curve 1). Barrow et al. [34] cut nickel-chromium steel at different moderate cutting speeds and different depth of cuts. Their result indicated, in all cases, that the general form of the shear and normal stress distribution is similar to the Figure 2.10(a)-curve 2 and Figure 2.10(b)-curve 3. An interesting fact about their study is that, the length of the constant portion of the normal stress distribution is equal to that of constant shear stress distribution. Buryta et al. [45] used brass, stainless steel, medium carbon steel as the workpiece material at 130 m/min. In their study, they introduced the plowing force effect, which is the force acting in the very front portion of the cutting edge. It is believed that, although this force does not play a significant role in chip formation mechanics, it affects the stress distribution, especially at the cutting edge. The form of stress distribution after removing the plowing force effect is the same as Buryta's. In another study, Childs and Mahdi [46] machined brass, aluminum, and mild steel and obtained the same type of stress distributions. They also showed that the constant portion of the shear stress distribution and constant portion of normal stress distribution are approximately same. The results obtained and the experimental conditions employed in different split tool technique studies are listed in Table 2.2. The models developed in these studies are depicted in Figure 2.10. Compared to photoelastic tool method, the studies performed by split tool method give more consistent and correct results.

As evident from the studies above, normal and shear forces show considerably different patterns based on the method used, cutting conditions, and tool and workpiece materials. Although there are a number of studies on the interfacial cutting conditions in the literature, there is no strong foundation or model defining cutting forces and regions on which they act upon. Furthermore, all the information is experimental and the theories rely on the experimental evidence.

Reference	Tool Material	Workpiece Material	Rake Angle	Cutting Speed (m/min)	Result (Shear, Normal)
Kato [43]	HSS	aluminum, copper, lead-tin	20	50	2 , 3 2 , 1
Usui and Shirakashi [44]	Carbide	plain carbon steel	-	200	2 , 1
Barrow et al. [34]	Carbide	nickel-chromium steel	0	30, 45, 60, 90, 129	2 , 3
Buryta [45]	Carbide	brass, stainless steel, medium carbon steel	-5	130	2 , 3
Childs and Mahdi [46]	-	brass, aluminum alloy mild steel	-	-	2 , 3

Table 2.2. Summary of split tool method studies

As mentioned earlier, the slip line field technique was used to model the chip formation process. Roth and Oxley [11] used this technique to determine the shear and normal stress on the rake face. In analyzing the interface stresses, they used the experimental flow field to obtain the centre of the chip curvature. The total contact length was assumed as plastic and elastic contact. The normal stress

distribution was assumed to vary exponentially, following the photoelastic tool experiments. Within the elastic contact zone, the shear stress was assumed to be given by the product of a constant coefficient of friction and corresponding normal stress. Over the plastic contact zone, the shear stress was assumed to be constant and defined as the product of the coefficient of friction and the normal stress at the elastic-plastic contact boundary. The shear and normal stress distributions were determined so that they were consistent with the resultant forces on the rake face obtained from measured cutting forces. They conducted experiments with mild and free machining steels and at low cutting speeds. As a result, they concluded that the increase in flow stress of the workpiece material is caused by strain hardening after passing through the plastic zone; whereas, along the tool-chip interface little strain hardening occurs, and the slip lines are consistent with those of constant flow stress material. In this model, they included the cutting edge effect, which is mainly the plowing force. The drawback of this model is that the experiments were performed at low cutting speeds since their aim was to minimize the strain-rate and temperature effects.

At high speeds under practical cutting conditions, the workpiece material's flow stress properties change with strain, strain rate and temperature. Usui and Shirakashi [44] reported a simulation analysis based on a finite element method to include the variability of flow stress properties. The conditions at the tool-chip interface were assumed to be plastic near the cutting edge and elastic near the

separation point. Their results exhibit the same patterns observed in Figure 2.10(a)-curve 2, and Figure 2.10(b)-curve 1.

Another method worth mentioning here is that of Wallace and Boothroyd [15] for its significance in determining the stress distribution on the rake face. Restricted contact tools were used in machining experiments, where the tool-chip contact length is restricted by removing the rear part of the tool rake face. However, this method is not valid since by restricting the tool contact area, the chip formation mechanism changes. This does not represent actual conditions. Consequently, the obtained stresses were different than the actual ones.

CHAPTER 3

PRELIMINARY EXPERIMENTS

The following experimental tools and analysis techniques were used fully or partially in the preliminary cutting experiments. These experiments served to find the best methods and analysis techniques to further experiment and analyze the tool chip contact interface in cutting experiments.

Experimentation and Analysis Methods

Equipment:

In all of the experiments an industry type lathe, capable of changing cutting speed and feed rate, was used. A Kistler type piezoelectric dynamometer was employed to measure the cutting forces during machining. Like other piezoelectric force transducers, the stacked piezoelectric crystals respond to the applied force and generate an electric current proportional to the force. An output voltage is sent to the voltage amplifier. The voltage values are recorded based on the sampling rate with the help of data acquisition software. After averaging and multiplying with a scaling factor, the cutting forces in 3-D coordinate system can be found. The force readings were in pounds-force (lbf) after scaling. A schematic representation of the lathe and force recording setup is shown in Figure 3.1.



Figure 3.1. Industrial lathe and data acquisition system

Cutting Tools and workmaterial:

Kennametal SNG 433-K68 cutting inserts were used in the experiments. The inserts were used on a tool holder type of CSRNR-164, which assures a cutting edge angle of 15° , an inclination angle of -5° and a rake angle of -5° . Aluminum alloys (Al 2024-T351, Al 6061-T6 and Al 7075-T6) were used as workpiece materials because of good adhesion characteristics to tool surface.

Scanning Electron Microscopy:

The tool surface, where chip and tool are in contact during cutting, exhibits mainly a 3-D topography. The aerial views of the contact area can be

obtained by scanning electron microscopy (SEM). After the experiments, tool-chip contact zone was investigated by SEM at a magnification of 50x. The images were saved as grey scale image. Also, back-scattered images were taken to analyze the metallurgical composition of the tool chip area. The back-scattered image on a SEM image is based on the molecular weight of the material. The materials with higher molecular weight are lighter in grey shade than the elements with low molecular weight. The brightness and contrast of the images can be set on the SEM. For example, the white areas represent for the cutting tool (tungsten carbide), and black areas represent the workpiece (aluminum). The SEM images of the contact region, therefore, lead us to understand the mechanism of chip formation in terms of material transfer from the workpiece to the tool surface. The SEM images were taken at Sam Noble Research Center and Sarkeys Energy Center.

Surface Profilometer:

The third measuring device used in the experiments was a Tencor instrument P-1 long scan profilometer. This instrument uses a stylus to record points (in micrometers) based on a reference height as it travels horizontally. The scan length can be adjusted to cover all the contact area. Also, horizontal resolution can be set up to allow the scan to capture the actual surface profile. Then each scan point is recorded and saved in a Microsoft Excel document.

Laser Scanning Confocal Microscopy:

Sticking and built up image differentiation was not easy from a 2-D image obtained by SEM. Therefore, Laser Scanning Confocal Microscopy (LSCM) was used. Confocal microscopy facilitates reproduction of three dimensional surfaces with the finest details. LSCM gives the actual three dimensional profile of the tool-chip interface. By using the confocal imaging in its required range and resolution, the tool surface could be reproduced in graphical environment. Analyzing the 3-D images, some topographical results can be obtained in terms of intensity and depth profiling.

The LSCM at OU Health Science Center was used to scan and analyze the surface topography of the cutting tools. This process was performed by scanning the samples by LCSM, followed by analyzing the scanned images by Leica Confocal Software (LCS Lite) developed by Leica™ for the LCSM. The results of LSCM analysis of deposited layers are represented in the following pages.

Nano-indentation:

The tool-chip interface was further investigated to determine the shear stress distribution at the interface. There is evidence in the literature [47] that there is a relationship between shear stress distribution and the hardness value of a fractured surface after plastic deformation. The study was initiated to observe the

existence of such a relationship in cutting experiments and to determine the use of this technique for future study. Nano-indentation tests were performed in Microphotonics Inc.

Image Processing :

In order to find the numerical value of the areas of sticking and sliding on the cutting tool surface, image processing technique was used on the images obtained by SEM. A special software code was developed in MATLAB® to identify the areas of sticking and sliding zones. Original SEM images were cropped to the areas of interest and cleaned for unwanted debris. Then each individual image was processed by the MATLAB code.

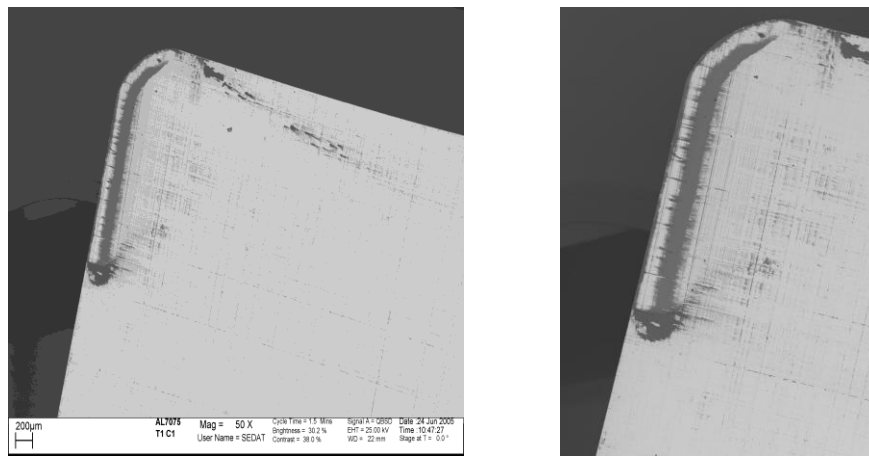


Figure 3.2. Original SEM image and the cropped and redefined image

An original SEM image showing the contact area is given in Figure 3.2. After the image size is cropped, the unwanted parts of the tool surface can be removed from the raw SEM images (Figure 3.2). In addition to the size adjustment, the brightness and contrast can be further adjusted to normalize the color values from tool to tool. The cropped and color adjusted images still contain all details and ambiguities in the sticking and sliding regions. An example of the cropped image obtained from the original SEM image is also shown in Figure 3.2.

In order to obtain values for the distinct regions of sticking and sliding, the images were further processed. The developed MATLAB® code has two parts. Before the first code is run, a color scale is established using Adobe PhotoShop and Microsoft Paint so that the image can be categorized based on color intensity. The first code performs color converting and image cleaning operations. This is achieved by converting the sticking areas to black color and the sliding areas and the tool background areas to gray color. The background of the image is set to white. This mainly filters the areas of interest and redefines the color intensities for further analysis. This cleaning code sweeps the area pixel by pixel and checks the color values of the surrounding pixels. If the original pixel does not match the surrounding pixels, it is changed to the color value of the surrounding pixels. Several resolution options for simplification of the areas were tested. It is preferable to have a resolution that simplifies the classification, without losing the image details. For this reason, the code with the 5 pixel resolution-repeating twice

was chosen. An example of image processing methodology is shown in Figure 3.3 for different resolution methods.

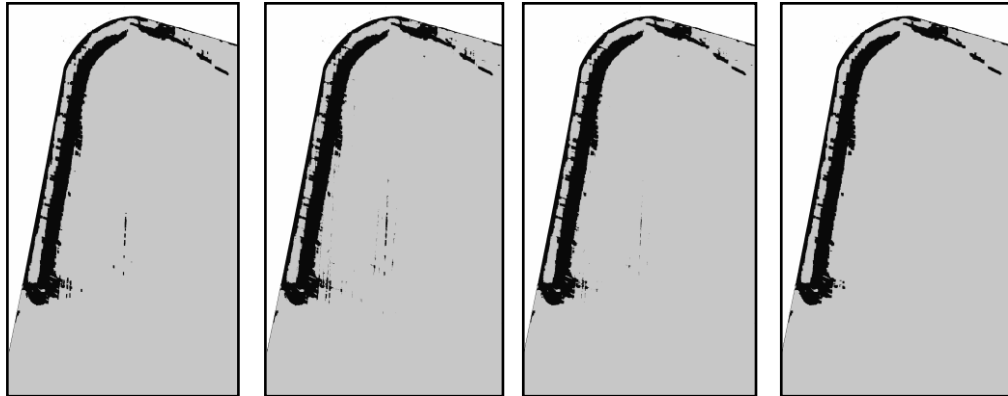


Figure 3.3. Cleaning code results (left to right): 3 pixels, 1 run; 3 pixels, 2 runs; 5 pixels, 1 run; 5 pixels, 2 runs

After completion of first code, it was necessary to manually categorize the images into sticking and sliding zones. For this reason, previously obtained images were processed manually by Microsoft Paint. Because of the edge effects near the nose radius, and at the end of depth of cut, some judgment has to be made by the user to decide what is valid sticking and what is unwanted build up from the edge effects or chip spread out. In deciding whether the area belongs to primary sticking zone or secondary sticking zone, manual adjustments are done for the overlapping regions. Once the images are categorized, each region is color coded so that second MATLAB® could read each pixel with its color intensity. Primary sticking zone color was defined as black. Sliding zone was represented

by light gray, and secondary sticking zone was colored as dark gray. The tool background area and the image background area were set to gray and white, respectively (Figure 3.4-a). The second code then produces images for each of the specified regions: Sticking, Sliding, and Total Contact Areas. For the example given in Figure 3.3, the total contact area consists of a primary sticking zone just at the front part of cutting edge, a sliding zone and a secondary sticking zone at the rear end of the contact zone, as shown in Figure 4, respectively. The second code weighs the categorized regions according to color intensity and compares each pixel. In doing so, the code identifies each pixel, its color, and its neighboring pixels. Finally, the pixel count of each color intensity is found. A conversion factor was applied to change pixels to square inches or mm^2 based on the cropped image size. As a result, the numerical values of desired regions were found. The generated MATLAB® code is provided in Appendix A.

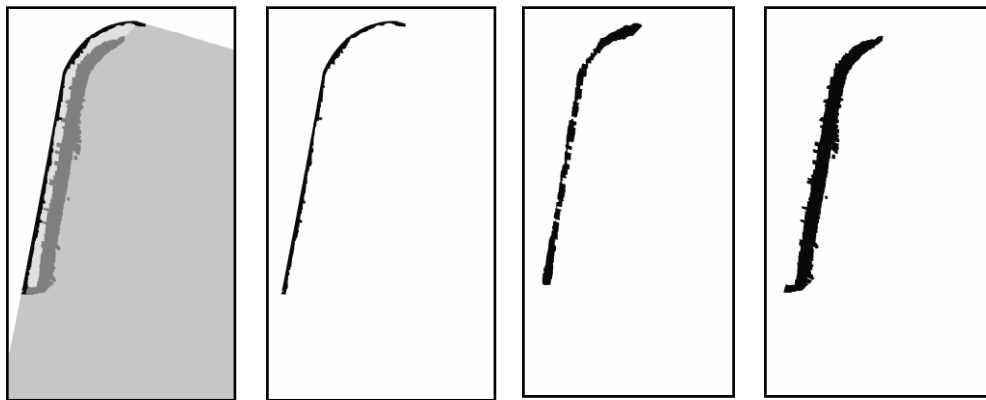


Figure 3.4. Area identification by MATLAB® code

Preliminary Experiments and Data Analysis

Repeatability Tests

These experiments were performed to validate the repeatability of cutting forces and SEM image readings. In the cutting experiments, Al-7075 material was machined by an uncoated cutting tool with 0.8 mm nose radius (SNG 432-K68) at a cutting velocity of 350 m/min. The average shear force was 5.23 N and the average normal force was 16.65 N. It was determined with 95% confidence that the measured shear force will fall between 5.11 and 5.36 N, and the measured normal force will fall between 16.44 and 16.87 N. After performing image analysis, numerical values of sticking, sliding and total area of contact were determined for the trial cuts (Figure 3.5). When comparing the types of contact area, the total contact area, sticking and sliding areas showed acceptable deviations in value - while the first sticking region and the sliding region showed significant deviations in area. The result of the area repeatability test was shown in Table 3.1, where the lower and upper boundaries are determined with 95% confidence. The deviation in the area values are due to image processing resolution and manual adjustments for the overlapping regions.

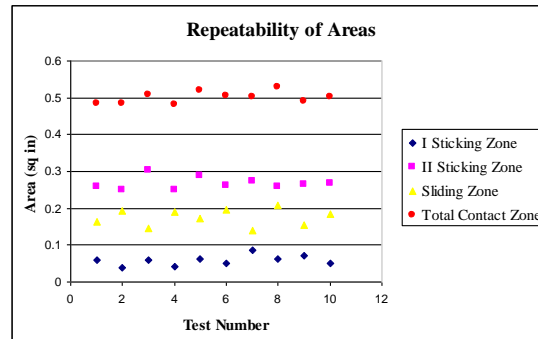
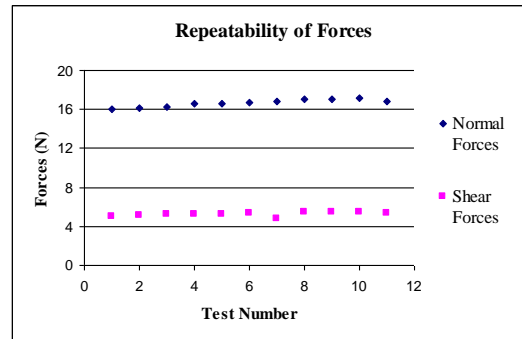


Figure 3.5. Reliability test results for the cutting force and contact area values

	Area Averages (in ²)	Lower Boundary (in ²)	Upper Boundary (in ²)	Percent Deviation from Average
Total Contact	7.755x10 ⁻⁴	7.607x10 ⁻⁴	7.903x10 ⁻⁴	1.90 %
Primary Sticking Zone	9.021x10 ⁻⁵	7.671x10 ⁻⁵	1.037x10 ⁻⁴	14.91 %
Sliding Zone	2.706x10 ⁻⁴	2.482x10 ⁻⁴	2.930x10 ⁻⁴	8.26 %
Secondary Sticking Zone	4.147x10 ⁻⁴	3.985x10 ⁻⁴	4.309x10 ⁻⁴	5.14 %

Table 3.1. Numerical values of contact area-repeatability testing

This analysis leads us to conclude that the experimental force reading and area calculations can be the input parameters to the mathematical model within acceptable error margins.

Identification of Frictional Conditions by Surface Profilometer

The chip deposited on the surface of the cutting tool was measured through the use of a surface profilometer, the cutting material being Al-7075. The general shapes observed were qualitatively categorized into three profile shapes, as can be seen in Figure 3.6.

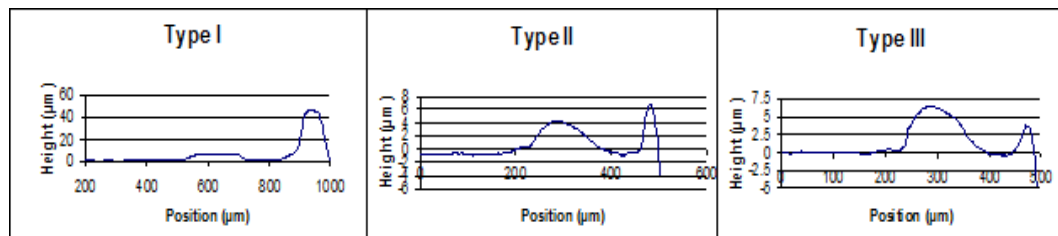


Figure 3.6. Profilometer results of tool-chip contact area for Al-7075

It was determined that there is a relationship between cutting velocity and the general shape of the material deposit. Lower cutting speed exhibited Type I behavior, indicating a primary sticking zone, where the deposited layer thickness has maximum value. Higher velocities produced Type III behavior, characterized by the secondary sticking region. The deposited layer in this zone has the maximum thickness. Low cutting forces correspond to high velocities, and high cutting forces correspond to low velocities. The magnitude of the first sticking

region was observed to be smaller for the lower forces (higher cutting speeds) and larger for the higher forces (lower cutting speeds). The magnitude of the first sticking area increases as force increases.

Identification of Frictional Conditions by LSCM

Another study was conducted to investigate and identify the sticking zone at the tool-chip interface using Al-2024 and Al-6061 as the workpiece material. This technique relies on confocal laser imaging as discussed earlier. The study focused on providing detailed information about different contact conditions and associated complex frictional mechanism at the tool-chip interface. The experiments were designed to investigate the chip tool interaction at different cutting speeds. The tool surfaces were analyzed under SEM and LSCM. The surface topography for each cutting surface was investigated and the sticking, sliding and built up edge areas were easily identified. Furthermore, LSCM verified SEM images in terms of areas of frictional contact conditions.

In situ observations were replaced by time dependent cutting experiments, i.e., the time of cut was chosen as 30 sec, 60 sec, and 90 sec and 120 sec. The experiments were conducted at cutting speeds of approximately 120, 180 and 240 m/min. The feed rate and depth of cut was kept constant at 0.142 mm/rev and 0.25 mm, respectively. The SEM images for Al-2024 for three different cutting speeds and four different cutting durations are shown in Figure 3.7. For the low cutting

speed, the built-up edge formation is obvious from the SEM images. For low-speed and 30 sec and 90 sec experiments, the built-up edge was separated from the tool surface. Therefore, it can not be seen. As the cutting speed increases, built-up edge formation is decreased. Similarly, tool-chip contact area, sticking and sliding areas are decreased. However, the quantitative measure of built-up edge and the surface topography of the chip tool interface can not be obtained from SEM images.

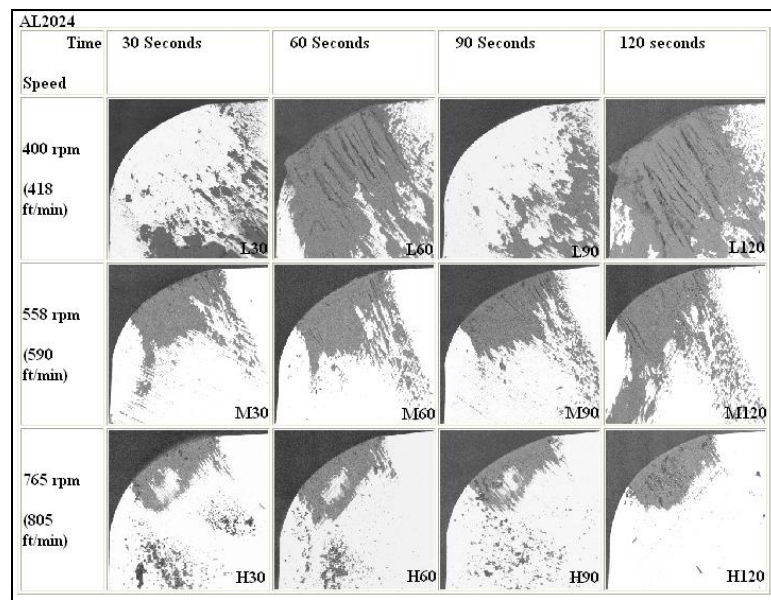


Figure 3.7. SEM images for Al-2024

SEM images for Al-6061 with the same cutting conditions are illustrated in Figure 3.8. For the low cutting speed, the built-up edge formation is obvious from the SEM images. A similar trend was observed for the built-up edge evolution, i.e., as the cutting speed increased, the built-up edge formation decreased. Total contact area, sticking and sliding areas are also decreased. Similarly, quantitative measure of built-up edge and the surface topography of the

chip tool interface can not be obtained from SEM images for Al-6061. Therefore, LSCM analysis was utilized.

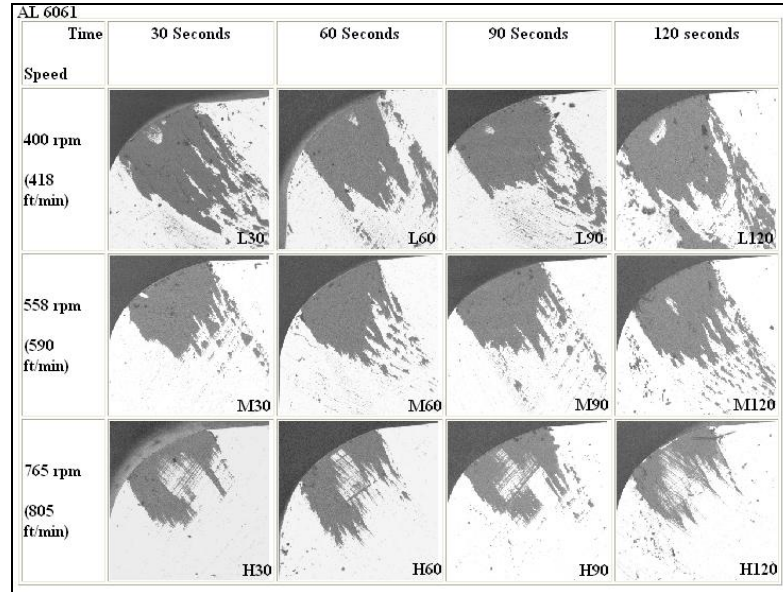
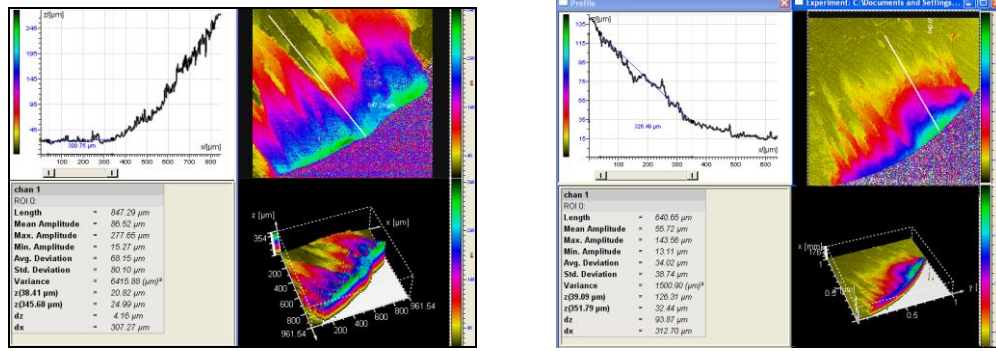


Figure 3.8. SEM images for Al-6061

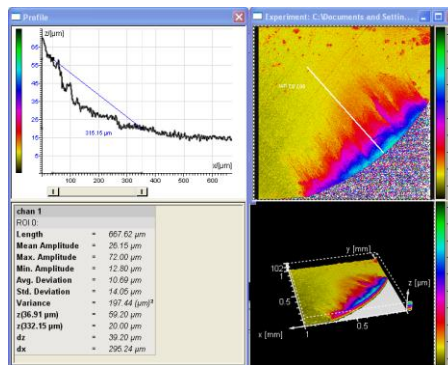
Figure 3.9 shows the images obtained by LSCM for Al-2024 for different cutting speeds and cut duration. Figure 9(a) illustrates the 3-D surface topography of the tool surface at the cutting edge for low speed (120 m/min) and 60 sec cutting time. The built-up edge formation and its shape can be easily observed from that figure. Also the 2-D aerial view enables us to get the surface profile in the direction of the cut, as shown by the white line. The line starts on the inner part of tool face and ends at the edge of tool. From this profile, it can be seen that the built-up edge has occurred at the radius edge, and it has a thickness of approximately 245 μm . As the chip flows on the tool surface, the built-up edge decreased and the sticking areas thickness was measured as 55-70 μm . The

thickness value of sliding areas is $20\ \mu\text{m}$. The 3-D surface topography of the tool surface at the cutting edge for medium speed (180 m/min) and cutting time of 90 sec is given in Figure 9(b).



(a) Low Speed Cut (60 sec)

(b) Moderate Speed Cut (90 sec)

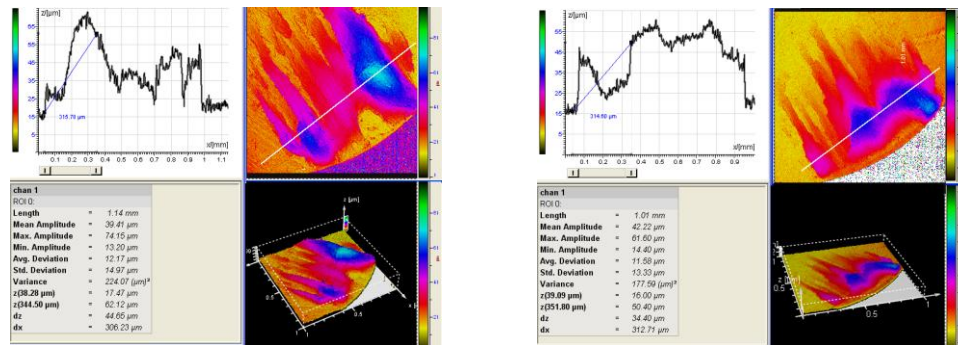


(c) High Speed Cut (90 sec)

Figure 3.9. Surface topography analysis of Al-2024 at different cutting speed and cutting times

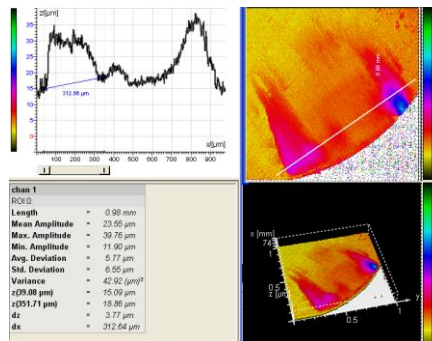
The built-up edge formation and its shape are easily identified. The built-up edge formation has a thickness value of $45\text{-}55\ \mu\text{m}$. As the chip flows on the tool surface, the built-up edge formation disappears and sticking takes place,

which shows a maximum thickness of 25 μm . The sliding areas have a thickness of 15 μm . Figure 9(c) shows the 3-D surface topography of the tool surface at the cutting edge for high speed (240 ft/min) and cutting time of 90 sec. The built-up edge is limited to the nose radius again, with a built-up edge thickness of 30-45 μm . As the chip flows on the tool surface, the built-up edge formation cheeses and sticking takes place with a thickness value of 20-25 μm . The sliding areas level at 15 μm .



(a) Low Speed Cut (60 sec)

(b) Moderate Speed Cut (90 sec)



(c) High Speed Cut (90 sec)

Figure 3.10. Surface topography analysis for Al-6061 at different cutting speed and cutting times

Figure 3.10 illustrates the surface topography images obtained by LSCM where the deposited layer is Al-6061. 3-D surface topography of the tool surface at the cutting edge for low speed (120 ft/min) and cutting time of 60 sec is shown in Figure 3.10(a). The built-up edge formation and its shape are also easily identified for low speed cutting of Al-6061 as shown in that figure. The built-up edge formation has a thickness value of 45-65 μm . The sticking areas level off at 25-30 μm , whereas the sliding areas show a thickness value of 15-20 μm . Similar behavior was observed with moderate and high cutting speeds, with the sticking and sliding zones having 25 μm and 15 μm thickness values, respectively for moderate cutting speed. The thickness values are 20-25 μm . in sticking region, and 15 μm in sliding region for high cutting speed (Figure 3.10(b)-(c)). The thickness values of corresponding areas for different cutting speeds cutting times and materials are summarized in Table 3.2.

Material	Speed (m/min)	Tool Chip Contact			Explanation
		Built-Up (μm)	Sticking (μm)	Sliding (μm)	
AL-2024	120	245	55-70	20	Large Built-Up
	180	115-135	25-50	20	Moderate Built-Up
	240	45-65	25-35	15-20	Low Built-Up
AL-6061	120	45-65	25-30	15-20	Large Built-Up
	180	45-55	25	15	Moderate Built-Up
	240	30-45	20-25	15	Low Built-Up

Table 3.2. Results of LSCM imaging

The low speed cutting is very prone to built-up edge formation. As the cutting speed increases, the built-up edge formation decreases, which is as expected since there is not sufficient time for the chip to stick on a previously adhered surface when the cutting velocity is high. Moreover, with the increase in cutting speed, the compressive cutting forces decrease. Also, the high speed chip carries away the built-up layer. However, since the difference can not be obtained in a backscattered image in terms of topology, it is impossible to distinguish the sticking areas from the built-up edge areas. Therefore the samples further investigated by LSCM.

The areas of sticking, sliding and built-up edge can easily be identified since LSCM gives the surface points in terms of its relative height with respect to the reference surface, i.e., tool surface. If the surface profiles are investigated carefully, it can be seen that the built-up edge formation of the two materials are different. At low speed, built-up edge of Al-2024 has a thickness value of 245 μm , whereas Al-6061 has the peak value of 65 μm . Similar characteristic is observed for the moderate and high speed cuts. However, the difference between the peak values of built-ups for both materials is decreased at high speeds. The same phenomenon can also be seen in sticking zones, but the difference is not as large as it is in the built-up region. This means that Al-6061 and Al-2024 have tendency to adhere to the tool surface, and this characteristics is dependent on cutting parameters. This conclusion can also be obtained also when the pattern of each different zone is investigated for the two materials.

3-D surface topography visualization, by itself, is satisfactory to distinguish the sticking area and built-up edge. All the 3-D pictures show built-up edge as high intensity colors compared to the sticking area. In that respect, LSCM has been found to be a promising tool to investigate the tool chip interface.

SEM Backscattering

SEM images serve further to identify the metallographic analysis of contact zones. The tool-chip contact area is divided into three regions: a) primary sticking zone, close to the edge, b) sliding zone, and c) secondary sticking zone at the rear end of the contact, as shown in Figure 3.11.

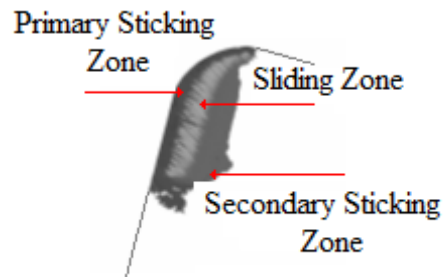


Figure 3.11. Backscattered image of tool-chip contact area, showing different frictional conditions

When modeling interfacial frictional conditions at the tool-chip contact area, it is important to consider the changes in the structure and physical properties of workpiece material. The deposits on the cutting tools were further

analyzed by SEM backscattering tool to get the compositional differences at different locations. Al-2024 is an aluminum-copper alloy and its composition is: Si 0.50%, Fe 0.50%, Cu 4.90%, Mn 0.90%, Mg 1.50%, Cr 0.10%, Zn 0.25%, Ti 0.15%. AL2024 is a soft material, but it gains its strength mainly from the presence of fine hard precipitates, which obstructs the dislocation in the material. Heat treatment and quenching of the alloy forms an unstable supersaturated solid solution and prevents the formation of large precipitates in it. These alloys are then aged at elevated temperatures, allowing the formation of fine precipitates in the alloy to impart strength to the material [48, 49]. CuAl_2 and Mg_2Si precipitates formed during age hardening are mainly responsible for the increase in strength of all Al-2024. The built-up on the tool rake face shows two distinct shades of grey of sticking work-material. The front end of the sticking material is dark grey and the later part is in lighter shade in the backscatter image, indicating a higher molecular weight as seen in Figure 3.12.

The chemical composition of front and back part of the built-up areas is illustrated in Figure 3.12(a) and (b), respectively. When the chemical composition is analyzed, the secondary sticking zone shows a high concentration of copper (35.73 %) in weight (Figure 3.12(b)); whereas, the primary sticking zone has a copper concentration of only 4.41 % in weight (Figure 3.12(a)). After passing the plastic deformation zone, aluminum acts like a fluid. It carries the alloying elements inside the matrix which have higher melting points. It is speculated that as the chip flows on the tool surface, the chip loses heat and its temperature drops,

turning the fluidic metal into a solid, open to oxidation and prone to sticking with its alloying elements. Therefore, the copper concentration is higher than that was observed at the tool edge.

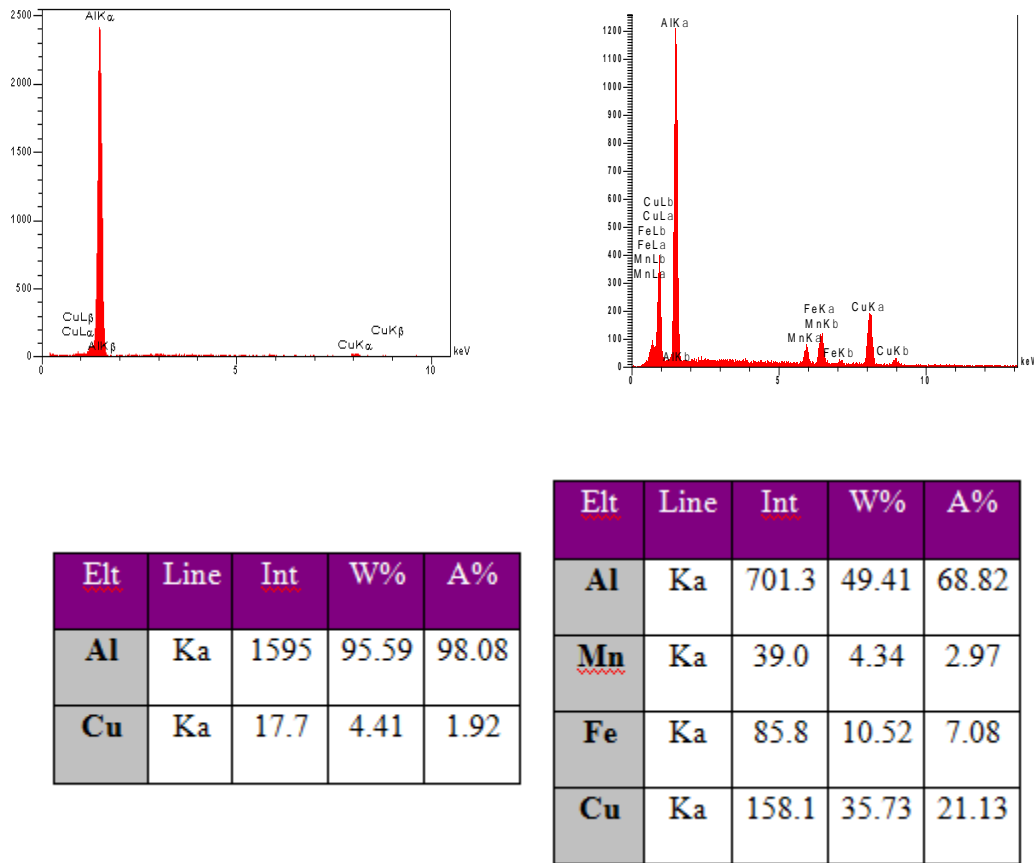


Figure 3.13. Elemental scan and chemical composition of sticking areas:

(a) Primary sticking zone, (b) Secondary sticking zone

Nano-indentation Test

Nano-indentation tests were performed after the cutting experiments on the Al-6061 workmaterial adhered on the tool surface. The surface flatness plays

an important role in indentations. Finding a flat spot is the key element to obtain satisfactory results in indentation experiments. The surface of the built-up layer was searched for flat areas, and two indentations were performed. The indenter type was a Barkovic indenter. The depth of indentations was kept at 1 μm range. The results of the indentation tests are shown in Table 3.3.

The elastic modulus and surface hardness were determined at those two spots. The elastic modulus values at the surface are close to each other and to the bulk elastic modulus value; whereas, hardness values differ. This is an indication that the hardness profile differs on the surface and there is no evidence between hardness and shear stress. It is speculated in reference [47] that there is a relationship between hardness and shear stress values in a plastically deformed material. However, this initiated study failed since it did not give the relationship between the shear stress and hardness value over the tool-chip interface.

Test #	E Average GPa	H Average GPa	Modulus Unload GPa	Hardness Unload GPa	Drift Correction nm/s
1	64.407	1.374	79.989	1.372	0.122
2	71.109	1.956	105.012	2.405	0.108
Mean	52.128	1.184	104.804	2.175	0.108
Std. Dev.	27.278	0.883	24.711	0.716	0.015
% COV	52.33	74.64	23.58	32.94	13.94

Table 3.3. Elastic modulus and hardness values of Al-6061 at the tool-chip interface

CHAPTER 4

MAIN EXPERIMENTS AND DATA ANALYSIS

The results of preliminary experiments lead us to further investigate the cutting process at the microscopic level. Post-mortem experiments were conducted and analyzed by the feasible methods described in the previous section. These experiments were designed and conducted with the following variables:

Control Variables:

- Cutting Speed (m/min) : 110, 225, 335, 470
- Feed rate (mm/rev): 0.071, 0.198, 0.325
- Depth of Cut (mm): 0.51, 1.27, 2.03, 2.79
- Material: Al-2024, Al-6061

Response Variables:

- Cutting Forces (N)
- Tool-Chip Contact Area (SEM Images)

Fixed Variables:

- Cutting Tool
- Auxiliary Cutting Conditions (time, dry cut)

A total of 96 experiments were performed for further analysis. Cutting forces, contact surface area values and material composition of deposited layers on contact areas were compared with respect to uncut chip areas (A_{uc}) and d/f ratio. Especially d/f ratio is a non-dimensional variable that combines depth of cut

and feed rate as a control variable. The following table shows the variation of uncut chip area and d/f ratio for the experiments performed in this study.

Depth of Cut (mm ²)		Feed rate (mm/rev)		
		0.071	0.198	0.305
0.51	A _{uc}	0.0361	0.1006	0.1548
	d/f	7.1429	2.5641	1.6667
1.27	A _{uc}	0.0903	0.2516	0.3871
	d/f	17.8571	6.4103	4.1667
2.03	A _{uc}	0.1445	0.4026	0.6194
	d/f	28.5714	10.2564	6.6667
2.79	A _{uc}	0.1987	0.5535	0.8516
	d/f	39.2857	14.1026	9.1667

Table 4.1. Uncut cheap area and d/f ratio for the depth of cut and feed rates used in the experiments

In the methodology of experiment, cutting forces were measured during the experiments continuously and tool-chip contact areas on the cutting tools were characterized by SEM methods after the experiments. SEM image analysis was conducted for three purposes:

- SEM images were helpful in visualizing the deposits on the tool surface which defines sticking and sliding zones and even identifying built-up edge formation.

- SEM images were further analyzed by the image analysis tool, as explained earlier. Numerical values of sticking and sliding area on the cutting tool surface were determined by image processing technique. The end result is numerical area values in mm^2 or in^2 .
- Additionally, the deposits on the cutting tools were analyzed by SEM backscattering technique to identify and quantify the compositional differences. The elemental mapping was constructed based on weight percentage.

SEM Image Analysis

Tool Chip Contact Area Quantification

SEM images obtained after cutting experiments show how the cutting parameters effect the frictional contact zone formation. Since the tool surface has a finite surface roughness value and lay, the chip underneath surface fills the tool surface irregularities first. This was observed as continuous dark lines on the sliding zone and disregarded as sticking formation. The original SEM images of the contact zone for each cutting condition are shown in Appendix A. The noise data in SEM images were eliminated by manual processing after careful investigation of the chip contact zones. As a result, modified chip contact area images were obtained.

AL-2024 Experiments










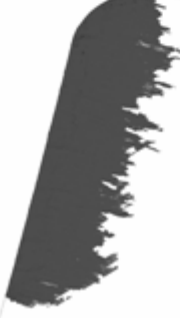
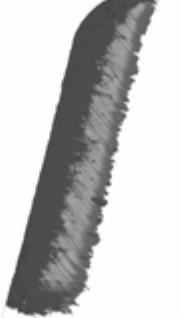

N=400 rpm	f = 0.071 mm/rev	f = 0.198 mm/rev	f = 0.305 mm/rev
d = 0.51 mm	Ac=0.0361 mm ² 	Ac=0.1006 mm ² 	Ac=0.1548 mm ² 
d = 1.27 mm	Ac=0.0903 mm ² 	Ac=0.2516 mm ² 	Ac=0.3871 mm ² 
d = 2.03 mm	Ac=0.1445 mm ² 	Ac=0.4026 mm ² 	Ac=0.6194 mm ² 
d = 2.79 mm	Ac=0.1987 mm ² 	Ac=0.5535 mm ² 	Ac=0.8516 mm ² 

Figure 4.1. Modified SEM images of tool-chip contact area for cutting experiments of AL-2024 at 110 m/min, different feed rates and depths of cut













N=658 rpm	f = 0.071 mm/rev	f = 0.198 mm/rev	f = 0.305 mm/rev
d = 0.51 mm	Ac=0.0361 mm ² 	Ac=0.1006 mm ² 	Ac=0.1548 mm ² 
d = 1.27 mm	Ac=0.0903 mm ² 	Ac=0.2516 mm ² 	Ac=0.3871 mm ² 
d = 2.03 mm	Ac=0.1445 mm ² 	Ac=0.2516 mm ² 	Ac=0.3871 mm ² 
d = 2.79 mm	Ac=0.1445 mm ² 	Ac=0.4026 mm ² 	Ac=0.6194 mm ² 

Figure 4.2. Modified SEM images of tool-chip contact area for cutting experiments of AL-2024 at 225 m/min, different feed rates and depths of cut













N=765 rpm	f = 0.071 mm/rev	f = 0.198 mm/rev	f = 0.305 mm/rev
d = 0.51 mm	Ac=0.0361 mm ² 	Ac=0.1006 mm ² 	Ac=0.1548 mm ² 
d = 1.27 mm	Ac=0.0903 mm ² 	Ac=0.2516 mm ² 	Ac=0.3871 mm ² 
d = 2.03 mm	Ac=0.1445 mm ² 	Ac=0.4026 mm ² 	Ac=0.6194 mm ² 
d = 2.79 mm	Ac=0.1987 mm ² 	Ac=0.5535 mm ² 	Ac=0.8516 mm ² 

Figure 4.3. Modified SEM images of tool-chip contact area for cutting experiments of AL-2024 at 335 m/min, different feed rates and depths of cut













N=1350 rpm	f = 0.071 mm/rev	f = 0.198 mm/rev	f = 0.305 mm/rev
d = 0.51 mm	Ac=0.0361 mm ² 	Ac=0.1006 mm ² 	Ac=0.1548 mm ² 
d = 1.27 mm	Ac=0.0903 mm ² 	Ac=0.2516 mm ² 	Ac=0.3871 mm ² 
d = 2.03 mm	Ac=0.1445 mm ² 	Ac=0.4026 mm ² 	Ac=0.6194 mm ² 
d = 2.79 mm	Ac=0.1987 mm ² 	Ac=0.5535 mm ² 	Ac=0.8516 mm ² 

Figure 4.4. Modified SEM images of tool-chip contact area for cutting experiments of AL-2024 at 470 m/min, different feed rates and depths of cut

Figures 4.1- 4.4 represent the modified images for Al-2024. According to these figures, the tool-chip contact area show a dynamic behavior at different cutting conditions. However, one obvious conclusion is the formation of different interfacial contact zones; namely primary sticking zone, close to edge; sliding zone following the primary sticking zone, and secondary sticking zone at the rear end of the contact.

Depth of cut (mm)	Zone	Feed rate (mm/rev)		
		0.071	0.198	0.305
0.51	Prim. Sticking	0.2727	0.3155	0.2990
	Sliding	0	0.0097	0.1444
	Sec. Sticking	0	0	0.0716
1.27	Prim. Sticking	0.5737	0.4903	0.5050
	Sliding	0	0.2021	0.3681
	Sec. Sticking	0	0.0464	0.1280
2.03	Prim. Sticking	0.9026	0.6615	0.6520
	Sliding	0	0.2960	0.6103
	Sec. Sticking	0	0.1324	0.1930
2.79	Prim. Sticking	1.1326	0.8654	0.8179
	Sliding	0	0.3950	0.7900
	Sec. Sticking	0	0.2847	0.2988

Table 4.2. Primary sticking, sliding and secondary sticking area values for Al-2024 at 110 m/min

Analysis of the modified SEM images of Al-2024 revealed an interesting pattern in the magnitude and evolution of the frictional contact boundaries.

Numerical values of each contact zone is provided in Table 4.2 and shown in Figure 4.5. At low cutting speed (110 m/min), primary sticking zone has the largest magnitude.

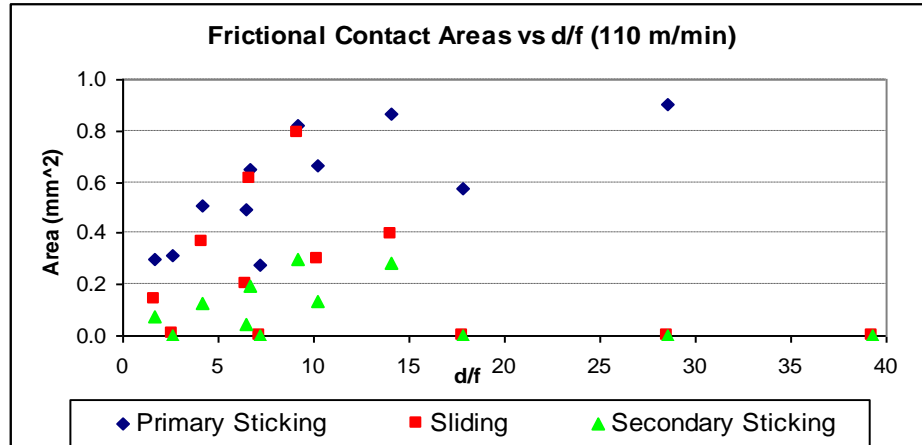


Figure 4.5. Frictional contact areas vs d/f for Al-2024 at 110 m/min

Furthermore, there is only sticking for low feed rate irrespective of depth of cut. This zone is mainly built-up layer because of low feed rate, depth of cut, and low speed. As the feed rate increases, sliding is observed to emerge and enlarge in magnitude. At deeper cuts and higher feed rates, secondary sticking zone is observed as a narrow band.

The chemical composition of material layer deposited on the preliminary and secondary sticking zones at 110 m/min cutting speed is given in Figure 4.6. This data supports the SEM images and different chemical composition of sticking zones on the contact area. In the primary sticking zone, sticking layer composition is very similar to chemical content of Al-2024 at room temperature.

However, the chemical composition changes on the secondary sticking zone. Copper content increases to approximately 48% and aluminum content decreases to 50% especially at high feed rates and depth of cuts.

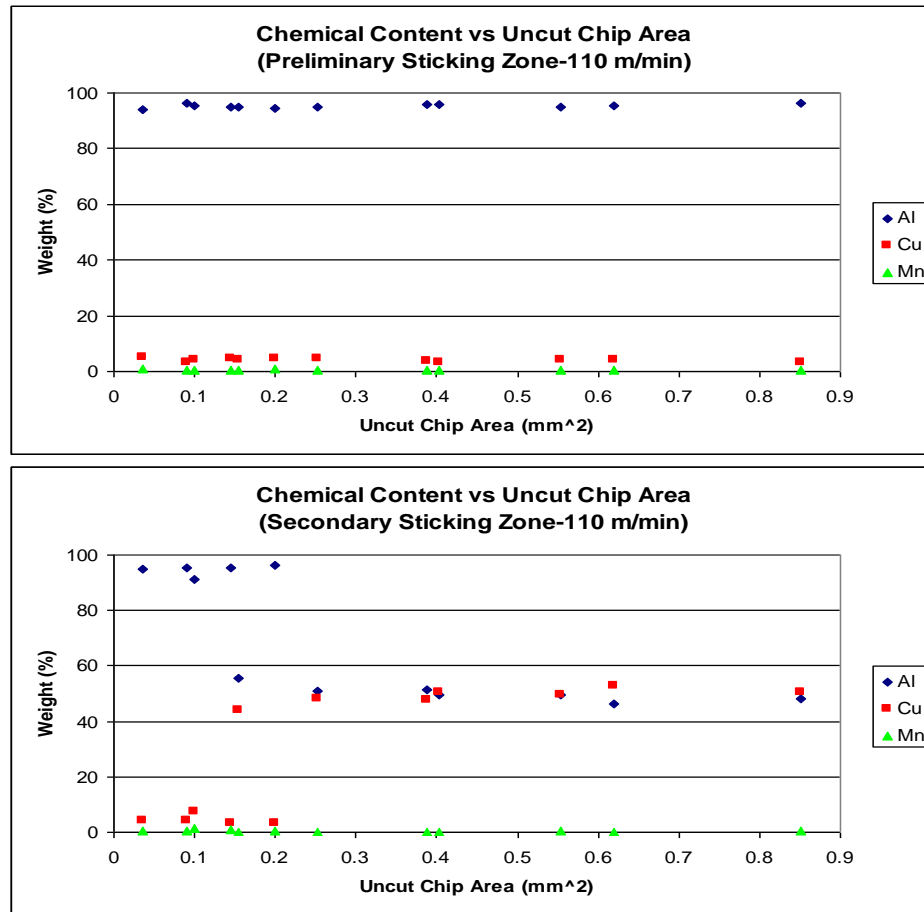


Figure 4.6. Chemical composition of primary and secondary sticking zones for Al-2024 at 110 m/min

When the cutting speed increases (225 m/min), secondary sticking area starts to develop and enlarge with the increase in feed rate and depth of cut. The built-up layer spread seen in the primary sticking zone decreases when compared

to the results of low cutting speed experiments. This change can be seen in Figure 4.7 and noted by comparing the area of each zone as tabulated in Table 4.3 with that of low cutting speed experiments. The chemical composition of material layer deposited on the primary and secondary sticking zones for 225 m/min cutting speed is given in Figure 4.8. The elemental analysis in the primary sticking zone is the same as it was in the low cutting speed. The chemical composition of adhesion layer in the preliminary sticking zone is observed as 93.5 ± 1 % Al, 4.5 ± 0.5 % Cu, 1.0 ± 0.1 Mn and 1.0 ± 0.1 other elements, which is typical for Al-2024 material.

Depth of cut (mm)	Zone	Feed rate (mm/rev)		
		0.071	0.198	0.305
0.51	Prim. Sticking	0.0673	0.0696	0.1301
	Sliding	0.0191	0.1081	0.1164
	Sec. Sticking	0.0305	0.1670	0.1982
1.27	Prim. Sticking	0.1576	0.1523	0.2113
	Sliding	0.1047	0.2404	0.2559
	Sec. Sticking	0.1525	0.4159	0.4322
2.03	Prim. Sticking	0.2763	0.2572	0.3419
	Sliding	0.1573	0.3947	0.3832
	Sec. Sticking	0.2981	0.7200	0.7717
2.79	Prim. Sticking	0.4739	0.4618	0.4634
	Sliding	0.2098	0.5121	0.4844
	Sec. Sticking	0.4110	0.8733	1.1365

Table 4.3. Primary sticking, sliding and secondary sticking area values for Al-2024 at 225 m/min

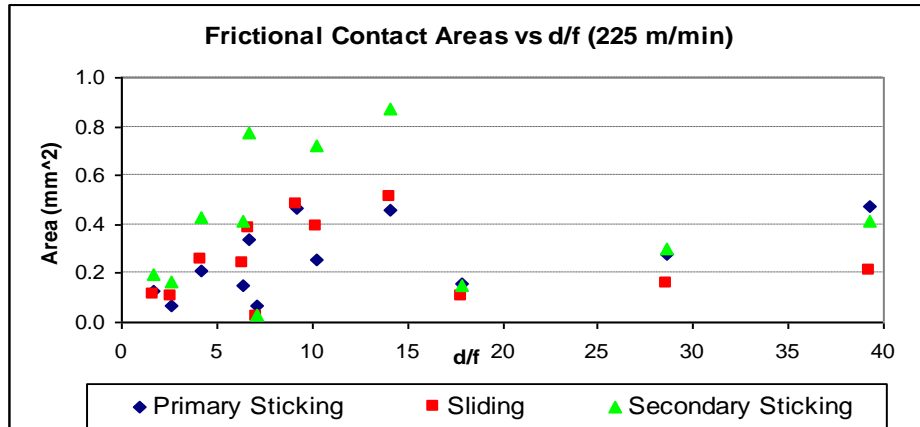


Figure 4.7. Frictional contact areas vs d/f for Al-2024 at 235 m/min

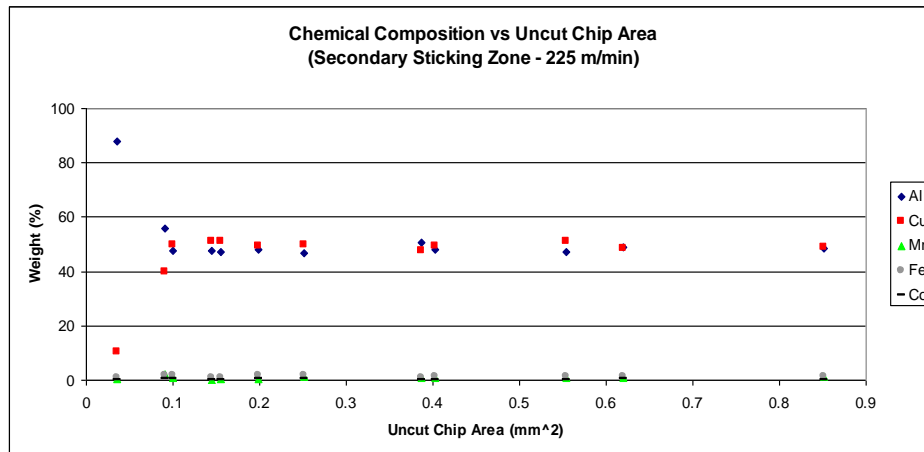
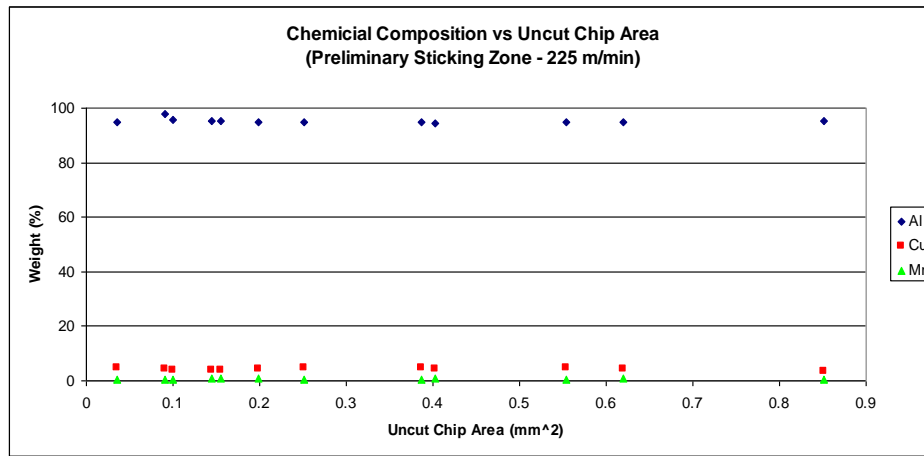


Figure 4.8. Chemical composition of primary and secondary sticking zones for Al-2024 at 225 m/min

A significant difference is observed in the secondary sticking zone. At low feed rate and small depth of cut, the base composition of Al-2024 does not change. With an increasing federate and depth of cut, aluminum content decreases to approximately 50% and copper content increases to approximately 49%, drastically. This is the effect of thermal softening with increasing speed. The original elemental composition is only observed for the minimum uncut chip area and feed rate.

Depth of cut (mm)	Zone	Feed rate (mm/rev)		
		0.071	0.198	0.305
0.51	Prim. Sticking	0.0451	0.0800	0.1044
	Sliding	0.0364	0.1131	0.1319
	Sec. Sticking	0.0672	0.1766	0.1895
1.27	Prim. Sticking	0.0802	0.1357	0.1759
	Sliding	0.1330	0.2530	0.3485
	Sec. Sticking	0.1178	0.2544	0.3225
2.03	Prim. Sticking	0.1568	0.1723	0.2210
	Sliding	0.2207	0.4028	0.5641
	Sec. Sticking	0.1253	0.5459	0.5109
2.79	Prim. Sticking	0.2494	0.2737	0.3106
	Sliding	0.2770	0.4715	0.6655
	Sec. Sticking	0.1841	0.7307	0.7757

Table 4.4. Primary sticking, sliding and secondary sticking area values for Al-2024 at 335 m/min

With a further increase in cutting speed 335 (m/min), primary sticking zone decreased slightly; the sliding zone moved to the front and secondary sticking zone increased. The modified SEM images shown in Figure 4.3 depict this change. Table 4.4 and Figure 4.8 show the difference in zone formation for this cutting speed.

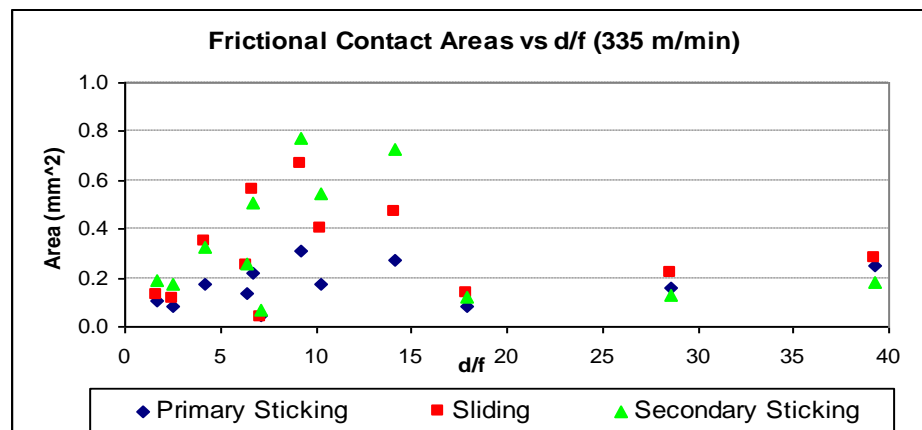


Figure 4.9. Frictional contact areas vs d/f for Al-2024 at 335 m/min

The elemental composition of the primary cutting zone does not change at 335 m/min cutting experiments. The same observation with cutting speeds of 110 m/min and 225 m/min are valid at this speed for the primary sticking zone. Secondary sticking zone, on the other hand exhibits a different result. Copper content drops to 34-36%, manganese content increases to 3.5%, and the composition of other elements increases slightly. This data is shown in Figure 4.9.

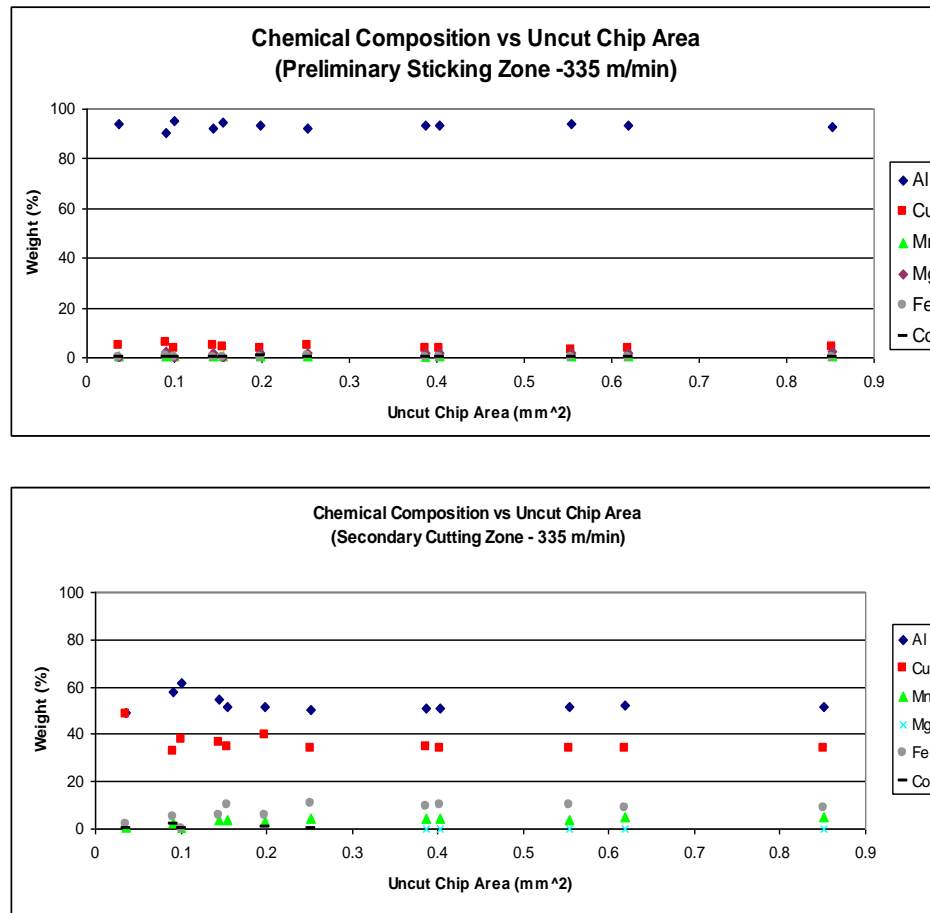


Figure 4.10. Chemical composition of primary and secondary sticking zones for Al-2024 at 335 m/min

Cutting experiments at 470 m/min show similar results as 335 m/min experiments. The area of preliminary zone decreases slightly, moving the sliding zone further to the cutting edge and secondary sticking zone further increases, as can be seen from Table 4.5 and Figure 4.10. The preliminary sticking zone chemical composition does not change and agrees with that of lower cutting speed experiments. However, the copper content in the secondary sticking zone further

decreases to 34% and manganese content increases to 4.3%. Figure 4.11 shows the chemical composition change of sticking zones at highest cutting speed

Depth of cut (mm)	Zone	Feed rate (mm/rev)		
		0.071	0.198	0.305
0.51	Prim. Sticking	0.0543	0.0484	0.0634
	Sliding	0.0444	0.0998	0.1553
	Sec. Sticking	0.1118	0.1880	0.2371
1.27	Prim. Sticking	0.1059	0.1150	0.1219
	Sliding	0.1284	0.2605	0.2949
	Sec. Sticking	0.1996	0.4329	0.4678
2.03	Prim. Sticking	0.1660	0.1859	0.2006
	Sliding	0.1929	0.3953	0.5666
	Sec. Sticking	0.3069	0.7380	0.6254
2.79	Prim. Sticking	0.2436	0.2872	0.3033
	Sliding	0.2593	0.5122	0.7557
	Sec. Sticking	0.3943	0.8626	0.7567

Table 4.5. Primary sticking, sliding and secondary sticking area values for Al-2024 at 470 m/min

Chemical composition results show that with increasing speed the energy dissipated to the tool increases and the temperature on the contact zone increases. The increase in contact zone changes the phase structure of the aluminum. As known, aluminum forms hard and brittle metallic compounds with Cu, Mg and Fe into Al_2Cu , Al_3Mg_2 , Al_3Fe . The phase diagram of aluminum alloys indicates that

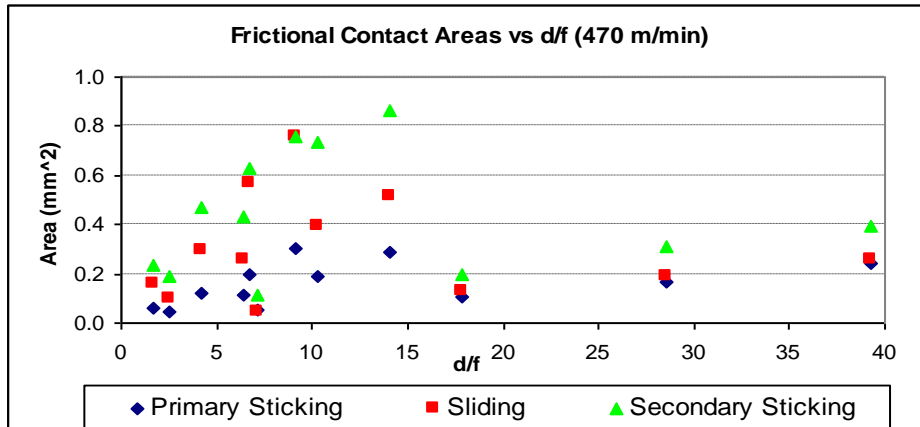


Figure 4.11. Frictional contact areas vs f/d for Al-2024 at 470 m/min

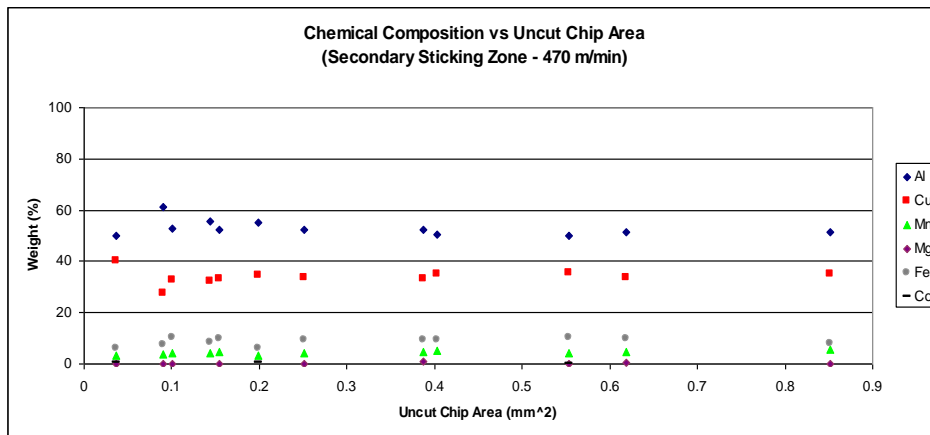
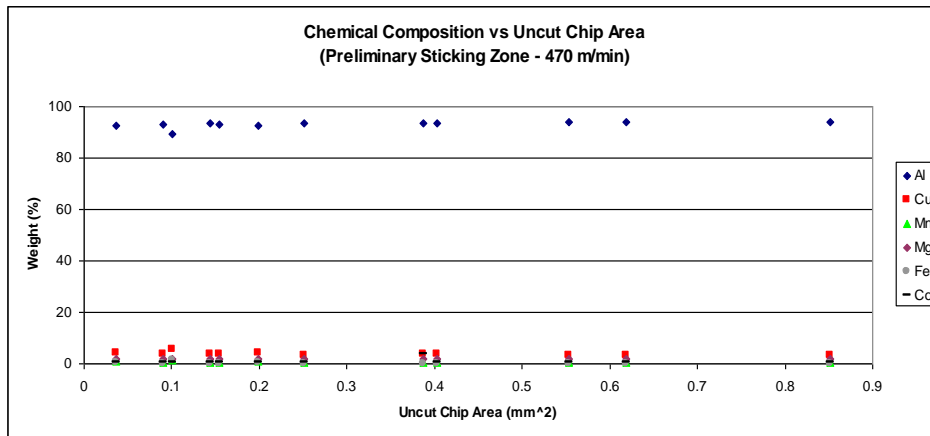


Figure 4.12. Chemical composition of primary and secondary sticking zones for Al-2024 at 470 m/min

microstructure of Al-2024 at room temperature or low cutting speeds consist of a mild, deformable alfa-solid solution. However, at elevated temperatures corresponding to high cutting speeds, depth of cut and feed rates, the microstructure changes; metallic compounds formed by aluminum and its alloying elements. These are the general observations from the cutting experiments of Al-2024.

AL-6061 Experiments

Modified SEM images for the experiments conducted with Al-6061 can be seen in Figures 4.12 - 4.15. In order to be consistent, the feed rate and depth of cut was kept as constant control variables, resulting in same uncut chip area and d/f ratio given in Table 4.1.

Cutting speeds were adjusted such that the experimental results can be compared with the results of experiments with Al-2024. Analysis of the modified SEM images of Al-6061 shows a slightly different evolution of sticking and sliding zone pattern. At a low cutting speed (120 m/min), there is no secondary sticking zone observed. Also, for low feed rates, everything occurs on the primary sticking zone; even no sliding zone is the characteristics of this cutting condition. Built-up edge is more dominant in Al-6061 for low cutting speed.










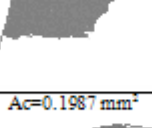
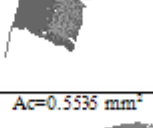
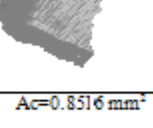
N=400 rpm	f = 0.071 mm/rev	f = 0.198 mm/rev	f = 0.305 mm/rev
d = 0.51 mm	Ac=0.0361 mm ² 	Ac=0.1006 mm ² 	Ac=0.1548 mm ² 
d = 1.27 mm	Ac=0.0903 mm ² 	Ac=0.2516 mm ² 	Ac=0.3871 mm ² 
d = 2.03 mm	Ac=0.1445 mm ² 	Ac=0.4026 mm ² 	Ac=0.6194 mm ² 
d = 2.79 mm	Ac=0.1987 mm ² 	Ac=0.5536 mm ² 	Ac=0.8516 mm ² 

Figure 4.13. Modified SEM images of tool-chip contact area for cutting experiments of AL-6061 at 120 m/min, different feed rates and depths of cuts.








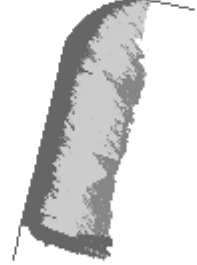
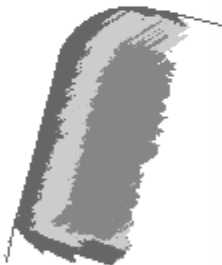
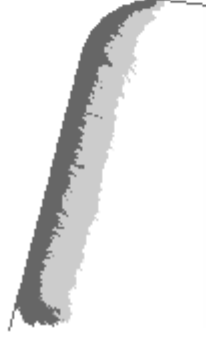


N=658 rpm	f = 0.071 mm/rev	f = 0.198 mm/rev	f = 0.305 mm/rev
d = 0.51 mm	Ac=0.0361 mm ² 	Ac=0.1006 mm ² 	Ac=0.1548 mm ² 
d = 1.27 mm	Ac=0.0903 mm ² 	Ac=0.2516 mm ² 	Ac=0.3871 mm ² 
d = 2.03 mm	Ac=0.1445 mm ² 	Ac=0.4026 mm ² 	Ac=0.6194 mm ² 
d = 2.79 mm	Ac=0.1987 mm ² 	Ac=0.5535 mm ² 	Ac=0.8516 mm ² 

Figure 4.14. Modified SEM images of tool-chip contact area for cutting experiments of AL-6061 at 230 m/min, different feed rates and depths of cuts.













N=765 rpm	f = 0.071 mm/rev	f = 0.198 mm/rev	f = 0.305 mm/rev
d = 0.51 mm	Ac=0.0361 mm ² 	Ac=0.1006 mm ² 	Ac=0.1548 mm ² 
d = 1.27 mm	Ac=0.0903 mm ² 	Ac=0.2516 mm ² 	Ac=0.3871 mm ² 
d = 2.03 mm	Ac=0.1445 mm ² 	Ac=0.4026 mm ² 	Ac=0.6194 mm ² 
d = 2.79 mm	Ac=0.1987 mm ² 	Ac=0.5535 mm ² 	Ac=0.8516 mm ² 

Figure 4.15. Modified SEM images of tool-chip contact area for cutting experiments of AL-6061 at 345 m/min, different feed rates and depths of cut








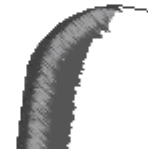




N=1350 rpm	f = 0.071 mm/rev	f = 0.198 mm/rev	f = 0.305 mm/rev
d = 0.51 mm	Ac=0.0361 mm ² 	Ac=0.1006 mm ² 	Ac=0.1548 mm ² 
d = 1.27 mm	Ac=0.0903 mm ² 	Ac=0.2516 mm ² 	Ac=0.3871 mm ² 
d = 2.03 mm	Ac=0.1445 mm ² 	Ac=0.4026 mm ² 	Ac=0.6194 mm ² 
d = 2.79 mm	Ac=0.1987 mm ² 	Ac=0.5535 mm ² 	Ac=0.8516 mm ² 

Figure 4.16. Modified SEM images of tool-chip contact area for cutting experiments of AL-6061 at 490 m/min, different feed rates and depths of cut

Depth of cut (mm)	Zone	Feed rate (mm/rev)		
		0.071	0.198	0.305
0.51	Prim. Sticking	0.3272	0.3155	0.3161
	Sliding	0	0	0.1427
	Sec. Sticking	0	0	0
1.27	Prim. Sticking	0.6139	0.5736	0.5352
	Sliding	0	0.1860	0.3820
	Sec. Sticking	0	0	0
2.03	Prim. Sticking	0.9657	0.7607	0.8019
	Sliding	0	0.2618	0.6067
	Sec. Sticking	0	0	0
2.79	Prim. Sticking	1.2798	0.9606	0.8833
	Sliding	0	0.3397	0.9023
	Sec. Sticking	0	0	0

Table 4.6. Primary sticking, sliding and secondary sticking area values for Al-6061 at 120 m/min

Numerical values of each contact zone is given in Table 4.6 and shown in Figure 4.16. Since there is no secondary sticking zone built in this cutting condition, chemical composition of material layer deposited on the primary sticking zone is given in Figure 4.17. This data shows an aluminum content of 97%, magnesium content of 1.6% and silicon content of 0.5%, which is typical composition of Al-6061 at room temperature.

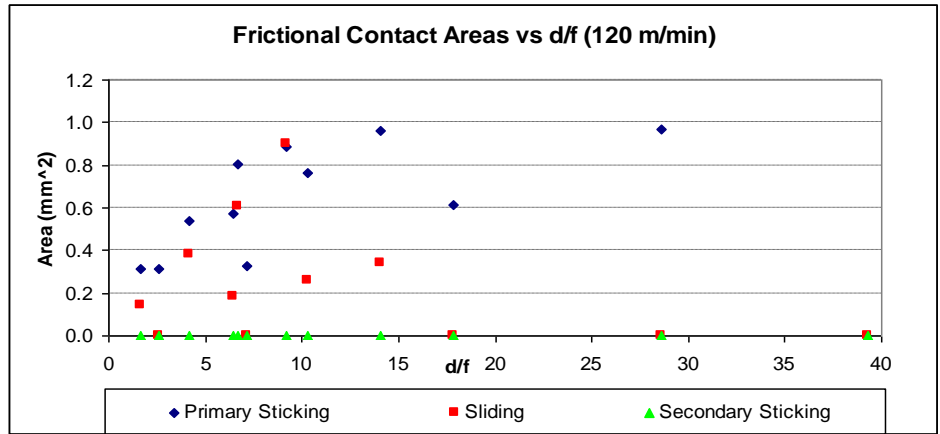


Figure 4.17. Frictional contact areas vs d/f for Al-6061 at 120 m/min

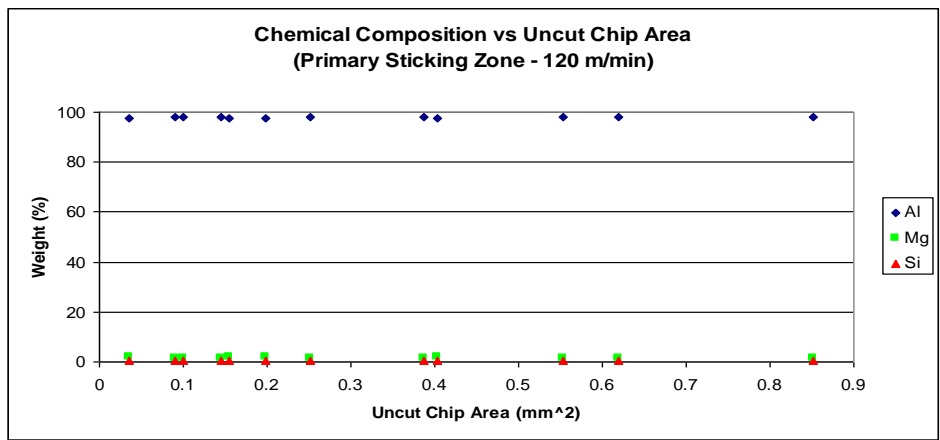


Figure 4.18. Chemical composition of primary sticking zone for Al-6061 at 120 m/min

When the cutting speed increases (230 m/min), secondary sticking area starts to develop. In spite of small depth of cut and low feed rate, there is still no secondary sticking zone observed. The built-up layer spread seen in the primary sticking zone decreases compared to low cutting speed experiment results. This

change can be identified by comparing the area of each zone as tabulated in Table 4.7 with the low cutting speed experiment. It is also shown graphically in Figure 4.19. It is concluded that 230 m/min is the transition speed from the built-up edge formation to normal frictional cutting conditions.

Depth of cut (mm)	Zone	Feed rate (mm/rev)		
		0.071	0.198	0.305
0.51	Prim. Sticking	0.1317	0.0876	0.1457
	Sliding	0	0.1330	0.1665
	Sec. Sticking	0	0	0
1.27	Prim. Sticking	0.2080	0.1782	0.3127
	Sliding	0.2115	0.3294	0.3019
	Sec. Sticking	0	0.0632	0.5748
2.03	Prim. Sticking	0.4035	0.2958	0.3693
	Sliding	0.2535	0.4973	0.4637
	Sec. Sticking	0	0.5966	0.8643
2.79	Prim. Sticking	0.5166	0.5265	0.5330
	Sliding	0.2959	0.6196	0.5861
	Sec. Sticking	0	0.7498	1.2843

Table 4.7. Primary sticking, sliding and secondary sticking area values for Al-6061 at 230 m/min

The chemical composition of material layer deposited on the primary and secondary sticking zones for 230 m/min cutting speed is given in Figure 4.19.

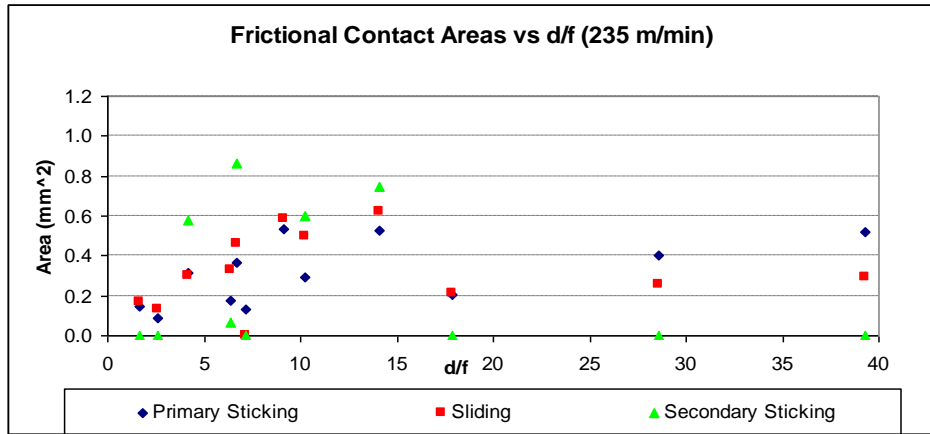


Figure 4.19. Frictional contact areas vs d/f for Al-6061 at 230 m/min

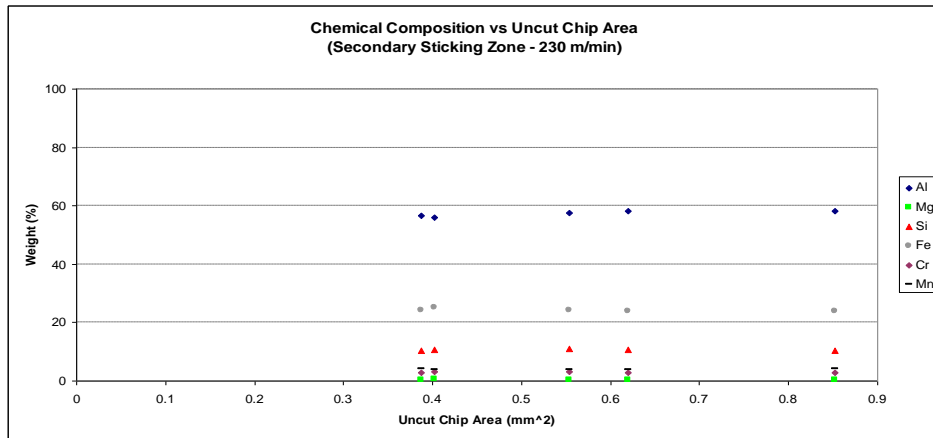
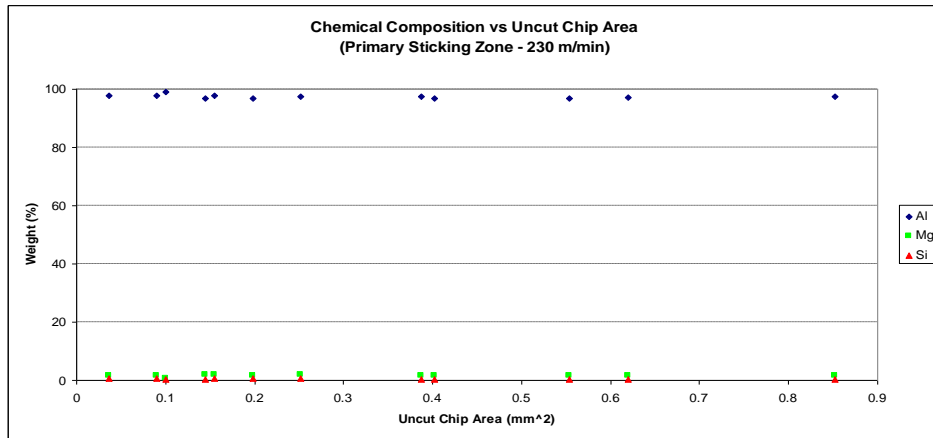


Figure 4.20. Chemical composition of primary and secondary sticking zones for Al-6061 at 230 m/min

The elemental analysis in the primary sticking zone is same as it is in the low cutting speed. The chemical composition of adhesion layer in the primary sticking zone is observed approximately as 97.5% Al, 1.6% Mg and 0.4% Si, which is typical for Al-6061 material. A considerable difference is observed in the secondary sticking zone. With increasing federate and depth of cut, the aluminum content decreases to approximately 59% and iron content increases to approximately 24%, and silicon content increases to 10%. As it was observed in Al-2024 cutting experiments, this is the effect of thermal softening with increasing speed.

With further increase in cutting speed 345 m/min, primary sticking zone decreases slightly, sliding zone moves to the front and secondary sticking zone increases, as was observed for Al-2024, too. Modified SEM images shown in Figure 4.15 illustrate this change. Area values show the difference in zone formation also. Area values at 345 m/min cutting speed are tabulated in Table 4.8 and shown in Figure 4.20.

The primary cutting zone elemental composition does not change at 345 m/min cutting experiments. This is in agreement with the experiments at cutting speeds of 120 m/min and 230 m/min. Secondary sticking zone, on the other hand exhibits a different result. Aluminum content drops to 60-65%, iron content increases to 20-25 %, and silicon remains same as 10%, and composition of other alloying elements increases. This data is shown in Figure 4.21.

Depth of cut (mm)	Zone	Feed rate (mm/rev)		
		0.071	0.198	0.325
0.51	Prim. Sticking	0.0686	0.1040	0.1461
	Sliding	0.0949	0.1319	0.1935
	Sec. Sticking	0	0.1801	0
1.27	Prim. Sticking	0.1034	0.1887	0.2498
	Sliding	0.1626	0.2615	0.3787
	Sec. Sticking	0	0.4100	0.3645
2.03	Prim. Sticking	0.2054	0.2154	0.3160
	Sliding	0.2396	0.3919	0.5426
	Sec. Sticking	0	0.5716	0.5184
2.79	Prim. Sticking	0.3367	0.3667	0.4255
	Sliding	0.2988	0.4675	0.6550
	Sec. Sticking	0	0.72478	0.8006

Table 4.8. Primary sticking, sliding and secondary sticking area values for Al-6061 at 345 m/min

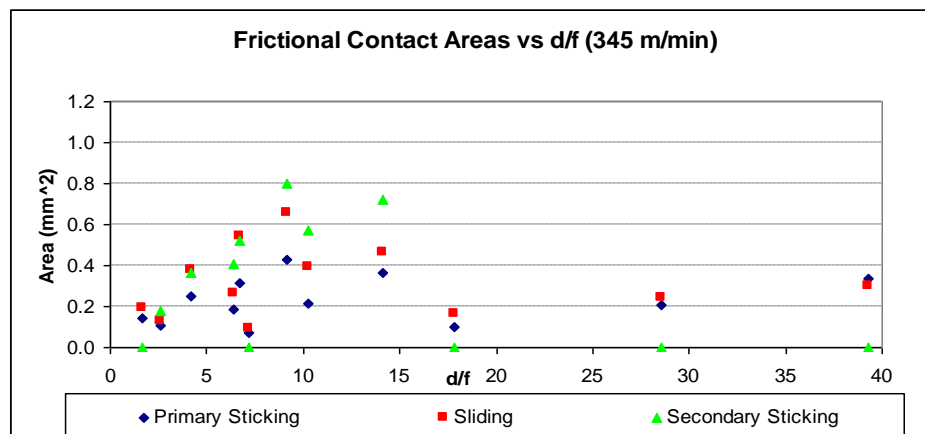


Figure 4.21. Frictional contact areas vs d/f for Al-6061 at 345 m/min

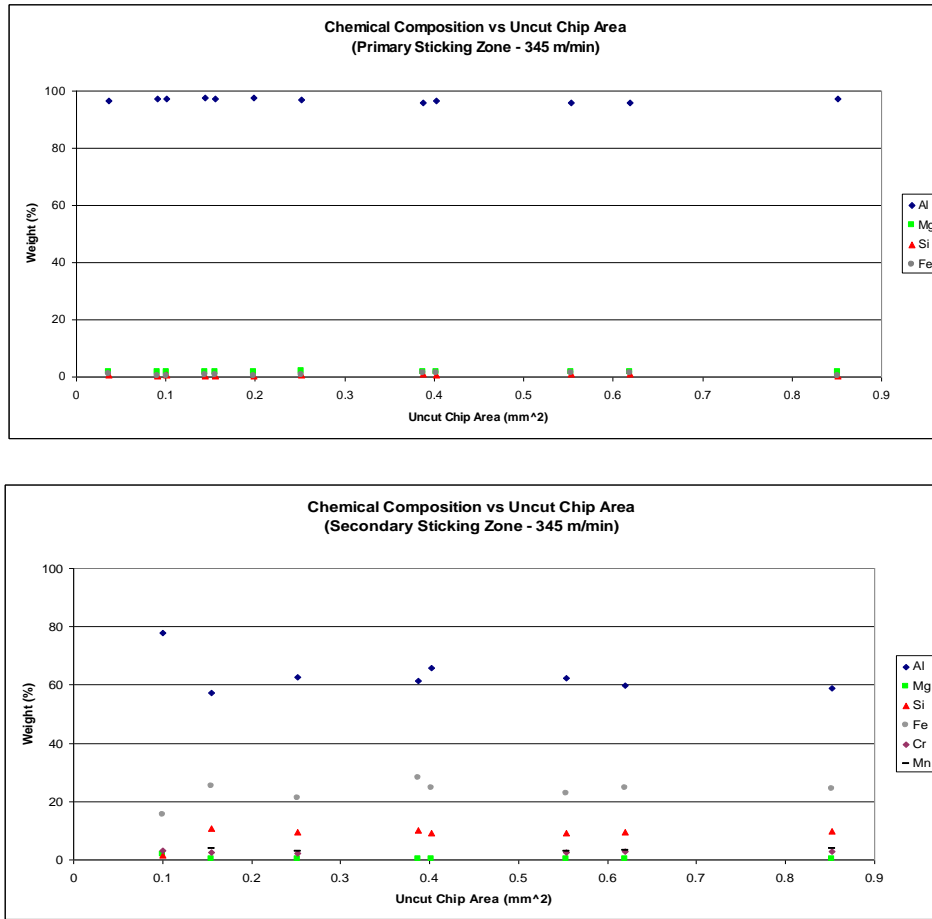


Figure 4.22. Chemical composition of primary and secondary sticking zones for Al-6061 at 345 m/min

Cutting experiments at 490 m/min show similar results as experiments at 335 m/min. The area of primary zone decreases slightly, moving the sliding zone further to the cutting edge, and the secondary sticking zone further increases. Still no secondary sticking zone is observed for low feed rates; even the cutting speed is high. The results of 490 m/min experiments are tabulated in Table 4.9 and shown in Figure 4.22. The primary sticking zone chemical composition does not

change and is in agreement with the composition found in lower cutting speed experiments. For the secondary sticking zone, aluminum content is 97% for the low feed rate and decreases to 60% at higher feed rate. Iron content is 25%, and silicon is 10%, with other alloying elements remaining the same as 335 m/min cutting experiments results. Although a secondary sticking zone is observed for low feed rates, the chemical composition on this area shows that this layer behaves like a built-up edge formation for low feed rates. Figure 4.23 shows the chemical composition change of sticking zones at the highest cutting speed.

Depth of cut (mm)	Zone	Feed rate (mm/rev)		
		0.071	0.198	0.325
0.51	Prim. Sticking	0.0702	0.1038	0.1153
	Sliding	0.1573	0.1100	0.1219
	Sec. Sticking	0	0.1725	0.2125
1.27	Prim. Sticking	0.1331	0.1464	0.1585
	Sliding	0.3193	0.2273	0.2395
	Sec. Sticking	0	0.3849	0.5137
2.03	Prim. Sticking	0.1968	0.2510	0.1928
	Sliding	0.4400	0.3044	0.3683
	Sec. Sticking	0	0.5314	0.8744
2.79	Prim. Sticking	0.2588	0.2441	0.1809
	Sliding	0.4735	0.4505	0.5089
	Sec. Sticking	0	0.8626	1.1270

Table 4.9. Primary sticking, sliding and secondary sticking area values for Al-

6061 at 490 m/min

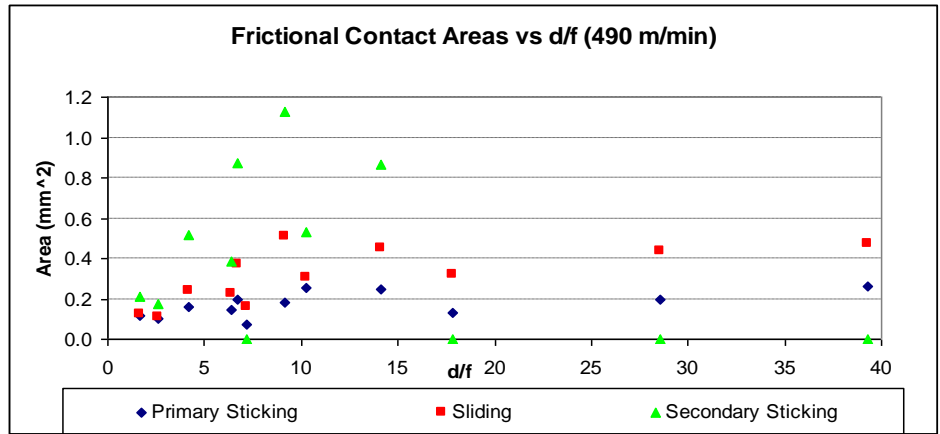


Figure 4.23. Frictional contact areas vs f/d for Al-6061 at 490 m/min

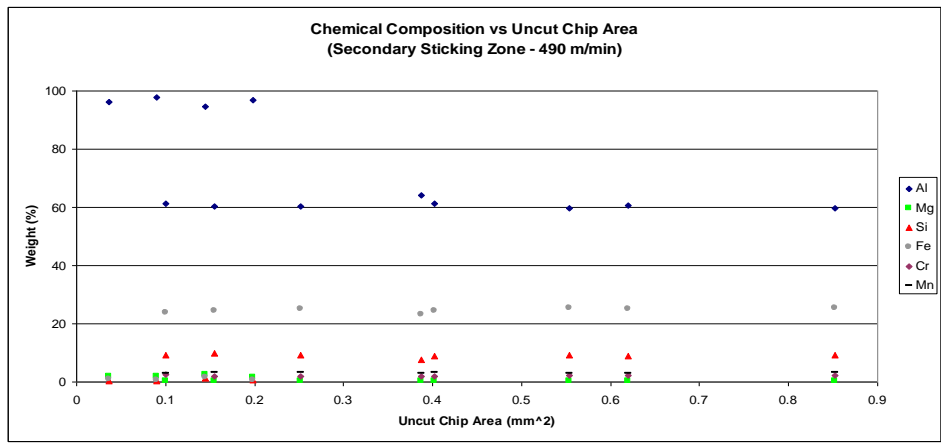
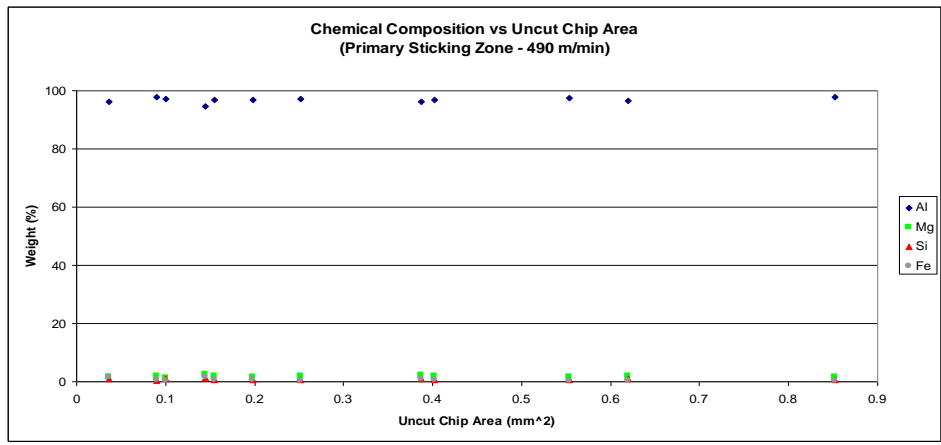


Figure 4.24. Chemical composition of primary and secondary sticking zones for Al-6061 at 490 m/min

Al-6061 generally has an excess of Mg_2Si as a phase constituent. After passing the primary shear zone and primary sticking zone, precipitates of Mg_2Si are observed in the secondary sticking as the chip cools slowly. Also, iron-rich phases such as $Fe_3Si_2Al_{12}$ are observed giving rise to iron and silicon content on the secondary sticking zone.

No secondary sticking zone formation at low cutting speeds is the main difference of Al-6061 material from Al-2024. Also, at high cutting speeds and low feed rates, there is no secondary sticking zone in Al-6061. Built-up edge formation at low cutting speeds is more problematic when machining Al-6061. Al-6061 is rather soft and gummy, and it has a tendency to stick to the cutting tool when machining. This is what was observed from the SEM images of deposited layers on the cutting tool surface. Al-6061 is more prone to built-up edge formation and exhibits better sticking characteristics to the surface of cutting tool. Although both Al-2024 and Al-6061 are classified as free-machining aluminum alloys, Al-2024 has better machinability rating than Al-6061.

Cutting Force Data Analysis

Experiments were carried out on an industry type lathe, shown in Figure 3.1. During each experiment, cutting forces were measured continuously by a

Kistler type piezoelectric dynamometer. The working principles of the piezoelectric type force transducers were explained in Chapter 3.

Cutting forces acting on the dynamometer are recorded in three mutually perpendicular axes as shown in Figure 4.25.

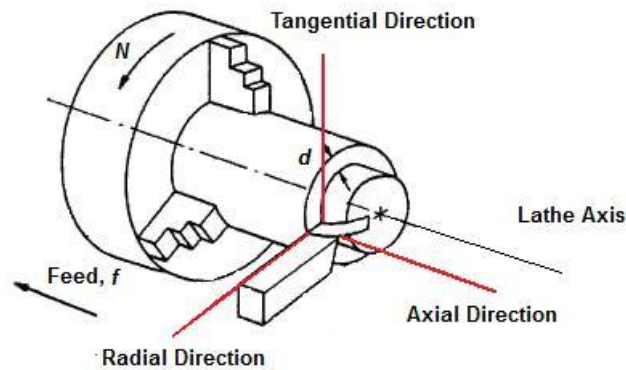


Figure 4.25. Schematic of cutting force axes

Forces acting on the tool are named based on the axes along which they act. These forces are described as follows:

- F_x is the component of cutting force measured along the axial direction, which is parallel to the Lathe axis, and opposite to the feed direction
- F_y is the component of cutting force measured along the radial direction, which is perpendicular to the axial direction and acts radially outward

- F_z is the component of cutting force measured in tangential direction, which is perpendicular to both axial and radial directions, and acts opposite to the rotation of workpiece.

Due to the nose radius, the chip flow angle was calculated as described in [3]. To make the definition easier, the chip flow angle can be redefined with respect to the straight cutting edge of the tool. As a result of this definition and calculations, the chip flow angle (with respect to the straight cutting edge of the tool) was found to be 37.5° . With the help of SEM pictures, the chip flow direction was manually measured with a protractor. The measurements were taken on several cutting experiments with the same cutting conditions. The results of these measurements yielded the chip flow direction as 35° , which is very close to the theoretical prediction.

This result shows that equivalent cutting edge model predicts the variables of actual cutting tool accurately. With the same approach the cutting forces can be redefined on the equivalent cutting edge.

Assumptions:

- Although the tool tip is sharp, plowing forces act on the tool tip
- The resultant force acting on the chip at the shear plane is equal, opposite and collinear to the force acting on the chip at the rake face.

After the equivalent edge assumption and the geometry of cutting edge are defined, the forces measured by the force dynamometer can be transformed to the new axes which are perpendicular to the rake face and tangential to the modified

side cutting edge and end cutting edge on the rake face. The schematic representation of this transformation is given in Figure 4.26. The transformation of measured forces to the forces acting normal and tangential to the cutting tool can be explained in three steps:

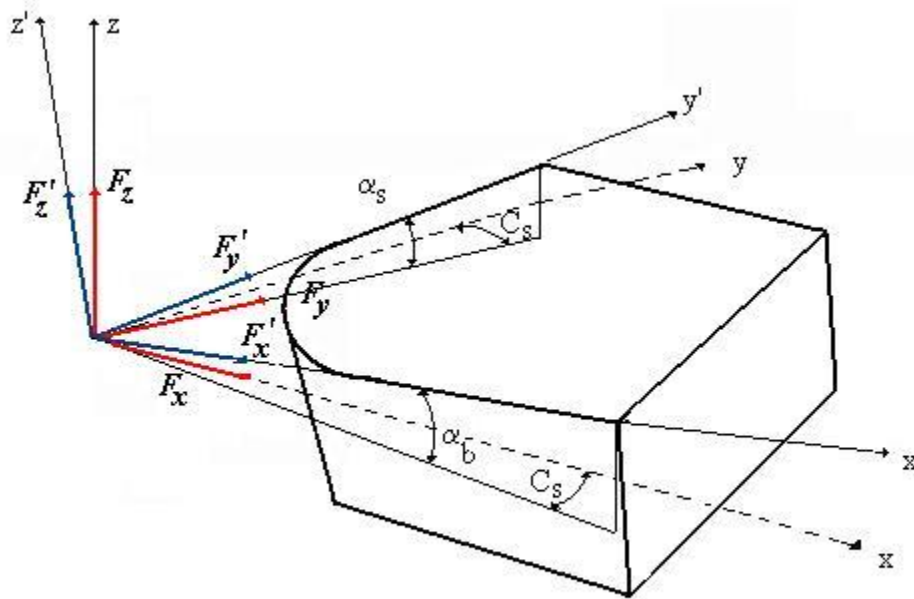


Figure 4.26. Schematic showing force measurement axis, forces acting on the tool, and tool geometry

First Step: When looking from the cutting direction, i.e., z -direction, the forces and the tool geometry can be seen as shown in Figure 4.27. Here F_x and F_y are the measured forces and F_A' and F_R' are the forces acting along the plan view of side cutting edge and end cutting edge of the modified tool. The modified side cutting edge angle is labeled as C_s^* in the figure.

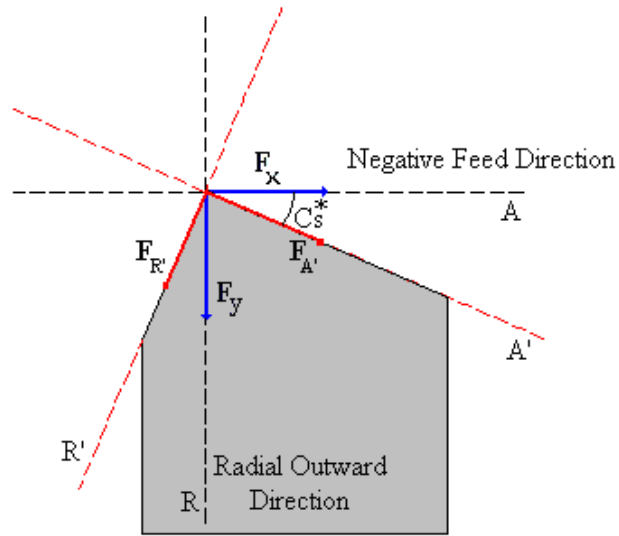


Figure 4.27. Planar view of the cutting tool (xy plane)

Mathematical model for the first transformation is:

$$\begin{aligned}
 F_C &= F_Z \\
 F_{A'} &= F_x \cdot \cos C_S^* + F_y \cdot \sin C_S^* \\
 F_{R'} &= F_y \cdot \cos C_S^* - F_x \cdot \sin C_S^*
 \end{aligned} \tag{9}$$

Second Step: When looking from modified axial direction (A'), the tool and forces can be seen as shown in Figure 4.28. F_Z is the cutting force acting in C direction, which is not perpendicular to the tool rake face. Because of the inclination angle of the cutting tool, $F_{R'}$ is not acting on the rake face. This second transformation will result in forces F_C' and $F_{R''}$, which act perpendicular to the rake face and tangential to the rake face along the side cutting edge (R'' direction), respectively.

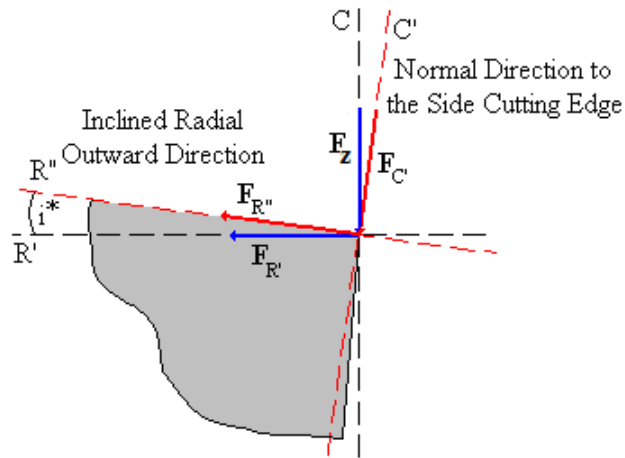


Figure 4.28. Planar view of cutting tool when projected in the modified axial direction

Mathematical model for the second transformation is:

$$\begin{aligned}
 F_A' &= F_A' \\
 F_C' &= F_Z' \cdot \cos i^* + F_{R'}' \cdot \sin i^* \\
 F_R'' &= F_{R'}' \cdot \cos i^* - F_Z' \cdot \sin i^*
 \end{aligned} \tag{10}$$

Third step: When looking in the direction of modified radial direction (R''), the tool and forces can be seen as shown in Figure 4.29. F_C' and F_A' are the two forces on the rake face. They need to be resolved as normal and tangential force components on the rake face. A modified rake face angle is the key element in this transformation, which will result in F_C'' and F_A'' . F_C'' is the force acting perpendicular to rake face, and F_A'' is the force acting tangentially on the rake face along the modified axial direction (A'').

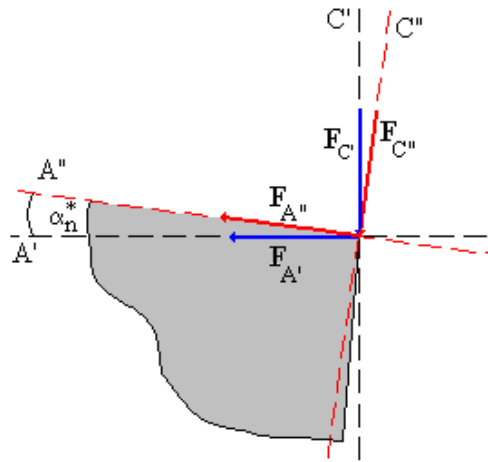


Figure 4.29. Planar view of cutting tool when projected in the modified radial direction

Mathematical model for the third transformation is:

$$\begin{aligned}
 F_R'' &= F_R'' \\
 F_C'' &= F_C' \cdot \cos \alpha_n^* + F_A' \cdot \sin \alpha_n^* \\
 F_A'' &= F_A' \cdot \cos \alpha_n^* - F_C' \cdot \sin \alpha_n^*
 \end{aligned} \tag{11}$$

The forces on the rake face are dependent on the geometry of the tool and are shown in Figure 4.30 after transformation. These forces create the normal compressive stress and shear stress on the rake face. There are two forces responsible for the frictional force on the tool rake face, namely F_A'' and F_R'' . As seen from the figure, their resultant force will be the frictional force, which has to be in the same direction as the chip flow. The angle β can be defined as the ratio of the F_R'' to F_A'' . It is measured from the end cutting edge of the cutting tool.

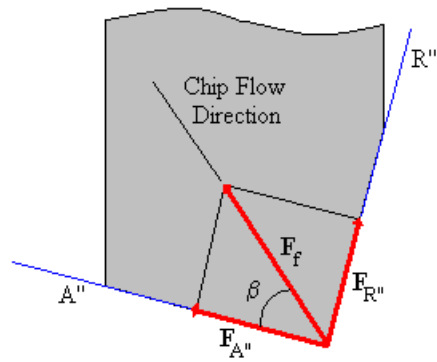


Figure 4.30. Frictional force on the rake face

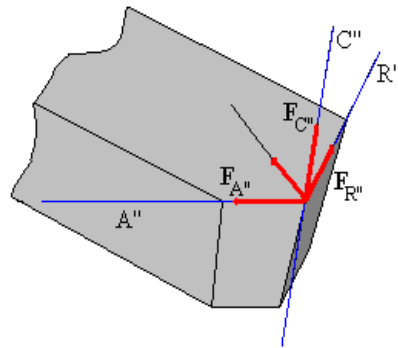


Figure 4.31. 3-D schematic representation of equivalent cutting tool with actual cutting forces

The cutting forces measured during experiments were transferred to the normal and shear components on the tool rake face.

$$\begin{aligned}
 F_s &= \sqrt{(F_A'')^2 + (F_R'')^2} \\
 F_n &= F_C''
 \end{aligned}
 \tag{12}$$

Al-2024	110 m/min (400 rpm)		225 m/min (558 rpm)		335 m/min (765 rpm)		470 m/min (1350 rpm)	
	F_n (N)	F_f (N)	F_n (N)	F_f (N)	F_n (N)	F_f (N)	F_n (N)	F_f (N)
1.667	168	142	159	106	133	84	136	75
2.564	122	108	116	83	114	77	105	59
4.167	401	298	335	194	352	175	318	157
6.410	282	233	246	159	250	139	264	137
6.667	619	447	567	319	568	276	493	238
7.143	57	67	51	48	52	45	45	38
9.167	848	613	749	405	706	343	660	317
10.256	438	363	414	266	412	224	384	198
14.103	590	507	545	348	524	292	504	271
17.857	131	142	112	101	109	85	114	86
28.571	202	221	189	172	180	140	168	124
39.286	274	295	250	226	231	181	220	169

Table 4.10. Normal and frictional forces on the cutting tool for Al-2024 at different cutting speeds, feed rate and depth of cut

Normal force (F_n) is the force responsible for the main contributor to the cutting process and frictional force (F_f) is the frictional force between the chip and tool surface. Experimentally measured cutting forces (F_x , F_y , F_z), transformed cutting forces on the tool (F_r , F_t , F_a) and the normal and shear force on the tool

(F_n , F_f) are tabulated in Appendix B for Al-2024 and Al-6061. The measured forces are recorded in US customary unit system as poundforce (lb-f) and converted to SI Unit system as Newton (N). Tables 4.10 and 4.11 summarizes the numerical values of the normal and frictional forces on the cutting tool for Al-2024 and Al-6061 experiments, respectively

Al-6061	120 m/min (400 rpm)		230 m/min (558 rpm)		345 m/min (765 rpm)		490 m/min (1350 rpm)	
	F_n (N)	F_f (N)	F_n (N)	F_f (N)	F_n (N)	F_f (N)	F_n (N)	F_f (N)
1.667	220	148	196	119	176	89	161	71
2.564	155	106	142	92	129	76	114	58
4.167	482	281	412	196	361	143	339	114
6.410	347	221	301	172	267	135	251	102
6.667	696	402	604	280	554	217	525	176
7.143	68	50	66	47	64	46	57	39
9.167	972	568	837	390	756	287	740	257
10.256	511	327	449	255	408	202	389	157
14.103	732	468	619	347	546	266	521	218
17.857	158	110	143	100	130	91	125	81
28.571	237	165	222	161	202	142	194	125
39.286	335	236	294	210	279	196	258	169

Table 4.11. Normal and frictional forces on the cutting tool for Al-6061 at different cutting speeds, feed rate and depth of cut

Furthermore the cutting force vs (d/f) is graphed and some interesting conclusions are drawn. (d/f) value is a dimensionless quantity and represents the experimental control variables well.

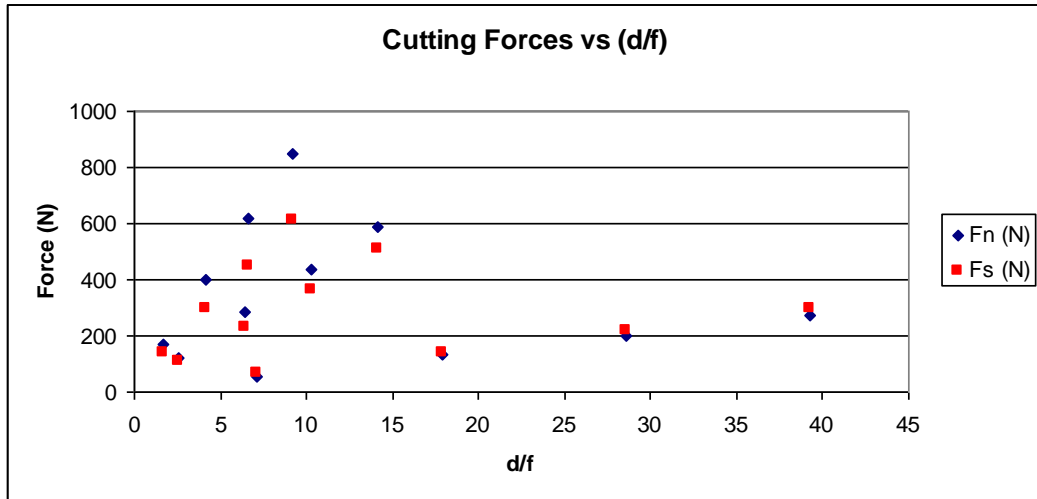


Figure 4.32. Normal and frictional force vs d/f for Al-2024 at 110 m/min

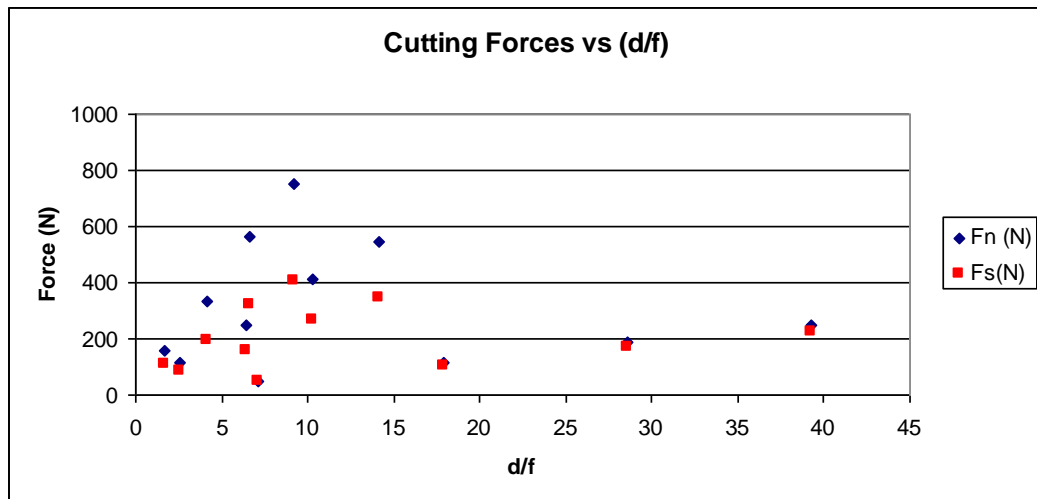


Figure 4.33. Normal and frictional force vs d/f for Al-2024 at 225 m/min

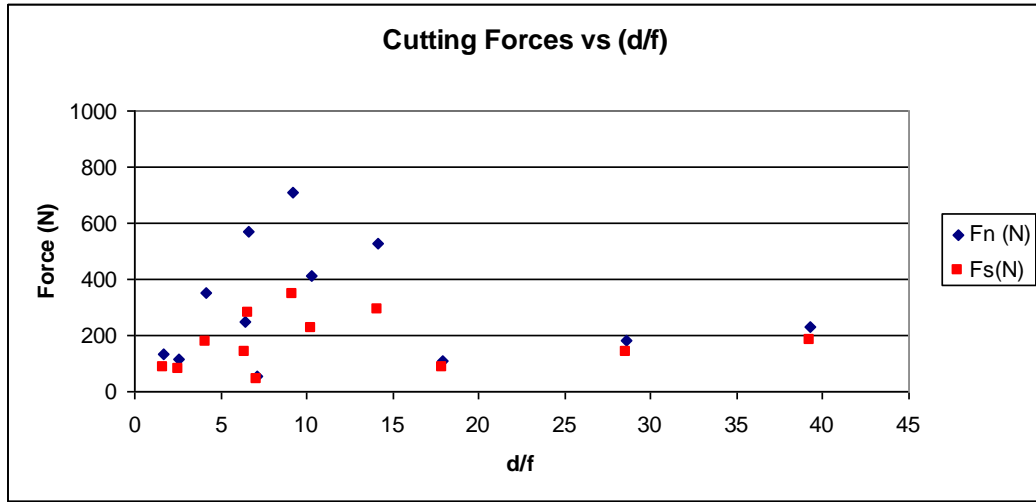


Figure 4.34. Normal and frictional force vs d/f for Al-2024 at 335 m/min

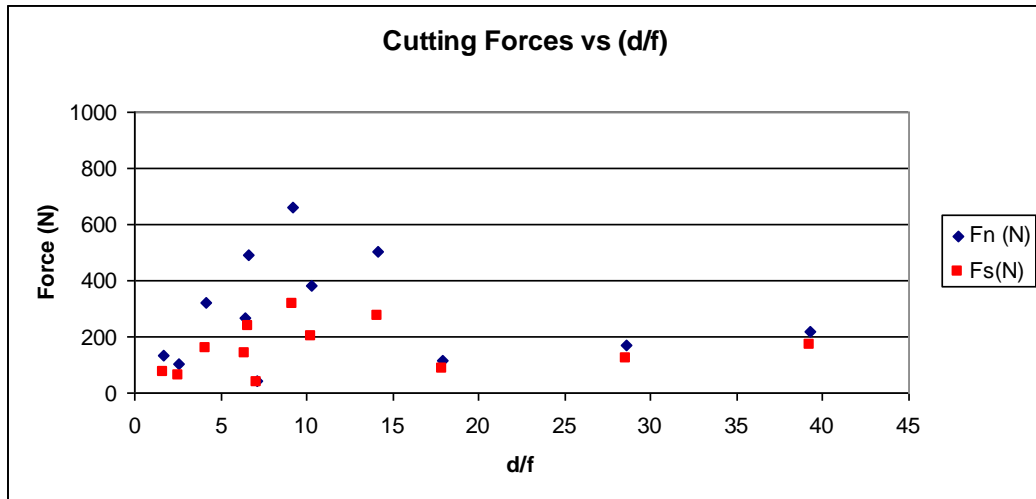


Figure 4.35. Normal and frictional force vs d/f for Al-2024 at 470 m/min

After careful investigation of these graphs following conclusions were made:

- As the cutting speed increases, the cutting forces decrease
- Effect of feed rate is more dominant than that of depth of cut

- For the same feed rate, cutting forces increase linearly with depth of cut
- For low feed rate, normal and frictional force values are almost equal to each other. Normal force is larger than frictional force for higher feed rate values irrespective of depth of cut

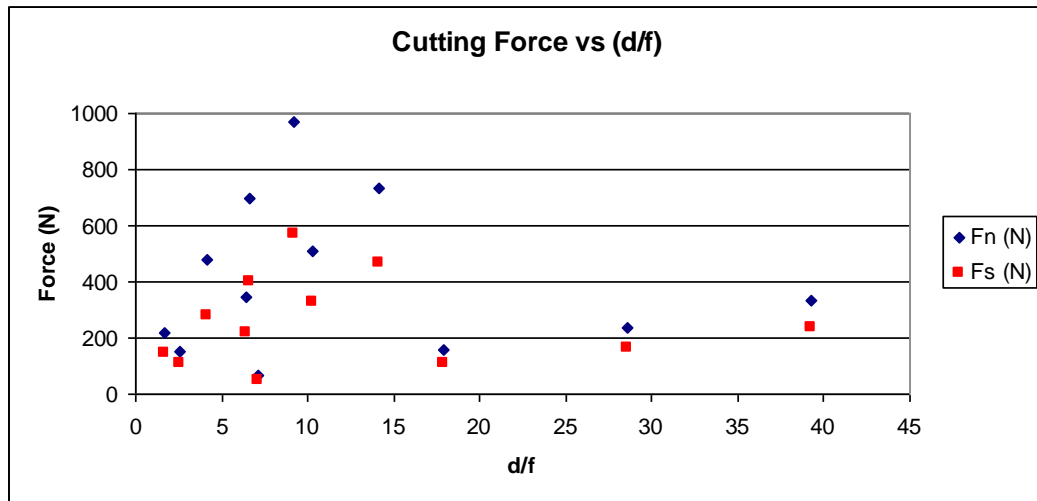


Figure 4.36. Normal and frictional force vs d/f for Al-6061 at 120 m/min

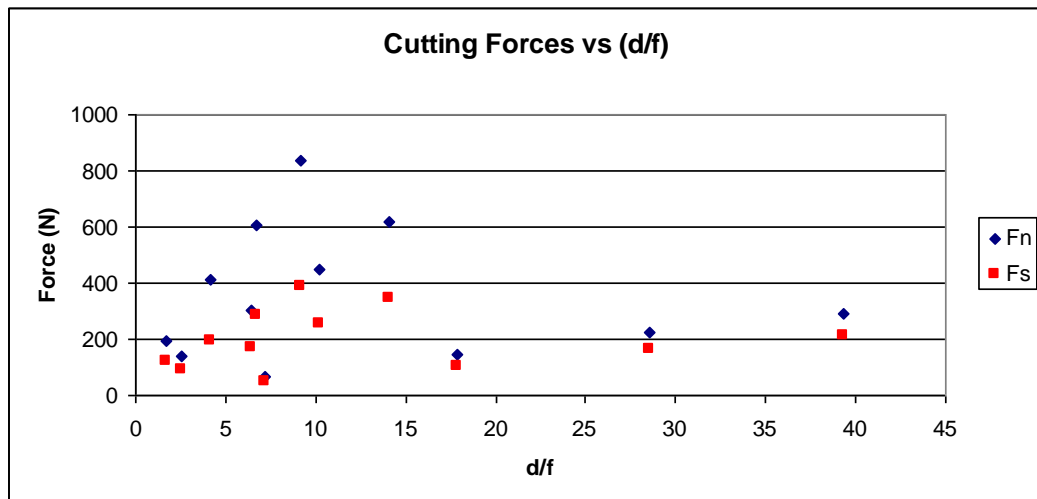


Figure 4.37. Normal and frictional force vs d/f for Al-6061 at 230 m/min

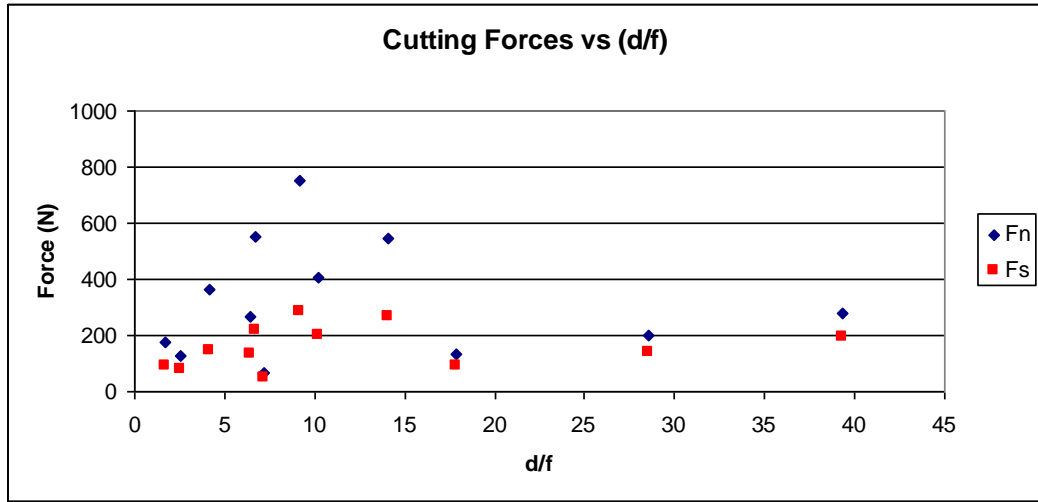


Figure 4.38. Normal and frictional force vs d/f for Al-6061 at 345 m/min

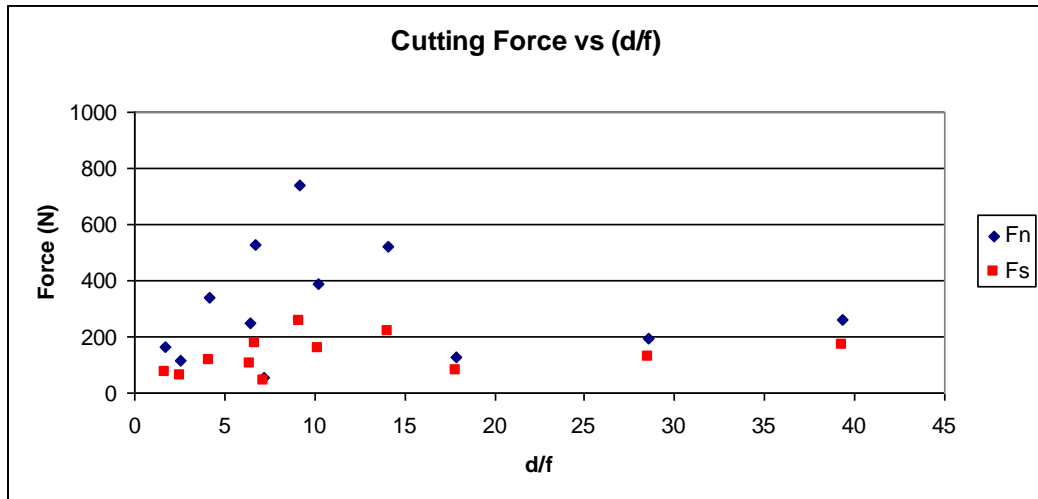


Figure 4.39. Normal and frictional force vs d/f for Al-6061 at 490 m/min

The same observations are valid for Al-6061 workpiece material. However, we can make some conclusions between two materials by comparing the corresponding graphs for the same cutting speeds. Cutting speeds show a slight difference between Al-2024 and Al-6061. However, this difference is

negligible and cannot be accounted for the force measurement differences between these two materials.

- Normal force measurements are larger for Al-6061 compared to Al-2024 for all cutting speeds and feed rates
- Opposite is true for shear force measurements: Al-2024 show higher frictional forces than Al-6061.

Plowing Force Determination

The shape of uncut chip cross section is not rectangular when machining with a finite tool radius. One important aspect of this tool geometry is the plowing force. As the tool edge engages into the workpiece material, the force acting on the tool cutting edge forms a portion of the cutting force. This force acts on the tool edge and cannot be neglected. This is the normal plowing force, F_{pn} .

Due to high stresses acting very near to cutting edge, deformation of the tool material may occur in this region. This deformation will cause contact between tool and new workpiece surface over a small area of the tool flank. Cutting with sharp edge tools, a frictional force component might occur due to this action. This force is called frictional plowing force, F_{pf} . Plowing forces acting on the tool edge is shown in Figure 4.40.

However, the force acting on the tool edge and the force on the tool flank do not contribute to chip removal, and these forces are called the plowing forces.

Existence of plowing forces in our cutting experiments can be determined by extrapolation of the cutting force data. This approach relies on the nonexistence of cutting forces if the uncut chip area becomes zero. In other words, there will not be any forces if the tool is not engaged with the workpiece. Cutting force versus d/f graphs show that the forces are proportional with depth of cut, and as the depth of cut approaches to zero, cutting forces are not zero.

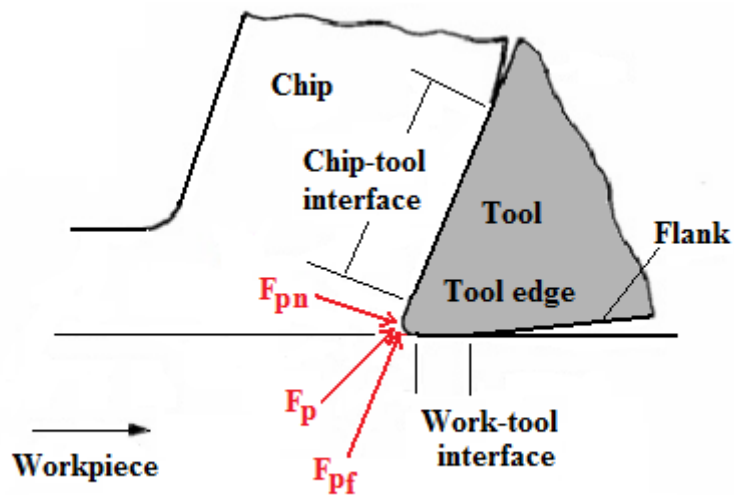


Figure 4.40. Plowing force and contact regions on a cutting tool

The finite value of these forces can be found by extrapolation of experimental relationship between the cutting force data and depth of cut or d/f . The existence and determination of plowing forces can be seen in Figure 4.41 as an example, for Al-2024 at 470 m/min. Normal and frictional forces on the cutting tool were graphed for low feed rate (0.071 mm/rev) and for four depths of cut. A line is fitted to the data points. The intercept of the fitted line with zero

depth of cut gives the so called “plowing force” for both normal and frictional forces. Plowing forces obtained by linear curve fitting method is shown in Tables 4.12 and 4.13 for Al-2024 and Al-6061, respectively.

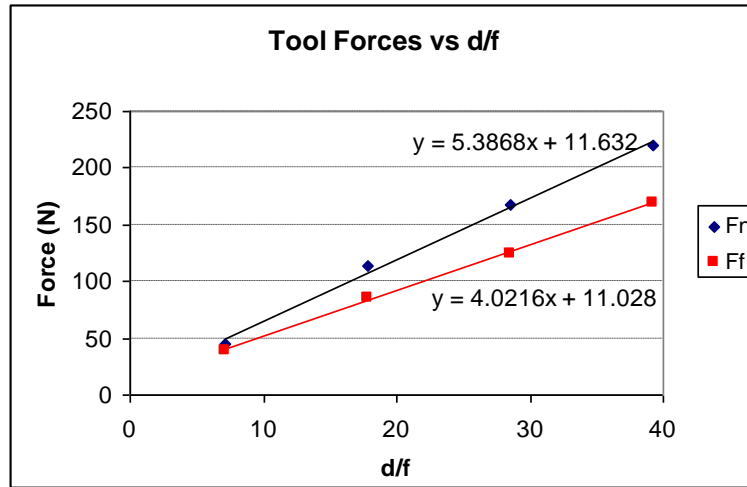


Figure 4.41. Graphical determination of plowing force for Al-2024 at 470 m/min and low feed rate

Cutting Speed (m/min)	Plowing Forces	f=0.071	f=0.198	f=0.305
		mm/rev	mm/rev	mm/rev
110	F_{pn}	15.50	19.84	19.54
	F_{pf}	9.90	15.46	36.49
225	F_{pn}	4.52	14.89	18.56
	F_{pf}	5.86	18.12	34.95
335	F_{pn}	10.61	23.19	20.63
	F_{pf}	12.07	25.02	29.43
470	F_{pn}	11.63	28.60	23.60
	F_{pf}	11.03	15.04	21.59

Table 4.12. Plowing forces for Al-2024

Cutting Speed (m/min)	Plowing Forces	f=0.071 mm/rev	f=0.198 mm/rev	f=0.305 mm/rev
120	F_{pn}	9.03	25.46	57.03
	F_{pf}	7.40	22.77	50.26
230	F_{pn}	16.37	35.41	53.54
	F_{pf}	10.32	33.12	51.60
345	F_{pn}	13.42	35.73	43.94
	F_{pf}	10.24	31.70	39.28
490	F_{pn}	12.69	24.37	25.05
	F_{pf}	9.93	17.81	20.28

Table 4.13 Plowing forces for Al-6061

The plowing forces were subtracted from the measurement data to find the main contributing components of cutting forces.

$$\begin{aligned}
 F_n &= (F_n)' - F_{pn} \\
 F_f &= (F_f)' - F_{pf}
 \end{aligned}
 \tag{13}$$

Tables 4.14. and 4.15 show the forces contributing only to the cutting and material removal after the plowing effect is subtracted. These forces will be compared with the forces obtained by the stress model.

Al-2024	110 m/min (400 rpm)		225 m/min (558 rpm)		335 m/min (765 rpm)		470 m/min (1350 rpm)	
	F_n (N)	F_f (N)	F_n (N)	F_f (N)	F_n (N)	F_f (N)	F_n (N)	F_f (N)
1.667	148	106	141	71	112	54	112	53
2.564	102	93	101	65	91	52	76	44
4.167	381	262	316	159	331	146	295	135
6.410	262	218	231	141	227	114	235	122
6.667	599	410	548	284	547	247	470	217
7.143	42	57	46	43	41	33	33	27
9.167	828	577	731	370	686	313	636	295
10.256	419	347	399	248	389	199	355	183
14.103	570	491	530	330	501	267	476	256
17.857	116	132	108	95	98	73	103	75
28.571	186	211	184	166	169	128	156	113
39.286	259	285	246	221	221	169	208	158

Table 4.14. Normal and frictional forces on the cutting tool for Al-2024 at different cutting speeds, feed rate and depth of cut - after plowing force effect is removed

Al-6061	120 m/min (400 rpm)		230 m/min (558 rpm)		345 m/min (765 rpm)		490 m/min (1350 rpm)	
	F_n (N)	F_f (N)	F_n (N)	F_f (N)	F_n (N)	F_f (N)	F_n (N)	F_f (N)
1.667	163	97	142	67	132	50	136	51
2.564	129	84	106	59	93	44	90	40
4.167	425	231	358	144	317	104	314	94
6.410	322	198	266	139	231	104	227	84
6.667	639	352	551	231	511	177	500	156
7.143	59	43	50	36	50	36	44	29
9.167	915	518	783	339	710	248	715	237
10.256	486	304	414	222	372	170	365	139
14.103	706	445	584	314	510	235	497	200
17.857	149	103	127	90	117	81	112	71
28.571	228	158	206	150	189	131	181	115
39.286	326	229	277	199	266	186	245	159

Table 4.15. Normal and frictional forces on the cutting tool for Al-6061 at different cutting speeds, feed rate and depth of cut - after plowing force effect is removed

CHAPTER 5

MATHEMATICAL MODEL OF TOOL STRESSES

There is no evidence on 3-D stress distribution profile in oblique cutting in the literature. Stress distribution on the rake face is modeled based on the different frictional conditions whose theoretical basis was proven by the experiments. Such a stress distribution model can be seen in Figure 5.1. This stress model relies on the experimental evidence of [10,17]. According to this model, the average stress values on the rake face can be determined by simple averaging method. The constant average values can be found by integrating the stress distribution profile over predefined zones and normalizing this value to the corresponding area. The validation of this model can be done by comparing the theoretically computed forces from the stress model with the measured and normalized forces obtained by experiments.

Stress Model

Without experimentation, it is very difficult to determine the normal and shear stress distribution over the rake face. In the literature, there is no proven method or model that satisfies the frictional boundary conditions and resembles to the exact stress distribution. However, some of the results obtained in the literature give good hints about possible stress distribution. These results were

presented in Chapter 2. Although the stress distributions show differences with respect to tool-workpiece material combination, cutting tool geometry, and cutting variables, the model developed by Lee et al. [51] is a satisfactory model. In this study stress state on the tool surface is assumed to behave as shown in Figure 5.1.

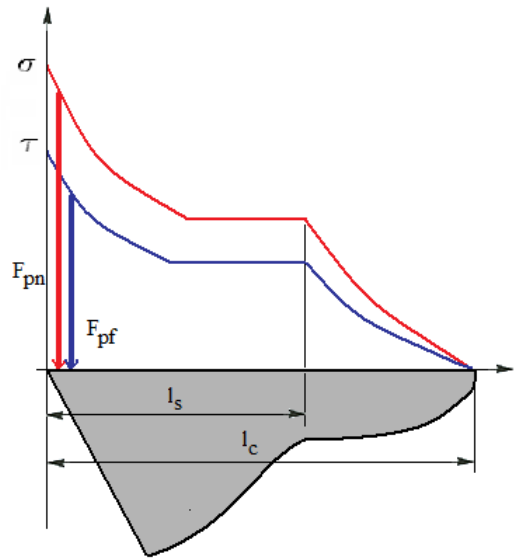


Figure 5.1. Lee's model for normal and shear stresses [51]

In this model, there is a leveling of the frictional stress, but the leveling does not extend all the way to the tool edge. Instead, the shear stress rises towards the tool edge, the extent being varying under different conditions. The normal stress is also assumed to exhibit a flattening level at some point of the curve. In this model, the high value of normal stress at the cutting edge was attributed to the plowing force. Therefore, by eliminating the plowing force on the cutting edge the

stress distribution on the tool levels flat. The method of finding the plowing force is explained in Chapter 4.

Based on the literature review on stress distributions, and tool-chip contact zone observations the following model has been proposed.

In the near part of cutting edge, sticking is the main frictional interaction between tool and chip under high cutting forces and temperatures. Most of the time, built-up edge occurs in this zone and cheeses as the cutting speed, feed rate, and depth of cut increases. This is called the primary sticking zone. It is followed by the sliding zone, where the chip freely flows over the rake face without any sticking or shearing. The secondary sticking zone depends on the cutting variables such as cutting speed, cutting time, feed rate and geometry of the cutting tool. In those regions, the stress distribution is assumed to act like Lee et al. [51] proposed.

The forces acting on the tool rake face are the shearing force on the sticking areas, $F_{S_{st}}$, frictional force on the sliding areas, $F_{S_{sl}}$, and the normal force on the total contact area, F_n . These theoretical forces can be mathematically modeled from stress-area relationship:

$$\begin{aligned}
 F_{S_{st}} &= \int_{A_{st}} \tau_{ave} \cdot dA_{st} \\
 F_{S_{sl}} &= \int_{A_{sl}} \mu \cdot \sigma_{ave} \cdot dA_{sl} \\
 F_n &= \int_{A_t} \sigma_{ave} \cdot dA_T
 \end{aligned} \tag{14}$$

$$F_{S_{theoretical}} = F_{S_{st}} + F_{S_{sl}} \quad (15)$$

$$F_{n_{theoretical}} = F_n$$

where τ_{ave} is the average shear yield strength of the chip material, μ is the average (sliding) friction coefficient between chip and tool on the sliding zone, and σ_{ave} is the average compressive stress on the different proposed contact zones. The constant average values can be found by integrating the stress distribution profile over predefined zones and normalizing this value to the corresponding area. The validation of this model can be done by comparing the theoretically computed forces with the measured forces obtained by the force transformation.

Depending on the actual contact zone, the model will predict the normal and tangential force on the tool surface. If the plowing forces associated from the edge effect are removed, the stress state on the tool surface will be further simplified as shown in Figure 5.2.

For the computation of forces from the stress model, the following assumptions are made:

- Flow stress of the material is constant. For Al-2024 it is 374 MPa and for Al-6061 it is 300 MPa. These values are the material properties listed in the material certification of test materials.
- Friction between tool and chip is taken as 0.7, as was stated 0.4-0.8 for dry cutting of aluminum alloys with tungsten carbide cutting tool.

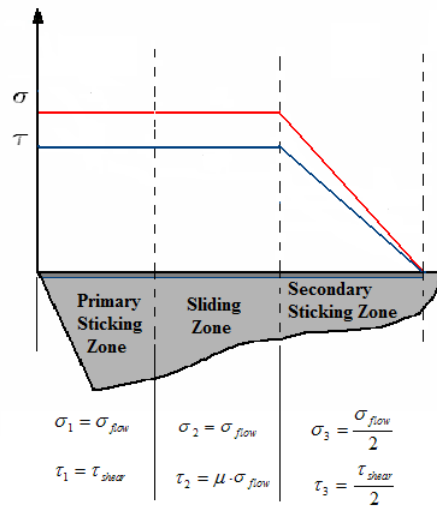


Figure 5.2. Schematic of stress model

Theoretical shear and normal forces on the cutting tool were determined from equation 19. Figures 5.3 - 5.6 compare theoretical frictional forces obtained from the stress model and experimental frictional forces for Al-2024.

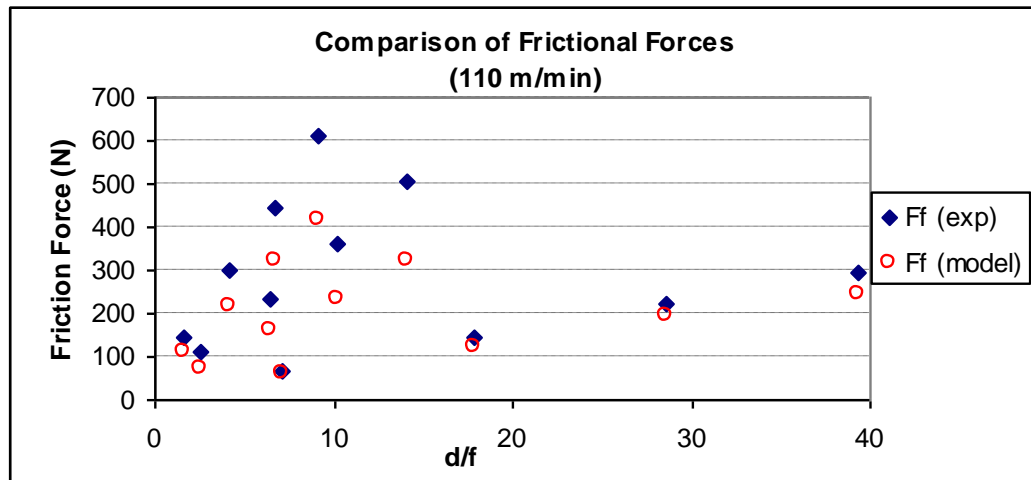


Figure 5.3. Comparison of predicted and experimental frictional forces for Al-2024 at 110 m/min

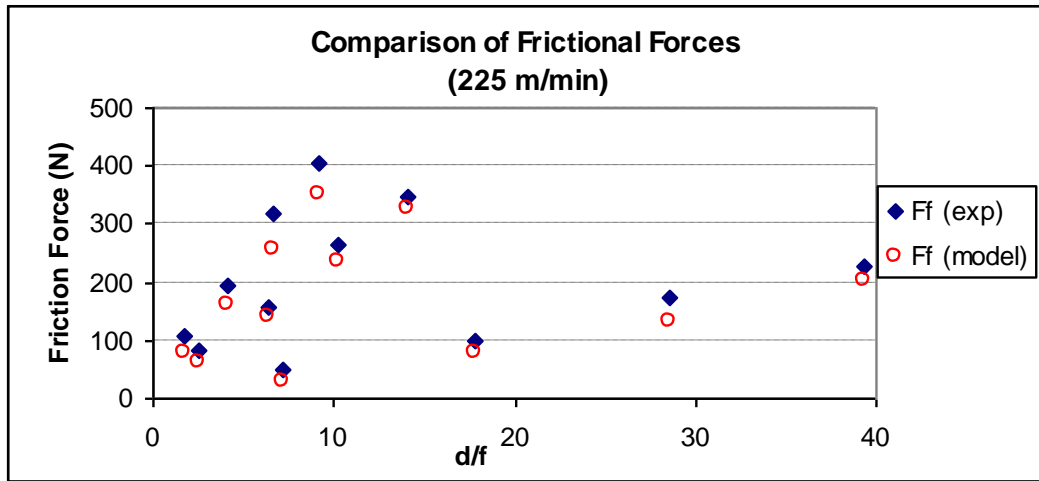


Figure 5.4. Comparison of predicted and experimental frictional forces for Al-2024 at 225 m/min

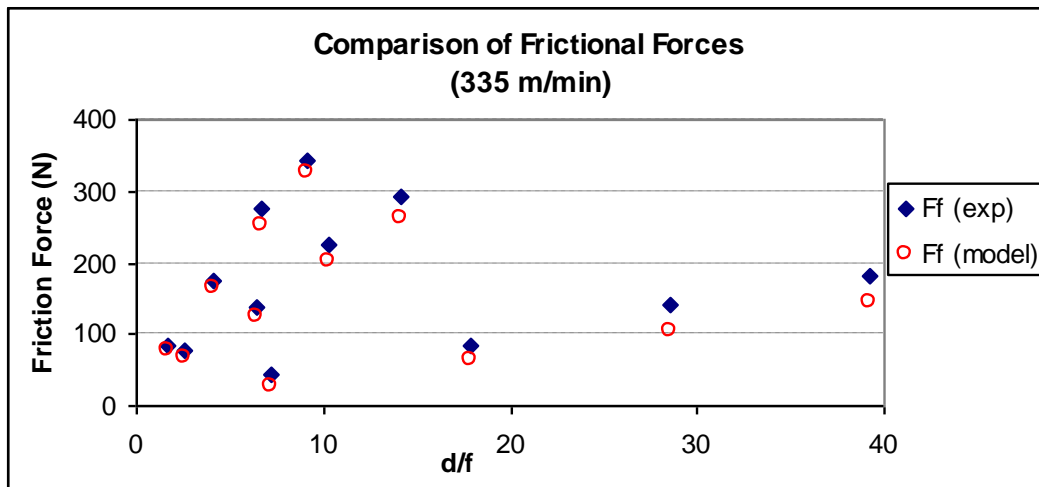


Figure 5.5. Comparison of predicted and experimental frictional forces for Al-2024 at 335 m/min

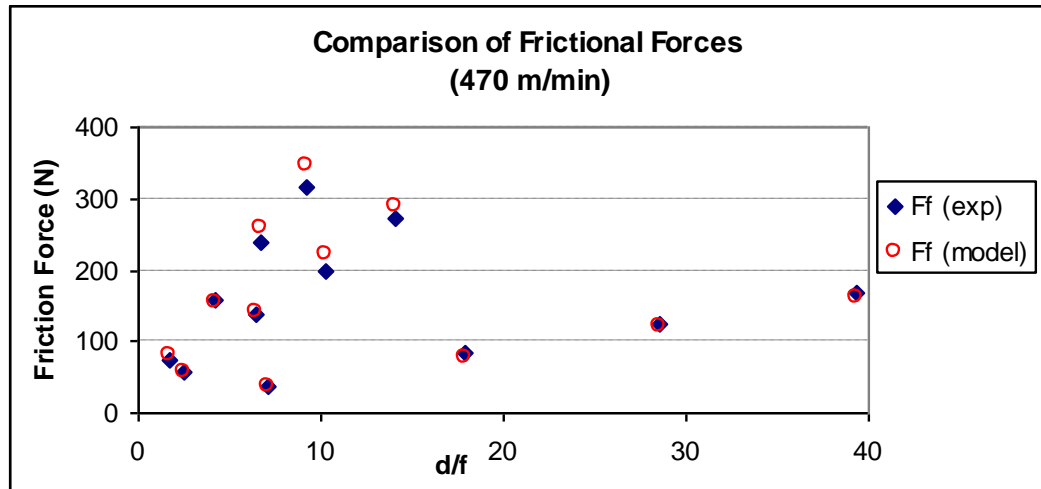


Figure 5.6. Comparison of predicted and experimental frictional forces for Al-2024 at 470 m/min

The shear stress model predicts the frictional forces fairly well for all cutting speeds. However, the error estimate of the model is less at higher cutting speeds and feed rates. For low cutting speed, the shear stress model estimate is moderate such that it slightly underpredicts the experiments. However, the model still captures the trend of experimental data at low cutting speed.

Comparison of theoretical normal forces obtained from the stress model and experimental normal forces are presented in Figures 5.7 – 5.10 for Al-2024.

Compared to frictional force prediction, normal force predictions are moderately good and agree with the pattern given by the experimental data. Similar to shear force prediction, the normal stress model successfully predicts the normal forces, especially at higher cutting speeds. At higher feed rates and depths of cut, accuracy of the model decreases as was observed in the shear stress model.

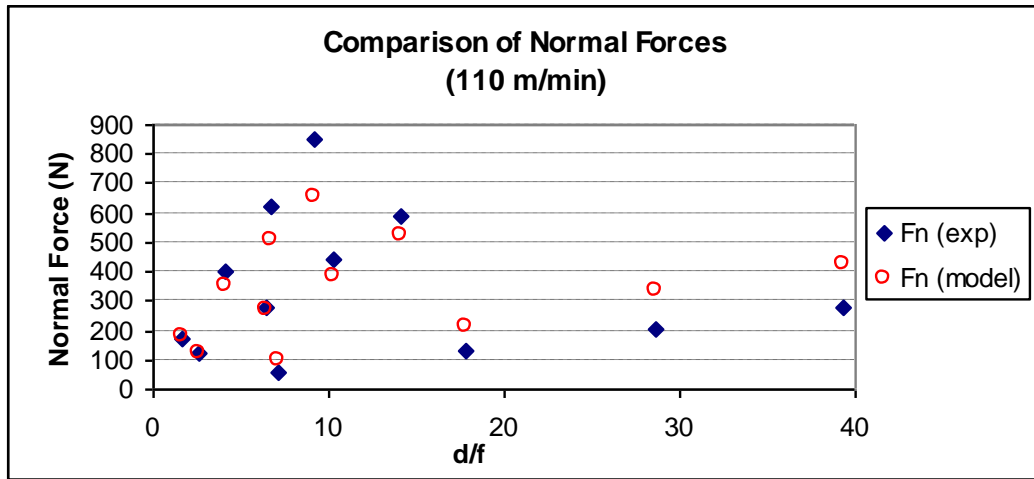


Figure 5.7. Comparison of predicted and experimental normal forces for Al-2024 at 110 m/min

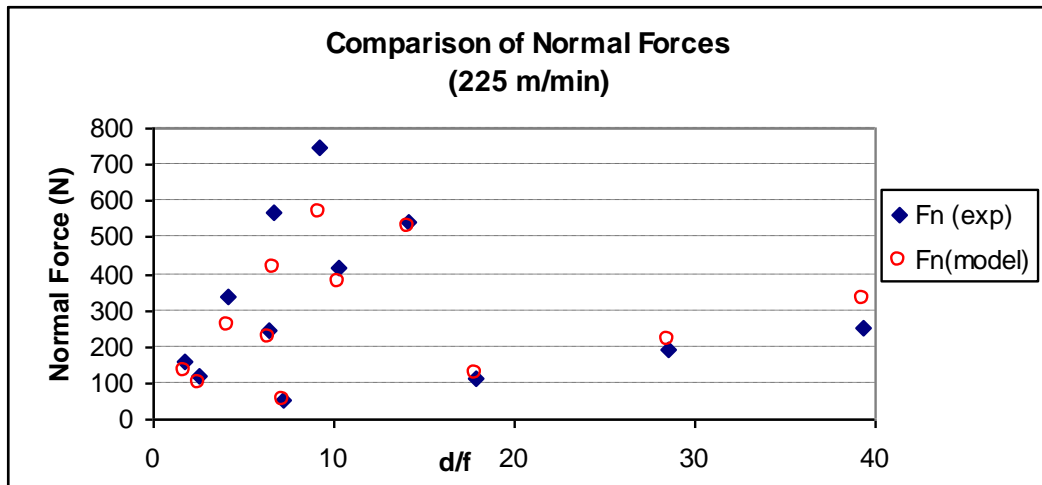


Figure 5.8. Comparison of predicted and experimental normal forces for Al-2024 at 225 m/min

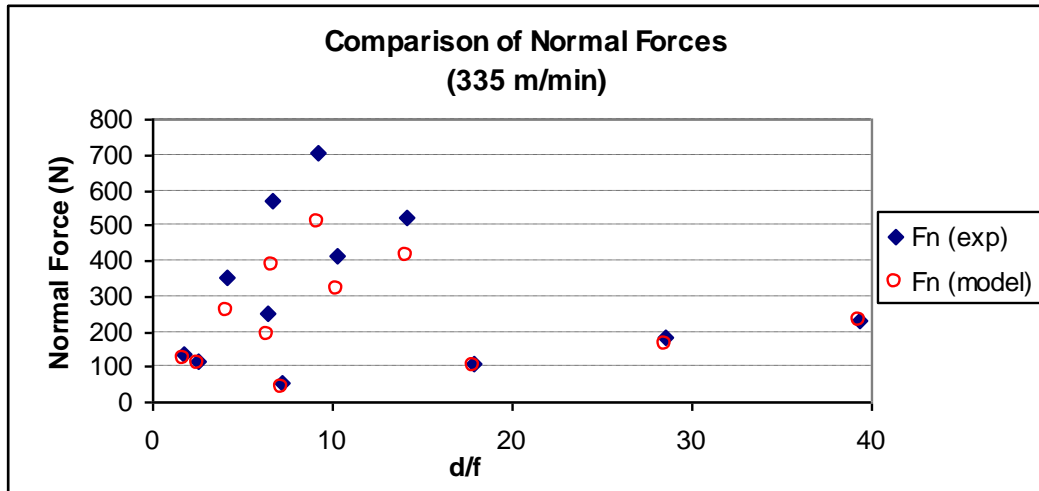


Figure 5.9. Comparison of predicted and experimental normal forces for Al-2024 at 335 m/min

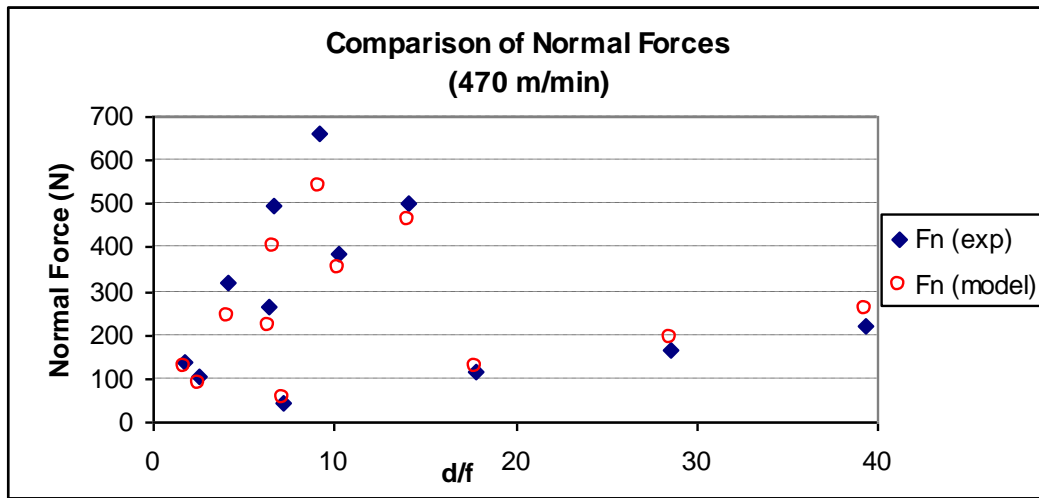


Figure 5.10. Comparison of predicted and experimental normal forces for Al-2024 at 470 m/min

Applying the same procedure to the results of experiments with Al-6061, we can make the following comparisons. Figures 5.11 – 5.18 reveal that the

model predictions for both normal and shear forces are in good agreement with the experimental data obtained for Al-6061.

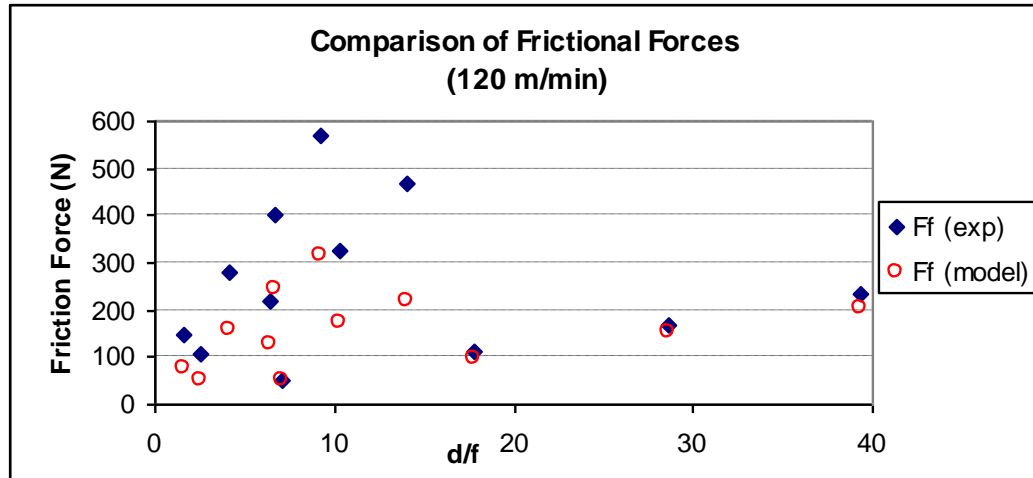


Figure 5.11. Comparison of predicted and experimental frictional forces for Al-6061 at 120 m/min

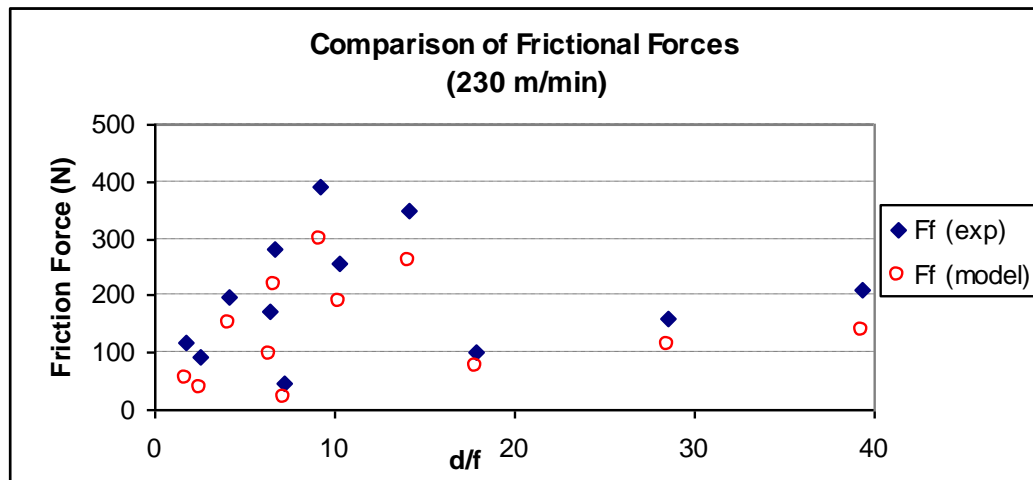


Figure 5.12. Comparison of predicted and experimental frictional forces for Al-6061 at 230 m/min

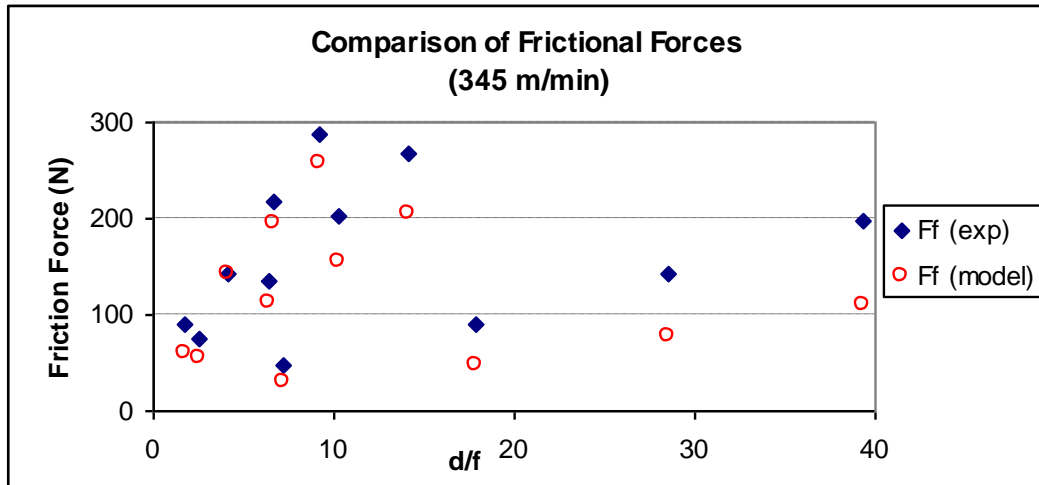


Figure 5.13. Comparison of predicted and experimental frictional forces for Al-6061 at 335 m/min

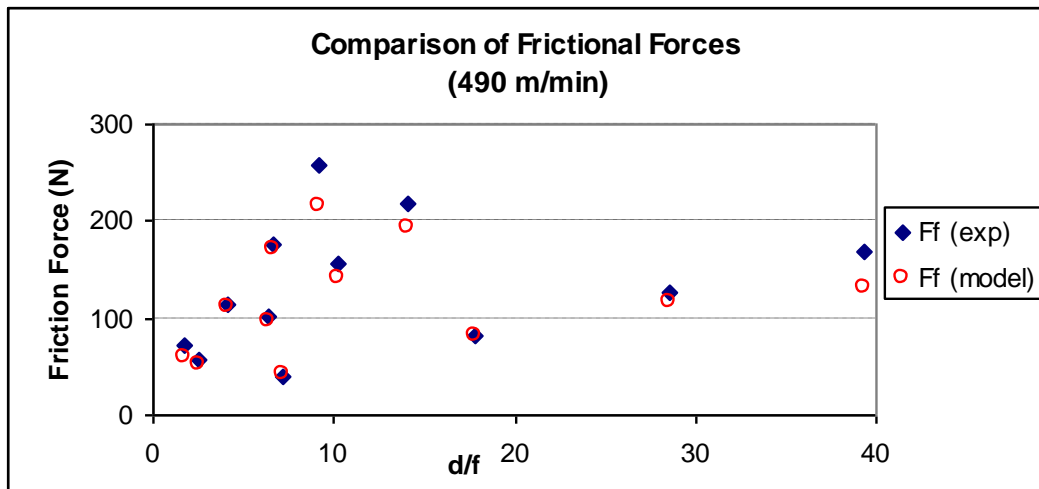


Figure 5.14. Comparison of predicted and experimental frictional forces for Al-6061 at 490 m/min

The shear stress model predicts frictional forces acting on the tool face interestingly well. For high cutting speeds, the model estimates the cutting forces

with minimum error, especially for small to moderate depth of cuts. For low cutting speeds, the deviation of the model from the experimental data points gets slightly larger.

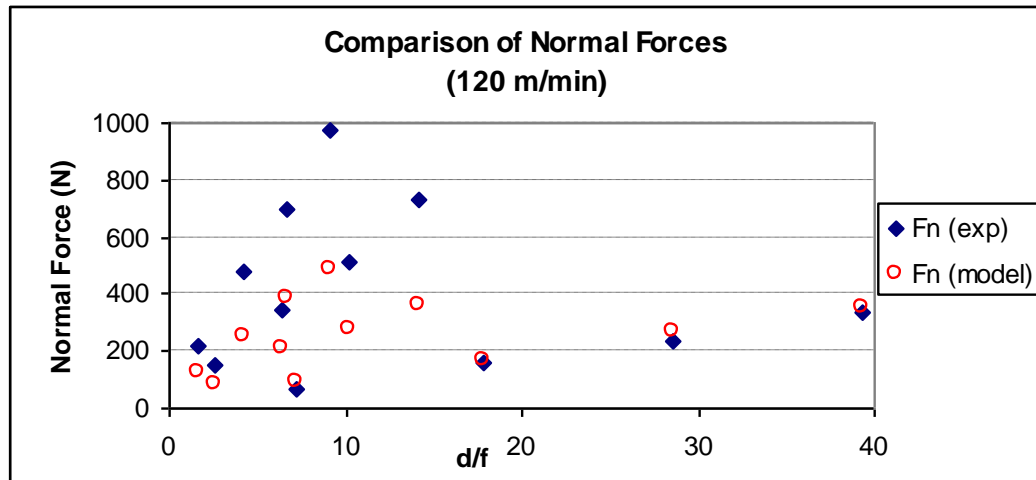


Figure 5.15. Comparison of predicted and experimental normal forces for Al-6061 at 120 m/min

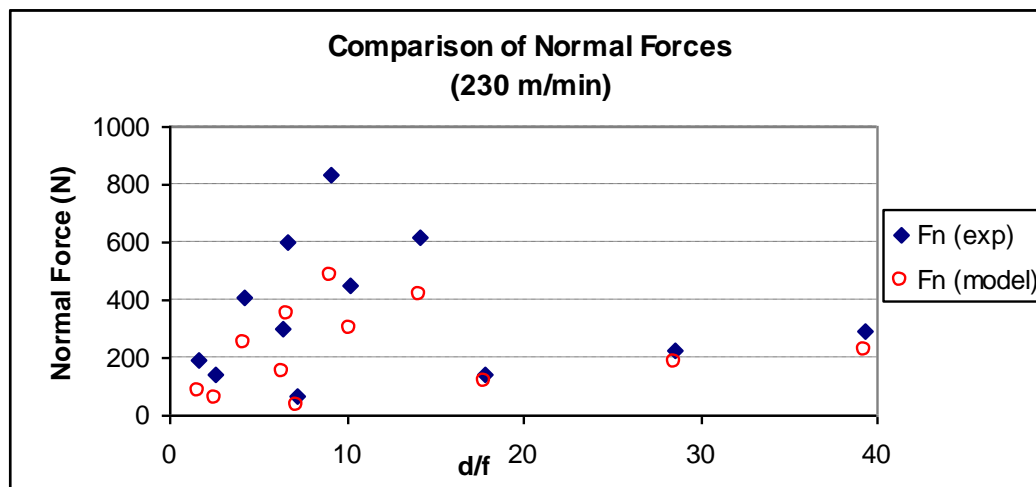


Figure 5.16. Comparison of predicted and experimental normal forces for Al-6061 at 230 m/min

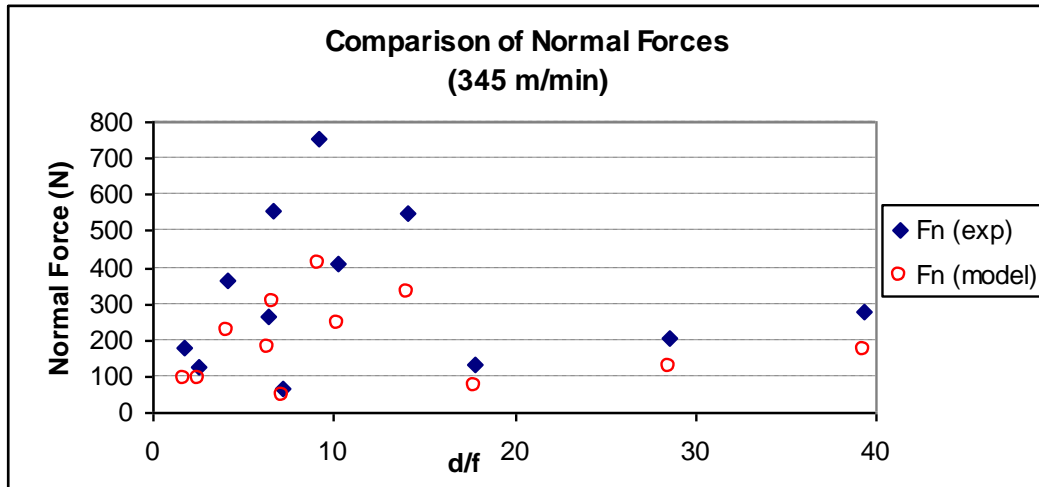


Figure 5.17. Comparison of predicted and experimental normal forces for Al-6061 at 345 m/min

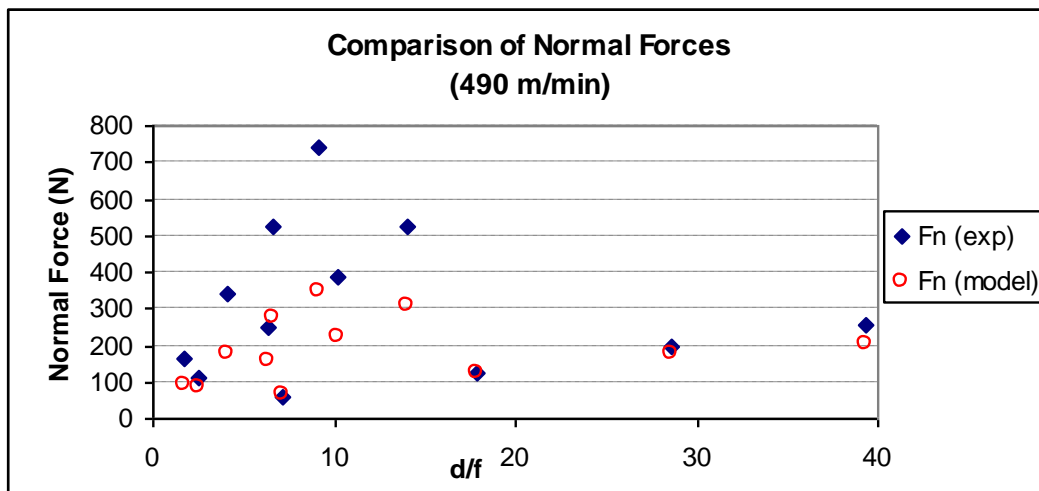


Figure 5.18. Comparison of predicted and experimental normal forces for Al-6061 at 490 m/min

As a last comparison, normal forces predicted by the stress model show the largest discrepancy. The error of estimate is larger compared to Al-2024 model estimates.

CHAPTER 6

CONCLUSION

It is well known that the macroscopic Coulombic law of friction is, in general, not applicable to the frictional interface conditions in machining because of the complex, and mostly unknown contact geometry. This thesis shows a detailed study at the microscopic level to gain an insight into this problem. The study was concentrated on oblique cutting of aluminum alloys due to the sticking characteristics of material. Oblique cutting was chosen to resemble the general machining process. The following observations and conclusions were made as a result of experimental analysis.

Experimental analysis showed that near the cutting edge and towards the end of tool-chip contact, sticking is the dominant mechanism when cutting of aluminum alloys with carbide tools at practical cutting speeds. Following the sticking zone near the cutting edge, there exists a sliding zone. These observations of the frictional conditions demonstrate the general inadequacy of the conventionally accepted frictional models.

The tangential resistance forces generated between chip and tool, in sliding zone result from interfacial friction. They can be determined from the Coulombic law of friction as long as the normal force is known at a particular location on the tool chip interface.

Sticking or adhesive friction results if the relative motion takes place within the chip material at some distance away from the interface. It is occurring as a form of shear of the contact asperities due to the tangential stress. The shearing action is observed as a deposited layer on the cutting tool.

Usually, both sticking and sliding friction occur simultaneously at the tool-chip interface. These physico-chemical processes are dynamic in nature, making the interfacial friction undetermined and complex.

Sticking can be defined as the strong chemical affinity of contact asperities, occurring as bond formation between the outermost layer atoms of undersurface of chip and tool surface. The types of intermolecular bonds and bond strength during the process are very difficult to determine with the available experimental methods. Friction depends on many internal and external parameters, such as oxide layer formation, cutting speed, and cutting time. The role of each parameter must be properly evaluated.

In this study, newer techniques were used to characterize the friction boundary conditions. Magnified images of tool chip interface obtained by SEM were very useful in identifying different friction zones. This method did not only serve to obtain the images, but with the backscattering technique, it also helped characterize the chemical composition of deposited layers. Furthermore, a computer code was generated to compute the area of the different zones within the SEM images. Consequently, the numerical values of sticking and sliding areas

and their relative positions were determined precisely. These results built the basis of a new friction model.

Other techniques such as LSCM scans and surface profilometer measurements were found to be efficient to visualize and characterize the 3-D surface topography. LSCM pictures are particularly useful in identifying the sticking area and built-up edge formation.

In the experiments, two different types of aluminum alloys, Al-2024 and Al-6061, were machined under the same cutting conditions with the same cutting tool geometry. A total of 96 experiments were carried out at four different cutting speeds, three different feed rates, and four different depths of cut. The cutting force dynamometer and data acquisition system were very effective in measuring and recording cutting forces.

Experimentally obtained tool surface topography was captured by SEM images. Backscattered SEM measurements revealed different chemical compositions in the deposited layers. Such results were construed as the evidence for the distinct friction zones. As a result of this methodology, it is concluded that friction conditions behave differently in three distinct zones:

1) Primary Sticking Zone: This zone is believed to occur as a result of the high normal force created by the edge effect or plowing force. At low cutting speeds, feed rates and shallow depths of cut, the primary sticking zone behaves as built-up edge. Plastically sheared metal in the primary shear plane contacts the tool surface in milliseconds. Material with low melting point tends to adhere to

the rake face. However, since the chip continuously moves, the adhesion layer shears off from the chip and builds-up. This phenomenon occurs very rapidly, so the material cannot find time to oxidize. Therefore, in this zone, material composition is very close to the raw aluminum material composition, irrespective of the cutting speed. As the cutting force, feed rate, and depth of cut increase, built-up edge formation disappears, and a profound sticking zone is observed. Experimental evidence showed that primary sticking area and cutting speed are inversely proportional. The primary sticking zone was observed in all experiments.

2) Sliding Zone: In this zone, the chip moves freely on the tool without any adhesion and shear. SEM images showed very little or no workpiece material in this zone. The ones observed were just the residues of the chip that filled the tool surface irregularities as a result of finite surface finish of the tool. Since there is no seizure in this zone, the conventional friction force model is applicable to this area. Except for low cutting speed, low feed rates, and shallow depths of cut, the sliding zone was always observed following the primary sticking zone.

3) Secondary Sticking Zone: Although the normal force is not as high as on the primary sticking zone, a secondary sticking zone was observed on the tool surface. The existence of this zone depends on the workpiece material, cutting speed, feed rate, and depth of cut, among which, cutting speed is the most dominant factor. Al-2024 exhibit no secondary sticking zone at low cutting speeds (110 m/min) and low feed rate; whereas, Al-6061 never showed secondary

sticking zone for all possible cutting speeds and low feed rates. This is a very remarkable observation of material effect on the friction evolution in our experiments. The secondary sticking zone occurred at moderate and high cutting speeds for Al-2024 no matter what the feed rate and depth of cut was. Al-6061 exhibit a secondary sticking zone at moderate and high cutting speeds and at high feed rates. This indicates that the Al-6061 is more prone to formation of built-up edge than the Al-2024, which supports the idea of better machinability rating of Al-2024 compared to Al-6061.

A difference in chemical composition on secondary sticking zone and the primary sticking zone is another intriguing observation that helped us to identify the built-up edge formation in primary and secondary sticking zone. It is a known fact that maximum tool temperatures occur at the back of the contact zone close to the separation point of chip and tool. Therefore, the chip temperature is higher on the secondary sticking zone compared to the primary sticking zone if a secondary zone exists. At elevated temperatures, the microstructure of aluminum alloys altered, and the metallic compounds formed by aluminum and its alloying elements were observed. This is the main reason of difference in chemical composition of deposits on seizure zones. Both Al-2024 and Al-6061 showed similar microstructural changes with different metallic compound formation.

Cutting force measurements served as another method to support the quantitative verification of the interfacial friction areas. Two types of forces occur on the tool-chip interface during cutting: normal forces and frictional forces. High

normal and shear forces observed on the primary sticking zone are due to the plowing effect of the cutting edge. In order to compare the experimentally measured forces with the forces obtained from the stress-friction model, the plowing force effect was removed from the cutting forces.

The proposed stress-friction model predicts the normal and friction force according to the frictional boundary conditions and associated stress values. Shear and normal stresses on the primary sticking zone and sliding zone are taken as constant after the plowing force is refined from the model. The frictional force associated in the primary sticking zone is the shear yield strength of the chip material. Accordingly, normal stress is taken as the yield strength of the material since the material is plastically deformed. This assumption does not take the plasticity effect into account. On the sliding zone, the normal stress is taken as the yield strength of the material; however, the frictional stress is due to pure sliding friction and is dependent on friction coefficient. In the secondary sticking zone, both normal and shear stress drops to zero at the chip separation point. Therefore, the stress is taken as the average value of the normal and shear stresses acting on primary sticking zone, assuming the decrease is linear.

In the final part of the study, normal and frictional forces predicted by the mathematical model were compared with the experimental data. Frictional forces are in good quantitative agreement at all cutting speeds for Al-2024. Frictional model validation is proved to be reliable at higher cutting speeds and feed rates. For low cutting speeds, although the general trend was observed, model

underestimates the frictional forces. Similar results were obtained with Al-6061. A deviation of model prediction from the experimental data was noted at the low cutting speeds.

Normal forces calculated by the model, and experimentally-measured normal forces, exhibit a larger discrepancy. At higher cutting speeds, the model predicts the normal forces. This probably happens due to the hardening effect of plastically deformed material having a larger flow stress than the yield strength. Compared to Al-6061, the normal force prediction is better for Al-2024.

The difference between model and experimental results can be a result of:

- Constant material properties assumption throughout the contact zone: This is a valid point since even experimental parameters, like cutting speed, feed rate and depth of cut might change the plastic flow stress.
- Friction area computations: Although the method of computation is well established and shows a close resemblance with the cutting conditions, image processing and analysis rely on the assumptions made in defining zones either as primary sticking, sliding and secondary sticking zones, especially where the boundaries are difficult to distinguish.
- Constant friction coefficient assumption and its numeric value used in the model.
- Errors associated with the force measurement.
- Errors in plowing force determination.

- Experimental errors due to difficulty in removing the chip during continuous chip formation

Many of the studies on friction in machining have used orthogonal cutting conditions to determine the domains of seizure and sliding as well as shear and normal stresses. In this thesis, tool-chip contact area is investigated at microscopic level in oblique machining to look beyond the Zorev's assumption of seizure followed by sliding. The model proposed in this study accounts for the nonlinearities associated in terms of frictional area determination and computations. Built-up edge formation, seizure and sliding vary for different cutting parameters, materials used, and cutting geometry. Even same materials with different alloying content show different interfacial contacts.

The proposed model needs to be further investigated for different cutting parameters, for different workpiece-cutting tool pairs, and cutting tool geometries to be universally accepted.

In conclusion, an experimental methodology was used to gain insight and better understanding about the friction phenomenon and the boundary conditions at the tool-chip interface in oblique cutting of aluminum alloys. The SEM technique was successfully used to identify and compute different frictional conditions precisely. The chemical composition identification of materials on different sticking zones proofed the necessity of multiple contact zone models. The developed model was accurately predicted the cutting forces for most tested conditions.

Coupling frictional boundary conditions with the stress model needs to be further studied in order to obtain a unified theory that will apply to various workpiece-tool combinations irrespective of cutting parameters and tool geometry. Mathematical relationships could be better defined to reflect these findings. A comprehensive cost-benefit analysis could be performed to identify key factors and lead to automated tool replacement. Multi-scale modeling of friction can also lead to better models for nano- and micro-machining.

REFERENCES

1. Piispanen, V., (1937). Lastunmuodostumisen Teoriaa. *Teknillinen Aikakauslehti*, 27(5), 315.
2. Ernst, H., Merchant, M.E., (1940). Surface Friction of Clean Metals – A Basic Factor the Metal Cutting Progress. *Proceedings of the Special Summer Conference on Friction and Surface Finish*.
3. Ernst, H., Merchant, M.E., (1941). Chip Formation, Friction and High Quality Machined Surfaces, from Surface Treatment of Metals. *Transactions of ASME*, 29, 299-328.
4. Chao, B. T., Trigger, K. J., (1951). Cutting temperatures and metal-cutting phenomena. *Transactions of the ASME*, 73, 777-793.
5. Lee, E.H., Shaffer, B.W., (1951). The Theory of plasticity applied to a problem of machining. *Journal of Applied Mechanics, Transactions of ASME*, 73, 405-413.
6. Shaw, M. C., Cook, N. H., Finnie, I., (1953). The Shear-Angle Relationship in Metal Cutting. *Transactions of ASME*, 75, 273-288.
7. Kobayashi, S., Thomsen, E.G., (1959). Some Observations on the shearing process in metal cutting. *Journal of Engineering for Industry*, 81(3), 251-262.
8. Dewhurst, P., (1978). On the uniqueness of the machining process, *Proc. R. Soc. Lond.*, A360, 587-610.
9. Shaw, M. C., (1984) *Metal Cutting Principles*, Oxford University Press, 1-38.
10. Oxley, P. L. B., (1989). *Mechanics of Machining: An Analytical Approach to Assessing Machinability*, Ellis Horwood Ltd., 1-69.

11. Roth, R. N., Oxley, P. L. B., (1972). A slipline field analysis for orthogonal machining based on experimental flow fields, *J. Mech. Eng. Sci.*, 14, 85-97.
12. Bowden, F.P., Tabor, D., (1986). *The friction and lubrication of solids*, Clarendon Press, 1-40.
13. Green, A.P., (1955). Friction between unlubricated metals: a theoretical analysis of the junction model, *Proc. R. Soc. Lond.*, A228, 191-204.
14. Zorev, N. N., (1963). Interrelation between Shear Processes Occurring along Tool Face on Shear Plane in Metal Cutting. *International Research in Production*, 42-49.
15. Wallace, P. W., Boothroyd, G., (1964). Tool Forces and Tool-Chip Friction in Orthogonal Machining. *Journal Mechanical Engineering Science*, 6(1), 74-87.
16. Doyle. E.D., Horne, J.G. and Tabor, D., (1979). Frictional interactions between chip and rake face in continuous chip formation, *Proc. R. Soc. Lond.*, A336, 173-183.
17. Trent, E.M., (1988). Metal cutting and the tribology of seizure: I-Seizure in metal cutting, *Wear*, 128, 29-45.
18. Horne, J.G., Doyle, E.D., and Tabor, D., (1978). Lubrication Challenges in Metalworking and Processing, *IIT Research Institute*, 1-3.
19. Wright, P. K (1981). Frictional interactions in machining: comparisons between transparent sapphire and steel cutting tools. *Metals Technology*, 150-160.
20. Wright, P. K., Horne, J. G., Tabor, D., (1979). Boundary Conditions at the Tool-Chip Interface in Machining: Comparison between Seizure and Sliding Friction. *Wear*, 54, 371-390.

21. Challen, J.M., Oxley, P.L.B., (1979). An explanation of the different regimes of friction and wear using asperity deformation models, *Wear*, 53, 229-243.
22. Takeyama, H., Usui, E., (1958). The Effect of Tool-Chip Contact Area in Metal Machining. *Transactions of ASME*, 80, 1089-1096.
23. Usui, E., Hirota, A., (1978). Analytical Prediction of Three Dimensional Cutting Processes. Part 2: Chip Formation and Cutting Force with Conventional Single-Point Tool. *Journal of Engineering for Industry*, 100, 229-235.
24. Guha, D., (1999). Boundary Conditions in Machining and Their Fractal Applications, M.Sc. Thesis, University of Oklahoma.
25. Raman, S., Longstreet, A., Guha, D. (2002). A Fractal View of Tool-Chip Interfacial Friction in Machining. *Wear*, 253, 1111-1120.
26. Colwell, L.V., (1954). Predicting the angle of chip-flow for single-point cutting tool. *Transactions of ASME*, 76, 199-204.
27. Stabler, G.V., (1951). The fundamental geometry of cutting tool. *Proc. Inst. Mech. Eng.*, 165(63), 14-21.
28. Armarego, E.J.A., and Brown, R.H., (1969). *The machining of metals*, Prentice Hall Inc., 1-50.
29. Young, H.T., Mathew. P., Oxley, P.L.B., (1987). Allowing for nose radius effects in predicting the chip flow direction and cutting forces in bar turning. *Proc. Inst. Mech. Eng.*, 201(3), 213-226.
30. Wang, J., Mathew, P., (1995). Development of a general tool model for turning operations based on a variable flow stress theory. *International Journal of Machine Tools & Manufacture*, 35(1), 71-90.

31. Arsecularatne, J. A. Mathew, P., Oxley, P. L. B., (1995). Prediction of chip flow direction and cutting forces in oblique machining with nose radius tools. *Proc. Inst. Mech. Eng., Part B: Journal of Engineering Manufacture*, 209, 305-315.
32. Jawahir, I.S., Dillon, O.W. Jr., Balaji, A. K., Redetzky, M., Fang, N., (1998). Predictive modeling of machining performance in turning operations, *Machining Science and Technology*, 2(2), 253-276.
33. Ghosh, F., (1986). Cutting forces model based on equivalent cutting edge in oblique cutting, *Journal of Engineering for Industry*, 108, 259-307.
34. Barrow, G., Graham, W., Kurimoto, T., Leong, Y.F., (1981). Rake face stress distributions in orthogonal machining, *International Journal of Machine Tool, Design and Research*, 22(1), 75-85.
35. Andreev, G.S., (1958). Photoelastic study of stresses in a cutting tool using cinematography, *Vestn. Mashinostroeniya*, 38(5). 54-57.
36. Kattwinkel, W., (1960). Untersuchungen an Schneiden spanender Werkzeuge mit hilfe der Spannungsoptic, *Industr.-Anzeiger*, 37, 29-33.
37. Usui, E., Takeyama H. (1960). A Photoelastic Analysis of Machining Stresses. *Journal of Engineering for Industry*, 82(4), 303-308.
38. Rice, W. B., Syniuta, S., Syniuta, W. D., (1960). Photoelastic determination of cutting tool stresses, *Trans. Engage. Inst. Can*, 4, 20-23.
39. Chandrasekaran, H., Kapoor, D.V., (1965). Photoelastic Analysis of Tool-Chip Interface Stresses. *Journal of Engineering for Industry*, 87, 495-502.
40. Amini, E., (1968). Photoelastic analysis of stresses and forces in steady cutting, *J. Strain Analysis*, 3(3), 206-213.

41. Bagchi, A., Wright, P. K., (1987). Stress analysis in machining with the use of sapphire tools, *Proc. R. Soc. Lond*, A409, 99-113.
42. Arsecularatne, J. A. (1997). On Tool-Chip Interface Stress Distributions, Ploughing Force and Size Effect in Machining. *International Journal of Machine Tools and Manufacture*, 37(7), 885-899.
43. Kato, S., Yamaguchi, K., Yamada, M. (1972). Stress Distribution at the Interface between Tool and Chip in Machining. *Journal of Engineering for Industry*, 94(2), 683-689.
44. Usui, E., and Shirakashi, T., (1982). Mechanics of machining – from descriptive to predictive theory. *On the Art of Cutting Metals – 75 Years Later*, ASME, 13-35.
45. Buryta, D., Sowerby, R., Yellowley, I., (1994). Stress distribution on the rake face during orthogonal machining, *Int. J. Mach. Tools Manufact.* 34(5), 721-739.
46. Childs, T. H. C. and Mahdi, M. I., (1989). On the stress distribution between the chip and tool during metal turning, *Ann. CIRP*, 38(1), 55-58.
47. Askathov, V.P, *Metal Cutting Mechanics*, CRC Press LLC. 70-78.
48. Smith, W. F., (1981). *Structure and Properties of Engineering Alloys*, McGraw-Hill.
49. Asby, M. F., Jones, D. R. H., (1986), *Engineering Materials: An Introduction to Microstructures, Processing and Design*, Pergamon Press.
50. Madhavan, V., Chandrasekar, S., Farris, T. N. (2002). Direct Observations of the Chip-Tool Interface in the Low Speed Cutting of Pure Metals. *Journal of Tribology*, 124, 617-626.

51. Lee, L. C., Liu, X. D., Lam, K. Y. (1995). Determination of Stress Distribution on the Tool Rake Face Using a Composite Tool. *International Journal of Machine Tools and Manufacture*, 35(3), 373-382.
52. Hu, R. S., Mathew, P., Oxley, P. L. B., Young, H. T. (1986). Allowing for End Cutting Edge Effects in Predicting Forces in Bar Turning with Oblique Machining Conditions. *Proceedings of the Institution of Mechanical Engineers*, 200, 89-99.
53. Lin, G. C. I., Mathew, P., Oxley, P. L. B., (1982). Predicting Cutting Forces for Oblique Machining Conditions. *Proceedings of the Institution of Mechanical Engineers*, 196, 141-148.
54. Merchant, M. E., (1945). Mechanics of Metal Cutting Process. II. Plasticity Conditions in Orthogonal Cutting. *Journal of Applied Physics*, 16, 318-324.
55. Shaw, M. C., Cook, N. H., Smith, P. A., (1952). The Mechanics of Three-Dimensional Cutting Operations. *Transactions of ASME*, 74, 1055-1064.
56. Kirk, J.A., Anand, D.K., McKindra, C., (1977). Matrix Representation and Prediction of three-dimensional cutting forces. *Journal of Engineering for Industry*, 828-834.
57. Brown, C. A., Von Turkovic, B. F. (1983). A Practical Method for Estimating Machining Forces from Tool-Chip Contact Area. *Annals of the CIRP*, 32(1), 91-95.
58. Arsecularatne, J. A., Fowle, R. F., Mathew, P. (1996). Nose Radius Oblique Tool: Cutting Force and Built-Up Edge Prediction. *International Journal of Machine Tools and Manufacture*, 36(5), 585-595.
59. Rao, B. C., Shin, Y. C. (1999). A Comprehensive Dynamic Cutting Force Model for Chatter Prediction in Turning. *International Journal of Machine Tools and Manufacture*, 39, 1631-1654.

APPENDIX A

MATLAB CODE

```
MATLAB® Code (Cleaning Code)
clear
clc
[im,map]=imread('T1C1(ML)','bmp');

% ##### DEFINING REGIONS #####

for i=1:1900
    for j=1:1300
        if im(i,j) <= 150;
            im(i,j) = 10;
        end
        if (im(i,j) > 150) & (im(i,j) < 253);
            im(i,j)=200;
        end
        if im(i,j)>= 253;
            im(i,j)=255;
        end
    end
end

% ##### CLEAN UP IMAGE #####

    for i=6:1895
        for j=1:1300
            if (im(i,j)==10 );

if(((im(i+1,j)==200)||(im(i+2,j)==200)||(im(i+3,j)==200)||(im(i+4,j)==200)||(im(i+
5,j)==200))&&((im(i-1,j)==200)||(im(i-2,j)==200)||(im(i-3,j)==200)||(im(i-
4,j)==200)||(im(i-5,j)==200)));
                im(i,j)=200;
            end
        end
    end
end
end

for i=1:1900
    for j=6:1295
```



```

        if (im(i,j)==10 );

if(((im(i,j+1)==200)||(im(i,j+2)==200)||(im(i,j+3)==200))&&((im(i,j-
1)==200)||(im(i,j-2)==200)||(im(i,j-3)==200)));
        im(i,j)=200;
        end
    end
end
end

% ##### CREATING IMAGES #####

for i=1:1900
    for j=1:1300
        if im(i,j) == 255;
            u(i,j) = 255;
        elseif im(i,j) == 200;
            u(i,j) = 200;
        else im(i,j) == 10;
            u(i,j) = 10;
        end
    end
end
% read image may not be gray scale..hence assign
map = colormap(gray(256));
figure(1)
colormap(gray(256))
image(u)
colormap(gray(256))
imwrite(u,map,'FirstRun.bmp');

clear
clc
[im,map]=imread('T2C4(ML2)','bmp');

```

MATLAB® Code (Area Calculation)

```
% ##### COUNTING AREAS #####
```

```
StickingA=0;
StickingB=0;
Sliding=0;
ToolBackground=0;
LineCnt=0;
for i=1:1900
    for j=1:1300
        if im(i,j) == 9;
            StickingA = StickingA + 1;
        elseif im(i,j) == 225;
            Sliding = Sliding + 1;
        elseif im(i,j)==128;
            StickingB=StickingB+1;
        else (im(i,j) == 199)||(im(i,j)==100);
            ToolBackground=ToolBackground+1;
        end
    end
end
Total = StickingA + StickingB+ Sliding + ToolBackground+LineCnt;
c = (1580*10^(-3))/sqrt(1900*1300);
StickingAreaA = c^2 * StickingA;
StickingAreaB = c^2 * StickingB;
SlidingArea = c^2 * Sliding;
ToolBackgroundArea = c^2 * ToolBackground;
CombinedStickingArea=StickingAreaA+StickingAreaB;
CombinedStickingSliding = StickingAreaA+StickingAreaB+SlidingArea;
TotalToolArea = CombinedStickingSliding + ToolBackgroundArea;
```

```
% ##### CREATING IMAGES #####
```

```
for i=1:1900
    for j=1:1300

        if im(i,j) >= 253; % white space
            u(i,j) = 255; % All
            v(i,j) = 255; %First Sticking
            w(i,j) = 255; %Second Sticking
            x(i,j) = 255; %Sliding
            y(i,j) = 255; % Total Sticking
```

```

        z(i,j) = 255; %Total Contact Area
    end
    if (im(i,j) == 199)|| (im(i,j)==100);%toolbackground
        u(i,j) = 199;
        v(i,j) =255;
        w(i,j) = 255;
        x(i,j) = 255;
        y(i,j) = 255;
        z(i,j) = 255;

    end
    if im(i,j) == 9; %first sticking
        u(i,j) = 10;
        v(i,j) =10;
        w(i,j) = 255;
        x(i,j) = 255;
        y(i,j) = 10;
        z(i,j) = 10;
    end
    if im(i,j)== 128; %second sticking
        u(i,j) = 128;
        v(i,j) = 255;
        w(i,j) = 10;
        x(i,j) = 255;
        y(i,j) = 10;
        z(i,j) = 10;
    end
    if im(i,j)==225; %sliding
        u(i,j) = 225;
        v(i,j) = 255;
        w(i,j) = 255;
        x(i,j) = 10;
        y(i,j) = 255;
        z(i,j) = 10;
    end
end
end
end
% read image may not be gray scale..hence assign
% Write Everything Image
map = colormap(gray(256));
figure(1)
colormap(gray(256))
image(u)
colormap(gray(256))

```

```
imwrite(u,map,'Run2All.bmp');

figure(2)
colormap(gray(256))
image(v)
imwrite(v,map,'Run2FirstSticking.bmp');

figure(3)
colormap(gray(256))
image(w)
imwrite(w,map,'Run2SecondSticking.bmp');

figure(4)
colormap(gray(256))
image(x)
imwrite(x,map,'Run2Sliding.bmp');

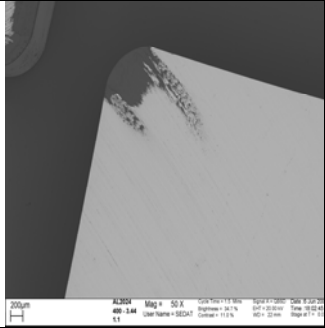
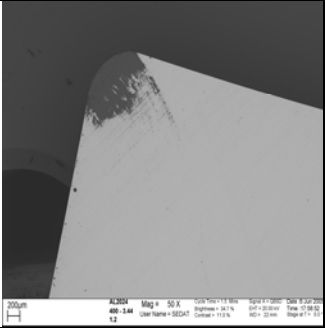
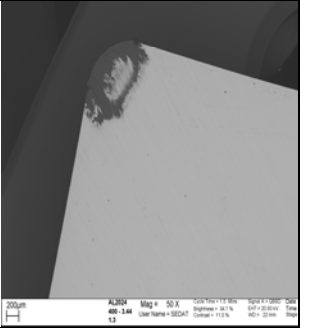
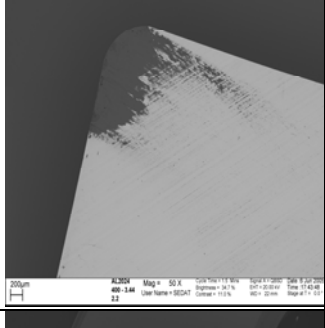
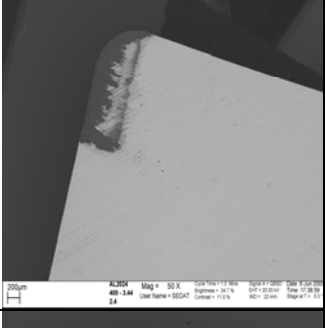
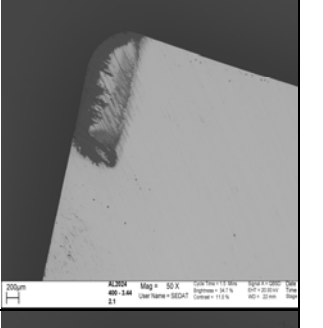
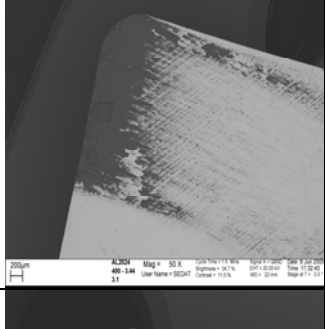
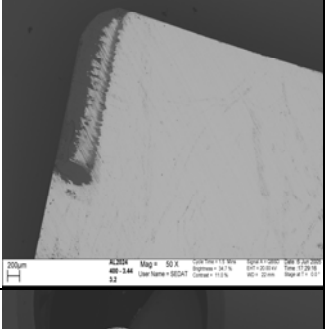
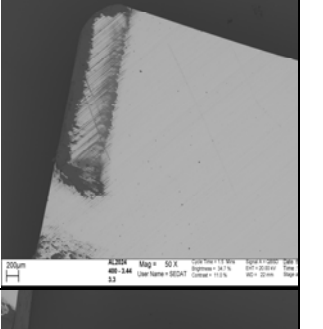
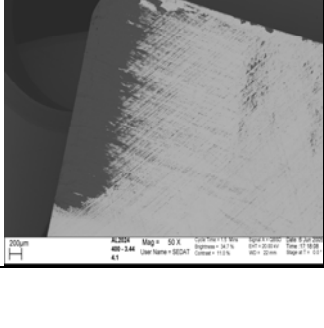
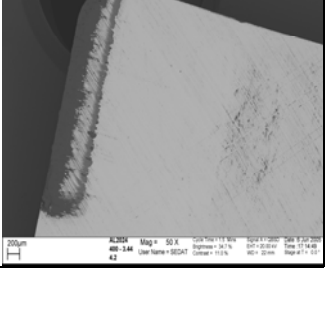
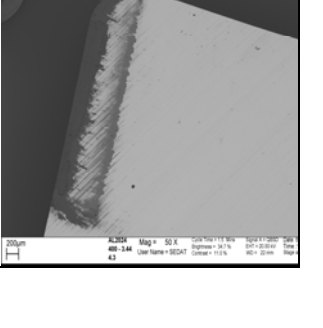
figure(5)
colormap(gray(256))
image(y)
imwrite(y,map,'Run2TotalSticking.bmp');

figure(6)
colormap(gray(256))
image(z)
imwrite(z,map,'Run2TotalContactRegion.bmp');

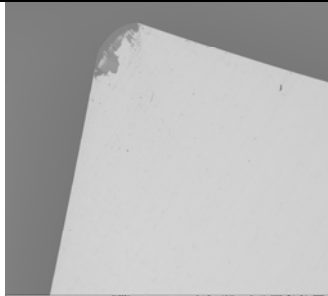
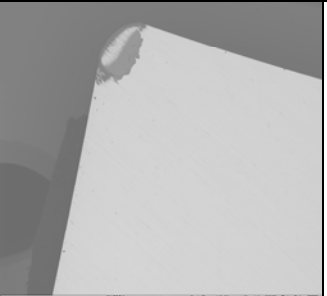
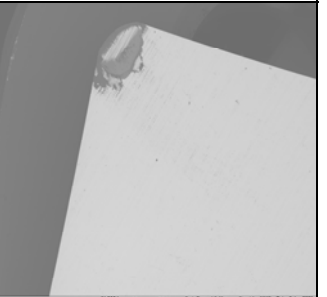
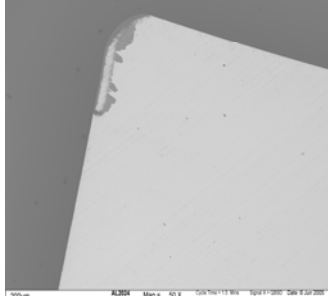
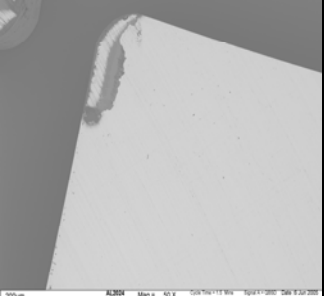
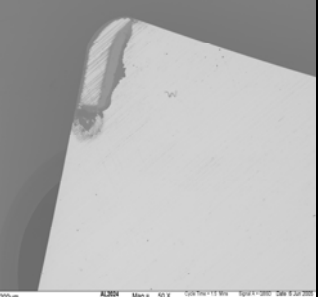
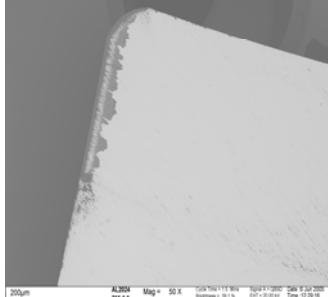
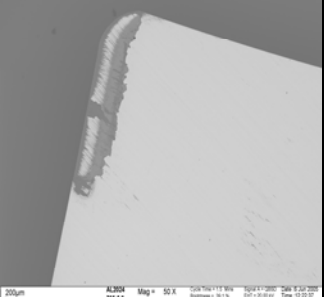
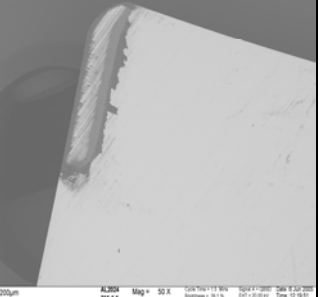
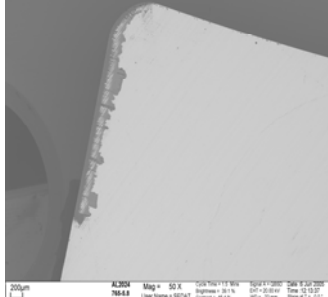
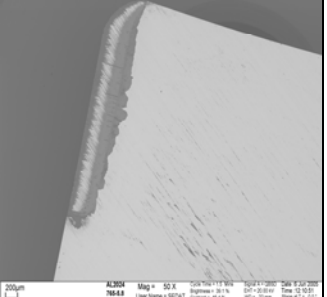
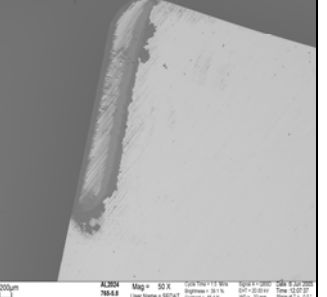
StickingAreaA
StickingAreaB
SlidingArea
ToolBackgroundArea
CombinedStickingArea
CombinedStickingSliding
TotalToolArea
```

APPENDIX B


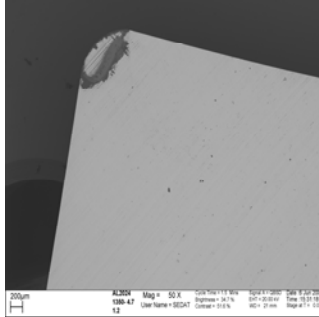
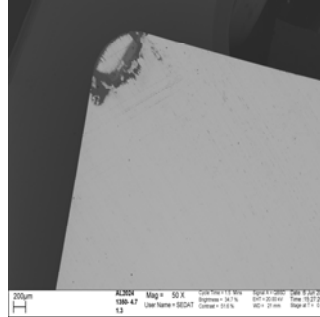
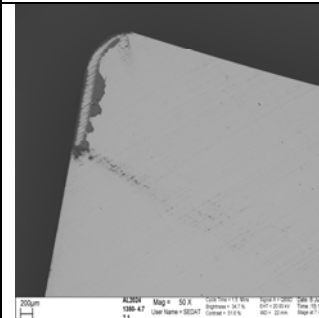
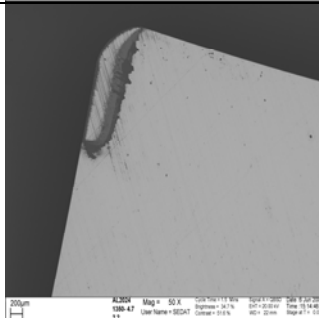
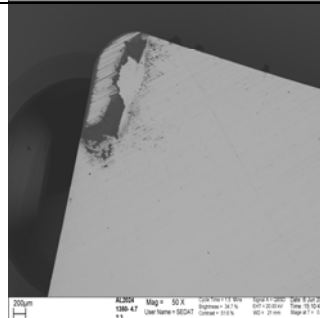
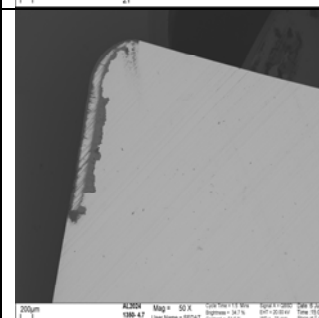
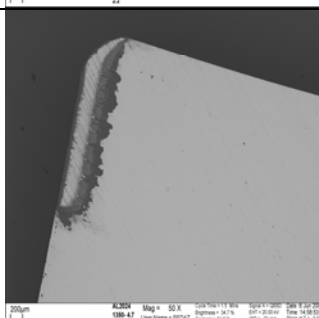
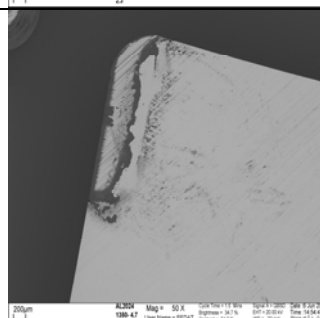
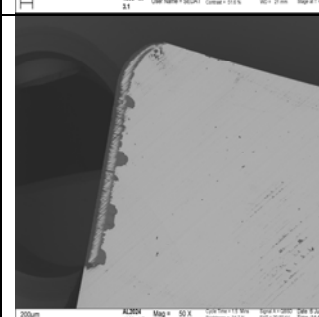
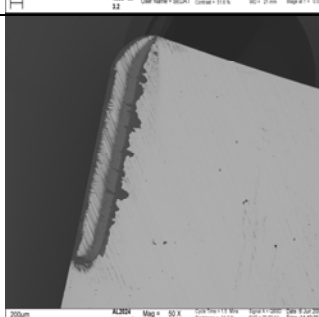
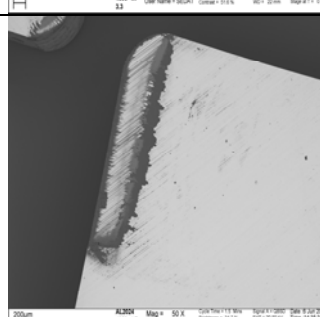
SEM Images for Al-2024 at 110 m/min

d mm	f = 0.071 mm/rev	f = 0.198 mm/rev	f = 0.305 mm/rev
0.51			
1.27			
2.03			
2.79			

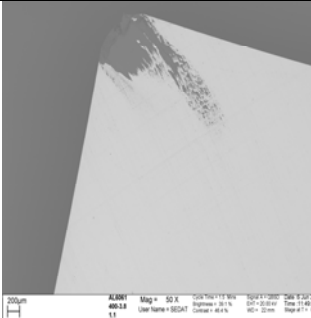
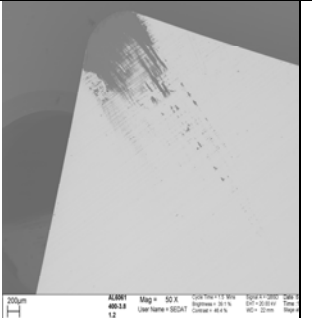
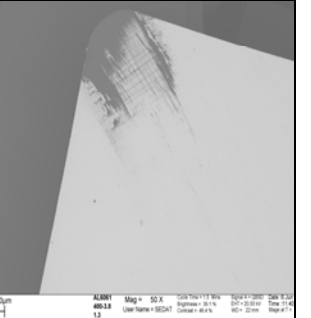
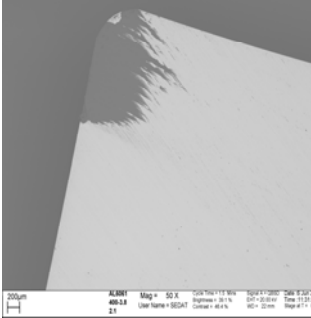
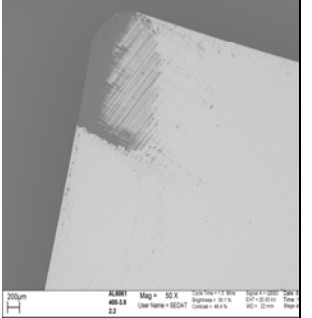
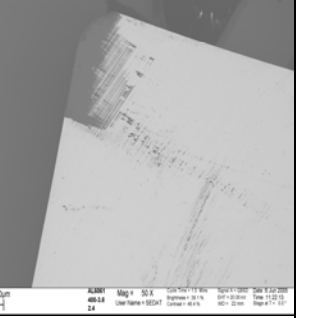
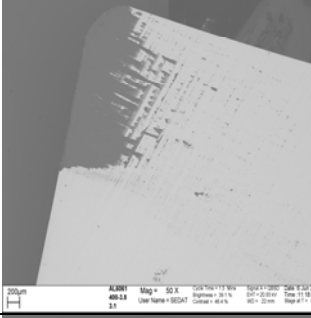
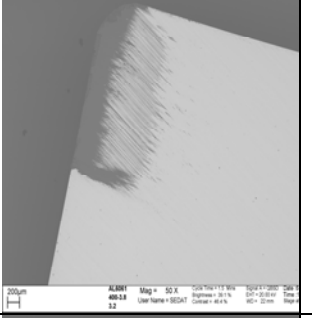
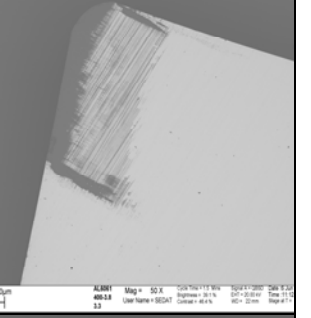
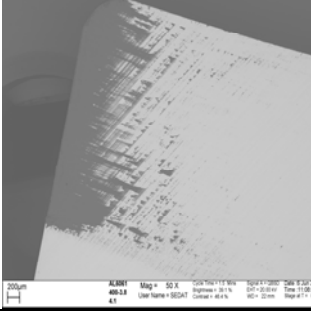
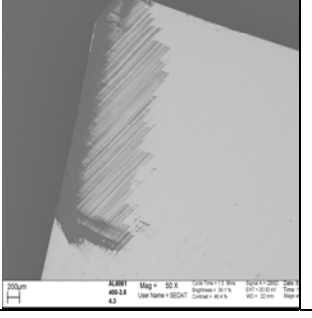
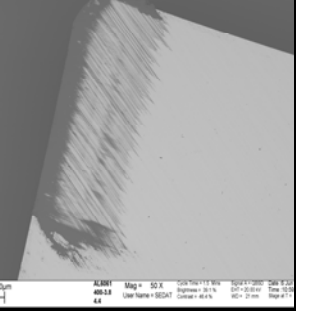
SEM Images for Al-2024 at 335 m/min

d mm	f = 0.071 mm/rev	f = 0.198 mm/rev	f = 0.305 mm/rev
0.5 1			
1.2 7			
2.0 3			
2.7 9			

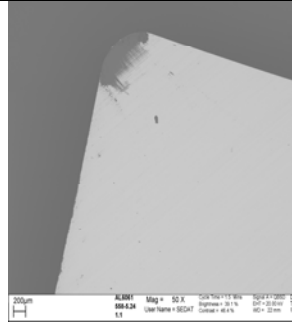
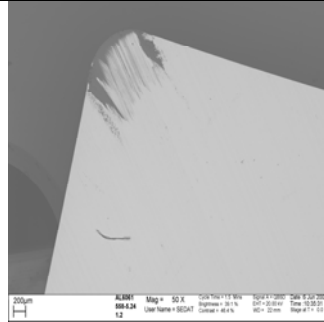
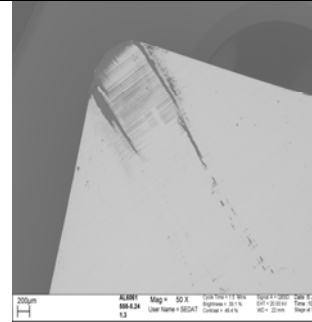
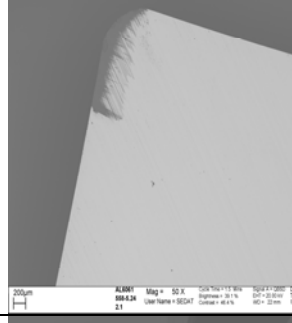
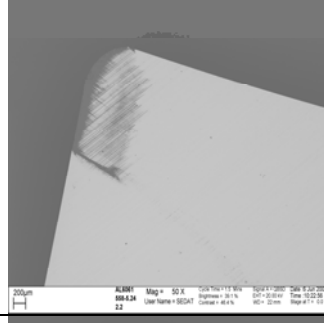
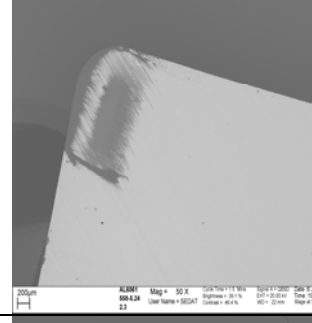
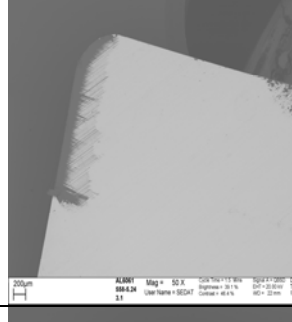
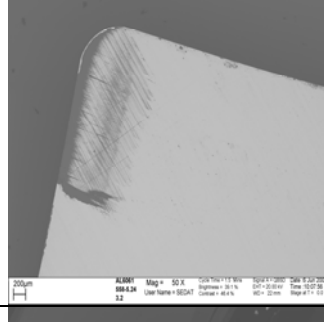
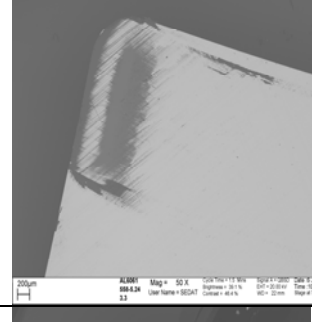
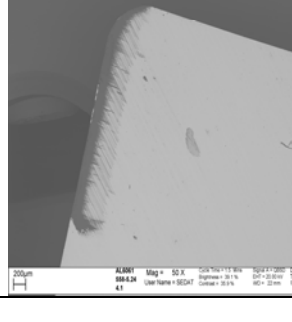
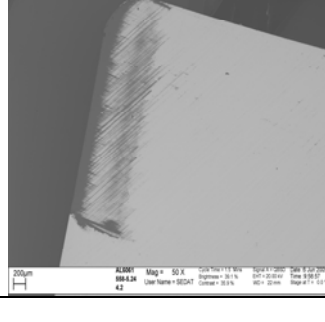
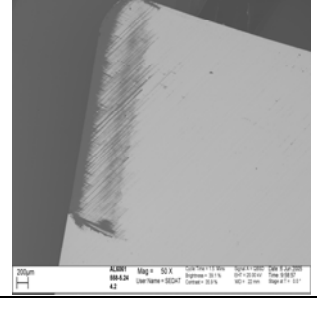
SEM Images for Al-2024 at 470 m/min

d mm	f = 0.071 mm/rev	f = 0.198 mm/rev	f = 0.305 mm/rev
0.51			
1.27			
2.03			
2.79			

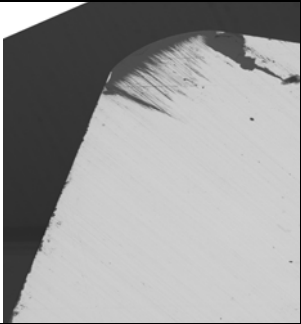
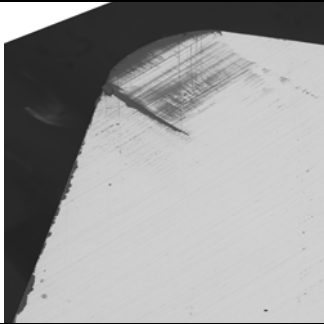
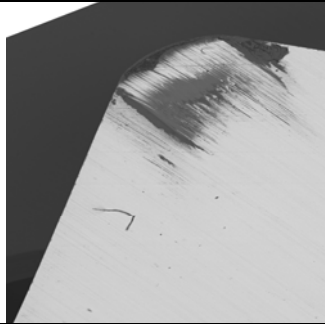
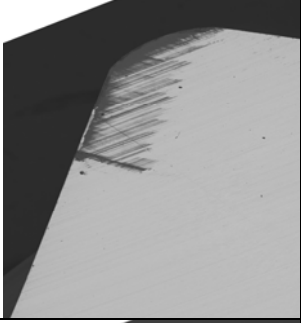
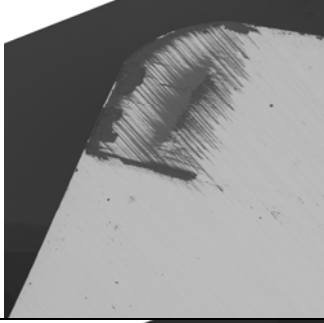
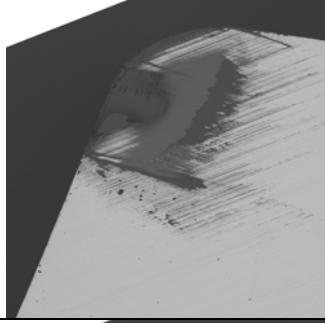
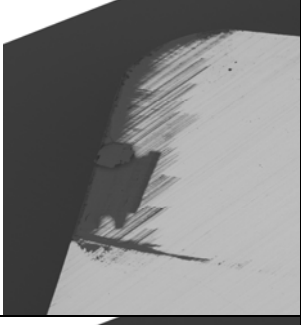
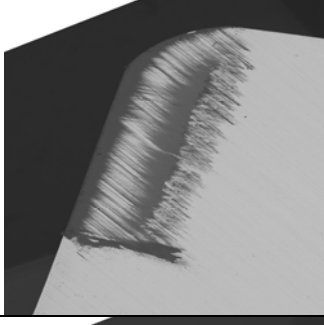
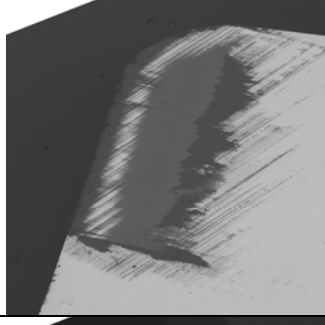
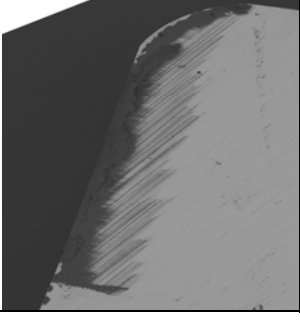
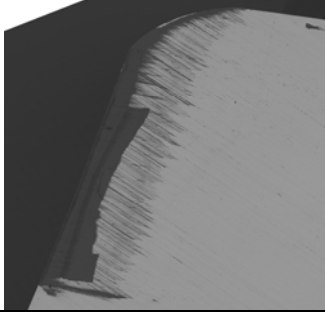
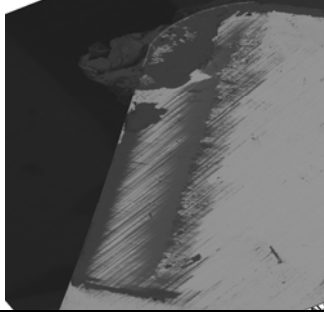
SEM Images for Al-6061 at 120 m/min

d mm	f = 0.071 mm/rev	f = 0.198 mm/rev	f = 0.305 mm/rev
0.51	 ALM01 Mag = 50 X 10/10/11 10/10/11 10/10/11 10/10/11 10/10/11 400.13 User Name = SEDAT Contrast = 40.0% 10/10/11 10/10/11 10/10/11 10/10/11 10/10/11 1.1	 ALM01 Mag = 50 X 10/10/11 10/10/11 10/10/11 10/10/11 10/10/11 400.13 User Name = SEDAT Contrast = 40.0% 10/10/11 10/10/11 10/10/11 10/10/11 10/10/11 1.2	 ALM01 Mag = 50 X 10/10/11 10/10/11 10/10/11 10/10/11 10/10/11 400.13 User Name = SEDAT Contrast = 40.0% 10/10/11 10/10/11 10/10/11 10/10/11 10/10/11 1.3
1.27	 ALM01 Mag = 50 X 10/10/11 10/10/11 10/10/11 10/10/11 10/10/11 400.13 User Name = SEDAT Contrast = 40.0% 10/10/11 10/10/11 10/10/11 10/10/11 10/10/11 2.1	 ALM01 Mag = 50 X 10/10/11 10/10/11 10/10/11 10/10/11 10/10/11 400.13 User Name = SEDAT Contrast = 40.0% 10/10/11 10/10/11 10/10/11 10/10/11 10/10/11 2.2	 ALM01 Mag = 50 X 10/10/11 10/10/11 10/10/11 10/10/11 10/10/11 400.13 User Name = SEDAT Contrast = 40.0% 10/10/11 10/10/11 10/10/11 10/10/11 10/10/11 2.3
2.03	 ALM01 Mag = 50 X 10/10/11 10/10/11 10/10/11 10/10/11 10/10/11 400.13 User Name = SEDAT Contrast = 40.0% 10/10/11 10/10/11 10/10/11 10/10/11 10/10/11 3.1	 ALM01 Mag = 50 X 10/10/11 10/10/11 10/10/11 10/10/11 10/10/11 400.13 User Name = SEDAT Contrast = 40.0% 10/10/11 10/10/11 10/10/11 10/10/11 10/10/11 3.2	 ALM01 Mag = 50 X 10/10/11 10/10/11 10/10/11 10/10/11 10/10/11 400.13 User Name = SEDAT Contrast = 40.0% 10/10/11 10/10/11 10/10/11 10/10/11 10/10/11 3.3
2.79	 ALM01 Mag = 50 X 10/10/11 10/10/11 10/10/11 10/10/11 10/10/11 400.13 User Name = SEDAT Contrast = 40.0% 10/10/11 10/10/11 10/10/11 10/10/11 10/10/11 4.1	 ALM01 Mag = 50 X 10/10/11 10/10/11 10/10/11 10/10/11 10/10/11 400.13 User Name = SEDAT Contrast = 40.0% 10/10/11 10/10/11 10/10/11 10/10/11 10/10/11 4.2	 ALM01 Mag = 50 X 10/10/11 10/10/11 10/10/11 10/10/11 10/10/11 400.13 User Name = SEDAT Contrast = 40.0% 10/10/11 10/10/11 10/10/11 10/10/11 10/10/11 4.3

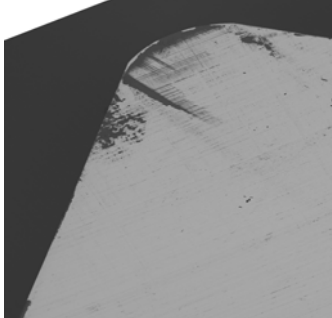
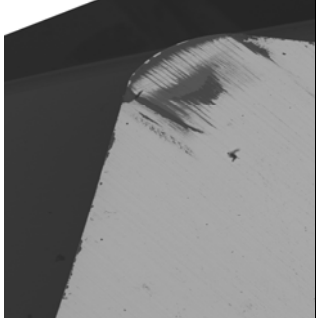
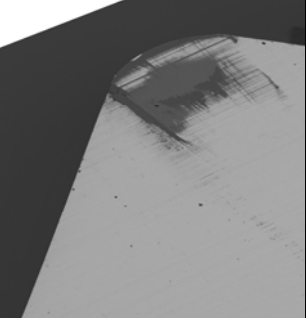
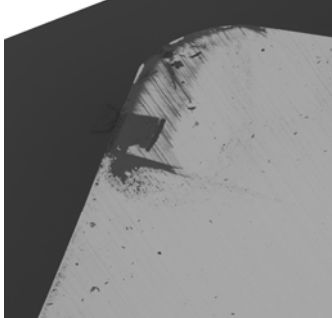
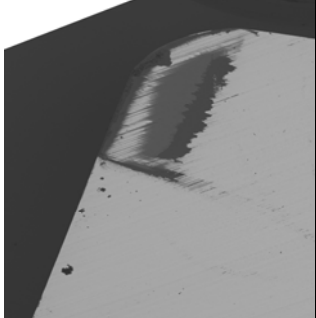
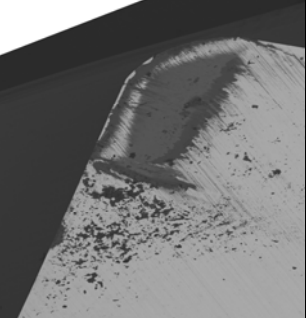
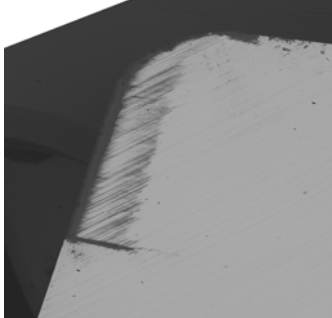
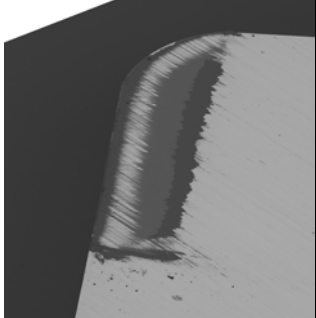
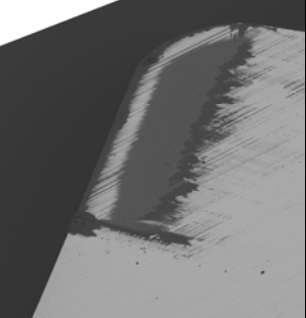
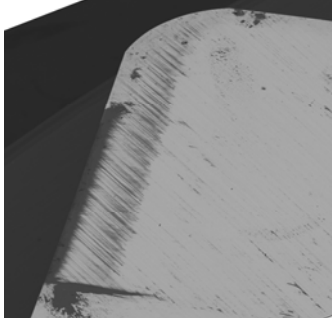
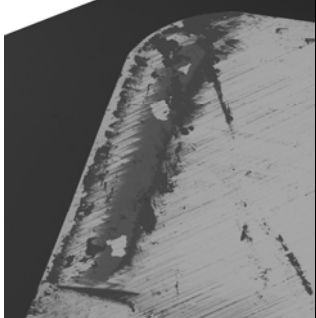
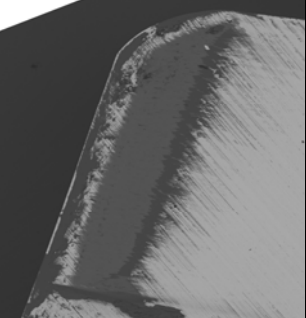
SEM Images for Al-6061 at 230 m/min

d mm	f = 0.071 mm/rev	f = 0.198 mm/rev	f = 0.305 mm/rev
0.51			
1.27			
2.03			
2.79			

SEM Images for Al-6061 at 345 m/min

d mm	f = 0.071 mm/rev	f = 0.198 mm/rev	f = 0.325 mm/rev
0.51			
1.27			
2.03			
2.79			

SEM Images for Al-6061 at 490 m/min

d mm	f = 0.071 mm/rev	f = 0.198 mm/rev	f = 0.325 mm/rev
0.51			
1.27			
2.03			
2.79			

APPENDIX C

CUTTING FORCE MEASUREMENTS

110 m/min (400 rpm)								
d / f	F_x (lbf)	F_y (lbf)	F_z (lbf)	F_r (lbf)	F_t (lbf)	F_a (lbf)	F_n (lbf)	F_f (lbf)
1.667	14.80	23.22	41.08	11.83	37.76	29.66	37.76	31.93
2.564	12.32	17.14	29.92	10.04	27.32	22.22	27.32	24.38
4.167	43.02	35.13	97.55	40.84	90.06	53.12	90.06	67.00
6.410	35.76	26.00	69.38	33.76	63.45	40.05	63.45	52.38
6.667	67.56	47.62	150.40	65.84	139.13	75.90	139.13	100.48
7.143	8.19	10.56	14.53	6.43	12.90	13.50	12.90	14.95
9.167	95.67	60.88	206.14	94.33	190.63	100.56	190.63	137.88
10.256	58.67	35.90	107.82	56.60	98.55	58.68	98.55	81.52
14.103	83.50	48.95	145.57	80.42	132.56	80.75	132.56	113.97
17.857	22.51	16.70	33.21	20.25	29.53	24.63	29.53	31.88
28.571	36.87	23.29	51.12	33.93	45.37	36.13	45.37	49.56
39.286	50.61	28.66	69.37	47.36	61.69	46.33	61.69	66.26

Cutting forces for Al-2024 at 110 m/min (rough data, transformed data)

225 m/min (558 rpm)								
d / f	F_x (lbf)	F_y (lbf)	F_z (lbf)	F_r (lbf)	F_t (lbf)	F_a (lbf)	F_n (lbf)	F_f (lbf)
1.667	10.86	16.47	38.22	9.53	35.76	21.92	35.76	23.90
2.564	9.48	12.22	28.00	8.41	26.03	16.59	26.03	18.60
4.167	24.49	24.11	79.96	24.32	75.26	36.32	75.26	43.71
6.410	22.08	18.37	59.26	21.68	55.32	28.39	55.32	35.72
6.667	42.84	35.40	135.13	43.87	127.36	56.60	127.36	71.61
7.143	5.81	7.51	12.61	4.76	11.44	9.80	11.44	10.89
9.167	57.87	38.90	178.35	61.20	168.44	67.48	168.44	91.10
10.256	39.35	27.22	99.65	39.53	93.03	44.76	93.03	59.72
14.103	52.73	33.86	131.19	53.44	122.49	57.25	122.49	78.32
17.857	15.70	11.42	27.86	14.59	25.27	17.37	25.27	22.68
28.571	28.77	16.44	46.88	27.53	42.44	27.13	42.44	38.65
39.286	38.21	21.00	62.04	36.76	56.21	35.20	56.21	50.89

Cutting forces for Al-2024 at 225 m/min (rough data, transformed data)

335 m/min (765 rpm)								
d / f	F_x (lbf)	F_y (lbf)	F_z (lbf)	F_r (lbf)	F_t (lbf)	F_a (lbf)	F_n (lbf)	F_f (lbf)
1.667	7.42	13.58	31.82	6.42	29.95	17.71	29.95	18.84
2.564	7.96	11.95	27.40	6.97	25.61	15.90	25.61	17.35
4.167	20.36	21.64	83.28	21.27	79.15	33.20	79.15	39.43
6.410	18.38	15.70	59.58	18.83	56.20	24.91	56.20	31.23
6.667	34.17	31.08	134.17	36.55	127.60	50.18	127.60	62.08
7.143	6.07	6.04	12.73	5.39	11.62	8.45	11.62	10.02
9.167	43.48	37.09	166.94	46.82	158.76	61.15	158.76	77.02
10.256	30.69	23.66	98.17	31.99	92.69	39.03	92.69	50.46
14.103	41.40	29.22	125.03	43.20	117.87	49.40	117.87	65.63
17.857	12.47	9.99	26.55	11.74	24.41	15.06	24.41	19.09
28.571	21.99	14.47	43.98	21.26	40.42	23.28	40.42	31.53
39.286	29.52	16.79	56.62	29.01	52.01	28.50	52.01	40.67

Cutting forces for Al-2024 at 335 m/min (rough data, transformed data)

470 m/min (1350 rpm)								
d / f	F_x (lbf)	F_y (lbf)	F_z (lbf)	F_r (lbf)	F_t (lbf)	F_a (lbf)	F_n (lbf)	F_f (lbf)
1.667	6.45	11.70	32.25	6.00	30.59	15.70	30.59	16.80
2.564	6.65	7.95	24.96	6.52	23.58	11.50	23.58	13.22
4.167	18.00	19.37	75.26	18.88	71.57	29.72	71.57	35.21
6.410	17.73	15.22	62.62	18.59	59.31	24.55	59.31	30.80
6.667	28.98	27.34	116.57	31.00	110.91	43.75	110.91	53.61
7.143	4.67	5.76	11.07	3.98	10.13	7.69	10.13	8.65
9.167	39.61	34.76	155.85	42.74	148.31	56.97	148.31	71.22
10.256	26.50	20.79	91.14	28.08	86.34	34.59	86.34	44.56
14.103	37.76	27.28	119.97	39.76	113.36	46.18	113.36	60.94
17.857	12.78	9.56	27.84	12.26	25.68	14.84	25.68	19.25
28.571	19.33	12.58	40.89	18.92	37.75	20.52	37.75	27.91
39.286	27.28	16.14	53.66	26.76	49.36	27.06	49.36	38.06

Cutting forces for Al-2024 at 470 m/min (rough data, transformed data)

120 m/min (400 rpm)								
d / f	F_x (lbf)	F_y (lbf)	F_z (lbf)	F_r (lbf)	F_t (lbf)	F_a (lbf)	F_n (lbf)	F_f (lbf)
1.667	20.82	33.03	45.02	22.49	24.44	49.48	49.48	33.21
2.564	16.29	22.76	31.55	14.95	18.67	34.73	34.73	23.92
4.167	60.46	43.97	100.61	17.96	60.57	108.25	108.25	63.18
6.410	47.52	33.20	72.16	13.40	47.87	78.08	78.08	49.71
6.667	89.80	57.25	145.92	19.21	88.26	156.44	156.44	90.33
7.143	8.28	10.06	13.85	6.34	9.30	15.32	15.32	11.26
9.167	130.16	73.66	204.29	19.51	126.22	218.61	218.61	127.72
10.256	73.63	42.68	106.66	12.79	72.42	114.94	114.94	73.54
14.103	106.28	58.83	152.85	15.88	103.94	164.51	164.51	105.15
17.857	23.62	15.90	32.67	6.36	23.92	35.57	35.57	24.75
28.571	36.68	21.63	49.16	7.07	36.52	53.35	53.35	37.20
39.286	53.52	28.25	69.57	7.33	52.64	75.35	75.35	53.15

Cutting forces for Al-6061 at 120 m/min (rough data, transformed data)

230 m/min (558 rpm)								
d / f	F_x (lbf)	F_y (lbf)	F_z (lbf)	F_r (lbf)	F_t (lbf)	F_a (lbf)	F_n (lbf)	F_f (lbf)
1.667	17.37	26.71	40.34	17.71	19.93	43.95	43.95	26.67
2.564	14.39	19.82	29.09	12.82	16.32	31.87	31.87	20.75
4.167	43.18	32.57	87.11	12.61	42.23	92.58	92.58	44.07
6.410	37.41	26.48	63.03	10.34	37.23	67.68	67.68	38.64
6.667	64.59	43.51	128.16	14.05	62.05	135.80	135.80	63.62
7.143	8.12	9.13	13.49	5.52	8.94	14.86	14.86	10.51
9.167	91.66	54.83	177.98	13.62	86.66	188.12	188.12	87.72
10.256	57.55	35.55	94.39	11.14	56.20	101.00	101.00	57.30
14.103	79.93	45.22	130.43	11.54	77.08	139.18	139.18	77.93
17.857	21.28	14.80	29.59	6.18	21.66	32.26	32.26	22.52
28.571	35.83	20.16	45.95	6.16	35.61	49.95	49.95	36.14
39.286	47.69	24.29	60.96	5.77	46.78	66.02	66.02	47.13

Cutting forces for Al-6061 at 230 m/min (rough data, transformed data)

345 m/min (765 rpm)								
d / f	F_x (lbf)	F_y (lbf)	F_z (lbf)	F_r (lbf)	F_t (lbf)	F_a (lbf)	F_n (lbf)	F_f (lbf)
1.667	14.01	20.43	36.86	12.83	15.43	39.61	39.61	20.07
2.564	12.51	16.22	26.65	10.06	13.82	28.95	28.95	17.09
4.167	32.09	25.51	76.96	9.56	30.65	81.07	81.07	32.11
6.410	29.92	21.48	56.33	8.04	29.34	60.04	60.04	30.42
6.667	50.71	35.53	118.64	10.78	47.50	124.65	124.65	48.70
7.143	8.08	8.95	12.98	5.40	8.91	14.34	14.34	10.42
9.167	69.35	43.76	161.70	10.14	63.79	169.41	169.41	64.59
10.256	46.29	29.33	86.31	8.76	44.49	91.64	91.64	45.34
14.103	62.25	36.80	115.86	9.26	59.19	122.74	122.74	59.91
17.857	19.92	12.28	26.99	4.33	19.94	29.32	29.32	20.41
28.571	31.58	18.02	41.91	5.54	31.32	45.46	45.46	31.81
39.286	44.61	23.11	57.94	5.69	43.77	62.71	62.71	44.14

Cutting forces for Al-6061 at 345 m/min (rough data, transformed data)

490 m/min (1350 rpm)								
d / f	F_x (lbf)	F_y (lbf)	F_z (lbf)	F_r (lbf)	F_t (lbf)	F_a (lbf)	F_n (lbf)	F_f (lbf)
1.667	10.52	17.40	34.06	11.06	11.55	36.30	36.30	15.99
2.564	9.13	13.23	23.86	8.30	10.04	25.65	25.65	13.03
4.167	26.05	22.17	72.77	8.28	24.35	76.18	76.18	25.72
6.410	23.07	17.60	53.63	6.32	22.00	56.52	56.52	22.89
6.667	42.01	30.98	112.99	9.14	38.46	118.03	118.03	39.53
7.143	6.50	8.05	11.57	5.06	7.27	12.74	12.74	8.86
9.167	62.67	41.44	159.25	9.84	56.98	166.32	166.32	57.82
10.256	37.16	24.34	83.23	6.59	34.70	87.48	87.48	35.32
14.103	52.17	31.31	111.53	6.96	48.46	117.23	117.23	48.96
17.857	17.57	11.68	25.99	4.44	17.61	28.12	28.12	18.16
28.571	28.27	16.08	40.44	4.66	27.77	43.59	43.59	28.16
39.286	38.62	20.10	53.86	4.69	37.60	57.98	57.98	37.89

Cutting forces for Al-6061 at 490 m/min (rough data, transformed data)